INVESTIGATIONS OF 3D BINARY BLACK HOLE SYSTEMS

Diplomarbeit

von

Lars Nerger

vorgelegt dem Fachbereich Physik der
Universität Bremen

angefertigt am

Albert-Einstein-Institut
Max-Planck-Institut für Gravitationsphysik
Golm

Contents

Acknowledgements

I would like to thank my advisors Prof. Edward Seidel and Dr. Bernd Brügmann for their guidance and support during the time I worked on this thesis. It was a great chance to work together with excellent researchers in an international research group under very good working conditions, which Ed Seidel offered to me. I am also grateful to Bernd Brügmann for many patient conversations about different aspects of numerical relativity.

I would like to thank Prof. Peter Richter, my advisor at the University of Bremen. Despite the fact that he is not working in the field of general relativity he made it possible for me to perform my diploma thesis external at the Max-Planck-Institute for Gravitational Physics (Albert-Einstein-Institute). We had several interesting discussions, mainly about black holes, focussing on their physical and numerical aspects.

All members of the numerical relativity group at the Albert-Einstein-Institute, especially Miguel Alcubierre, Ryoji Takahashi, and John Baker deserve thanks for their support and many conversations about various aspects of numerical relativity.

Thanks also to the *Cactus* team, Gabrielle Allen, Tom Goodale, and Gerd Lanfermann for their technical help.

I am especially grateful to my parents for the support I received from them.

Thanks to Anja for her understanding and encouragement.

Chapter 1

Introduction

1.1 Numerical Relativity

Albert Einstein's formulation of the theory of general relativity in 1915 changed our viewpoint on gravity and its significance in the universe. General relativity considers spacetime as a curved four-dimensional manifold, its curvature being induced by matter and determining the motion of matter in the spacetime. The equations introduced by Einstein, which govern the curvature as a manifestation of gravity, are a set of ten non-linear, coupled, partial differential equations for the ten components of the metric tensor. Still, more than 80 years after their publication, only a limited number of analytical solutions to this equations for highly symmetric problems is known. The solution space of the Einstein equations is essentially unknown.

A problem of special interest is the two-body problem of general relativity. In vacuum this is the binary black hole problem. That is the scenario of two black holes orbiting each other, spiraling inwards and eventually merging. Such black hole coalescences are expected to be strong emitters of gravitational waves which are candidates for detection [34, 35] by the gravitational wave detectors [51] LIGO (Livingston, USA), VIRGO (Pisa, Italy), and GEO600 (Hannover,Germany), which will soon be operational.

In contrast to Newtonian physics, where the two-body problem can be solved analytically, the full binary black hole problem is, in general, still unsolved. There are different attempts to the calculation of the inspiral of two black holes: In the early phase of the inspiral post-Newtonian methods are applicable [16] and the final stage of the coalescence can be modeled by perturbation methods [36]. But these methods are not applicable to the late strong-interaction phase of the coalescence. This phase is only accessible by numerical relativity, which employs computers to construct numerical solutions to the full Einstein equations.

Numerical relativity dates back to the year of 1964 where the first attempts to the numerical solution of the Einstein equations have been reported [38]. At this time the computational resources concerning computing speed and memory had been so small that the problem of an axisymmetric black hole merger was more or less intractable. In addition, no suitable algorithms had been developed at this time. Since this time the young research field of numerical relativity has evolved to a more mature state as is detailed by Hobill and Smarr in [33].

Today, the achievements of numerical relativity are strongly connected to the development of supercomputer technology. The computer technology has even reached a state allowing for the consideration of full three-dimensional problems.

In the 1990's many of the old problems have been reconsidered, employing larger computers to obtain more accurate results. However, one of the major goals, the general simulation of the binary black hole system, is still unsolved.

While applying numerical relativity to problems connected to binary black hole mergers Anninos et al. [11, 12] recently studied the axisymmetric collision of two black holes. Disturbed black holes have been studied by Camarda [29]. Such systems are analogous to excited black holes generated by a black hole merger. These simulations allowed evolution times to about 100M, where M is the spacetime mass. Furthermore, a first study of the evolution of a full three-dimensional binary black hole data set was reported by Brügmann [26]. In this work two black holes, each with momentum and spin, have been evolved until about 10M. This evolution time was sufficient for the black holes to merge but to short for the calculation of emitted gravitational waves. However, Brügmann showed that waves are at least possible in such simulations.

In this thesis I will also consider the full three-dimensional problem of binary black hole systems. This is strongly connected to Brügmanns work. Since this work, the initial data solver ('puncture' initial data) used by Brügmann, has been ported to a collaborative computational framework for numerical relativity, called *Cactus*, which will be described below. Using *Cactus* I will perform an intensive study of puncture initial data showing it's capabilities to provide initial data for studies of binary black hole systems. In addition, evolutions of full three-dimensional binary black hole data sets are performed. These are the first long time evolutions of such data sets which allow for the extraction of gravitational waves.

Before presenting the initial data study in chapter 7 and evolutions of puncture initial data in chapter 8 I will review the reformulation of the Einstein equations for numerical treatment in chapter 2. Further, in chapters 3 and 4, I will discuss the generation of initial data and different evolution algorithms. Different methods to extract physical quantities from the numerically generated spacetime will be discussed in chapter 5.

1.2   The Computational Environment

Numerical Relativity is a challenging research field. Due to the complexity of the Einstein equations, there are many computational difficulties. The coupled, nonlinear equations are of mixed hyperbolic, elliptic, and even undefined types. Due to the tensorial character of the equations, typically between 50 and 100 variables, like the metric components, require to be stored at each point of the computational grid. The equations consist of thousands of terms and thousands of operations have to be performed per grid point per evolution step. As a special feature of general relativity regions of strong gravity can generate singularities. Since these cannot be treated numerically they need to be avoided. Thus, a dynamic control of the coordinate system is necessary.

This complexity requires to push the limits of massively parallel computation. It also requires a collaborative technology: Solving the Einstein equations involves gravitational physics, computational science, the development of suitable and effective numerical algorithms and applied mathematics as for the development of appropriate boundary conditions. If the Einstein equations with sources are considered, for example in the simulation of neu-

tron stars, even the fields of astrophysics, hydrodynamics, and magneto-hydrodynamics have to be taken into account.

These challenges are most effectively solved by collaborative work of researchers out of the different fields. At the Albert-Einstein-Institute [3] a new code for collaborative treatment of the Einstein equations in three dimensions has been developed, the *Cactus* code [27].

This code exhibits a modular structure in featuring a central kernel, the 'flesh' and application modules, the 'thorns'. The flesh provides the basic infrastructure and the interface to the thorns together with input-output routines. It is optimized for parallel computing using the "Message Passing Interface" (MPI) libraries. The thorns provide routines for the physical application like evolution algorithms and are connected to the flesh via a defined interface for variables and function calls. This structure allows for collaborative code development since the development of applications is done the thorns while the flesh is maintained by a small group of researchers. Nonetheless, also the source code of the flesh is publically available.

While older versions of *Cactus* had been specialized for the use in numerical relativity, the latest version, *Cactus 4.0*, is a general tool for the numerical treatment of partial differential equations on parallel computers, since the flesh has been rewritten and all parts belonging to numerical relativity have been moved into thorns. Now it is possible to apply *Cactus* to numerous numerical problems by writing the corresponding thorn which can be used with other existing thorns, like output-routines. Thus, parallel computation is possible without special knowledge in parallel computing.

A user does apply the code by obtaining the required flesh and thorns via the Internet. With this he obtains the source codes which can be compiled by specifying the thorns in a configuration file and applying a "make" procedure. The run parameters are set by an input file which is read at execution time. Since the user only obtains and compiles the routines necessary for the problem he wants to solve or simulate, the development of a "monster"-code is avoided.

The work presented in this thesis was done using the release 3.2 of *Cactus*.

Numerical calculations were performed at the Albert-Einstein-Institute (AEI), the Rechenzentrum Garching (RZG), and the National Center for Supercomputer Applications (NCSA), Champaign, IL.

1.3   Notations and Geometrized Units

Throughout this thesis the notations conform with those of Misner, Thorne and Wheeler [45]. That is, Greek indices range from 0 to 3 and label spacetime components while Latin indices ranging from 1 to 3 refer to spatial components. Indices are used equivalently to label tensor components as well as tensors itself.

The signature of the four-dimensional spacetime metric is Lorentzian with $(-+++)$. The signature of the of spatial metric is $(+++)$.

Naturally, the Einstein summing convention is used, unless otherwise noted. That is, quantities are summed with respect to identical lowered and raised indices.

Tensors and vectors are either written with indices or in bold face without indices.

Partial derivatives with respect to a coordinate x^μ are denoted in differential or by comma notation:

$$\frac{\partial f^\mu}{\partial x^\nu} = \partial_\nu f^\mu \equiv f^\mu{}_{,\nu}$$

Covariant differentiation with respect to a coordinate x^μ on a four-dimensional spacetime is written as ∇_μ or in semicolon notation as

$$\nabla_\nu f^\mu \equiv f^\mu{}_{;\nu}$$

while the covariant derivative induced on three-dimensional hypersurfaces is denoted by D or the semicolon notation

$$D_a f^b \equiv f^b{}_{;a}$$

where it should be obvious from the context if the semicolon refers to the covariant derivative on the spacetime or a hypersurface.

Lie differentiation with respect to a vector field $n^\alpha = \mathbf{n}$ is indicated by the symbol $\mathcal{L}_n$.

The units used in this theses are the 'geometrized' units. That is the gravitational constant G and the speed of light c are set to unity.

Chapter 2

3+1-Formalism

In general relativity spacetime is considered to be a curved four-dimensional Lorentzian manifold. The geometry, i.e. curvature, of spacetime is related to the distribution of matter and energy by the Einstein equations

$$G_{\mu\nu} = 8\pi T_{\mu\nu} \tag{2.1}$$

with the Einstein tensor $G_{\mu\nu} = R_{\mu\nu} - \frac{1}{2}g_{\mu\nu}R$ being the trace-reduced Ricci tensor for the four-dimensional manifold and the stress-energy tensor $T_{\mu\nu}$. This equation treats time and space variables on an equal base.

A convenient way to solve the Einstein equations numerically is to write them in the form of a Cauchy problem. Then, we have to find an appropriate initial data set of basic variables according to some initial value equations specifying constraints on the initial data. We can evolve this data set by evolution equations, i.e. equations specifying time derivatives for the basic variables.

2.1   Maxwell Equations as a Cauchy Problem

Before rewriting the Einstein Equations we will consider the structure of the Maxwell equations. In vacuum the Maxwell equations read

$$\nabla \cdot \boldsymbol{B} = 0 \tag{2.2}$$

$$\nabla \cdot \boldsymbol{E} = 0 \tag{2.3}$$

$$\frac{\partial \boldsymbol{B}}{\partial t} + \nabla \times \boldsymbol{E} = 0 \tag{2.4}$$

$$\frac{\partial \boldsymbol{E}}{\partial t} - \nabla \times \boldsymbol{B} = 0 \ . \tag{2.5}$$

These equations can be broken up into two classes: Equations 2.2 and 2.3 do not contain any time derivatives. These are the initial value or constraint equations for the electric and magnetic fields $\boldsymbol{E}$ and $\boldsymbol{B}$. The constraint equations specify the allowed fields at a particular time, i.e. one obtains Cauchy initial data. Equations 2.4 and 2.5 are evolution equations. Containing first order time derivatives of the electric and magnetic fields they propagate the fields in time. The constraint and evolution equations are independent though they are compatible. That is, the evolution equations propagate the fields without violating the constraint equations. This is of course not guaranteed in numerical integrations of the equations due to the finite precision of the computations.

Written in this form the Maxwell equations exhibit "3+1" form. The initial data is constrained by equations only including spatial coordinates ("3") while the propagation in time ("1") is governed by a separated set of equations. Once the initial data have been specified they may be evolved forward in time by the evolution equations.

There is a third class of equations which will also appear in the 3+1 formulation of the Einstein equations. Introducing the vector potential $\boldsymbol{A}$ there is an additional equation

$$\boldsymbol{B} = \boldsymbol{\nabla} \times \boldsymbol{A} \ . \tag{2.6}$$

Any transformation of the vector potential of the form

$$\boldsymbol{A} \rightarrow \boldsymbol{A} + \nabla \Lambda \tag{2.7}$$

with an arbitrary scalar function Λ, leaves the field variables $\boldsymbol{E}$ and $\boldsymbol{B}$ invariant. So equation 2.6 is a gauge equation. This adds an additional degree of freedom to the equations which can be used to cast the equations in a convenient form dependent on the problem to be calculated. By rewriting the Maxwell equations in terms of the vector potential $\boldsymbol{A}$ and the scalar potential ϕ and using special choice of the gauge, like the Coulomb gauge ($\boldsymbol{\nabla} \cdot \boldsymbol{A} = 0$), one can often simplify the equations.

2.2 Einstein Equations in 3+1 form

We now turn to the discussion of the 3+1 formulation of the Einstein equations. Before considering the mathematical derivation of the equations we will introduce the more illustrative approach to the foliation of the spacetime as described in the textbook by Misner, Thorne and Wheeler [45].
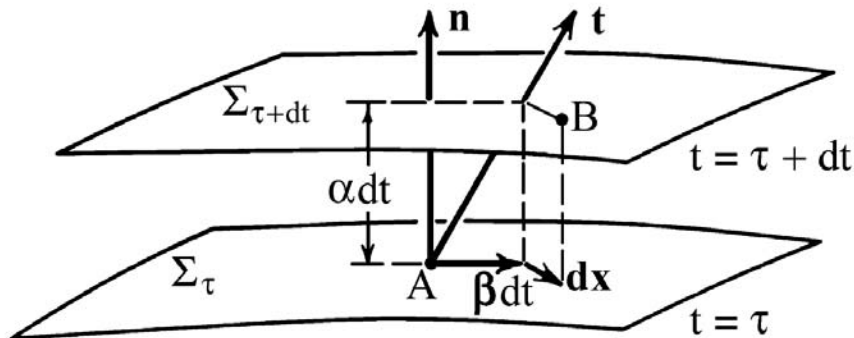

Figure 2.1: Two three-dimensional spacelike hyersurfaces Σ_τ and $\Sigma_{\tau+\delta t}$ connected by lapse function α and shift vector β.

We can foliate the four-dimensional spacetime $(\mathcal{M}, g)$ into a family of spacelike three-dimensional hypersurfaces $\{\Sigma\}$. These can be parameterized by a time parameter t.

For infinitesimally separated events the invariant distance between them, i.e. the metric of the spacetime, is

$$ds^2 = \gamma_{ab}(dx^a + \beta^a dt)(dx^b + \beta^b dt) - \alpha^2 dt^2 \qquad (2.8)$$

as is illustrated in figure 2.1. Here γ_{ab} is the (spatial) 3-metric on the hypersurface at time τ, Σ_τ. The distance from A to B is given by the purely spatial separation vector dx^a and the time vector dt. This can be split into the part normal to the hypersurface, αdt, which gives the propagation in time between the hypersurfaces and the tangential part given by a spatial shift $\beta^a dt$.

The 'lapse function' α describes the lapse of proper time between the two hypersurfaces Σ_τ and $\Sigma_{\tau+\delta t}$ at the times $t = \tau$ and $t = \tau + \delta t$ while the 'shift vector' β^a determines the coordinate distance a constant coordinate point moves away from the normal vector when advancing from Σ_τ to $\Sigma_{\tau+\delta t}$.

In numerical relativity the choice of the lapse function, and sometimes the foliation itself, is called 'slicing' with the spacelike hypersurfaces being called 'slices'.

The derivation of the standard 3+1 formulation of the Einstein equations was introduced by Arnowitt, Deser and Misner (ADM) [13]. York presented a detailed review of the Cauchy problem in [54]. A study of the initial value formulation of general relativity can also be found in the textbook by Wald [52]. We will follow the formal way in the notation of York [54] while reviewing the derivation of the equations.

In general the 3+1 formulation is derived by the introduction of a foliation of the four-dimensional spacetime by three-dimensional spacelike hypersurfaces. This slicing allows to define projection operators from the four-dimensional spacetime onto the three-dimensional slices. Using the foliation and the projection operators we are able to project the Einstein equations, equation 2.1, for the four-metric $g_{\mu\nu}$ onto the slices.

Mathematically the foliation is created by a normalized one-form ω_μ, which is the gradient of the time parameter t times the lapse function α:

$$\omega_\mu = \alpha \nabla_\mu t, \qquad \|\omega\| = -1 \qquad (2.9)$$

The foliation is spacelike if each of the slices is spacelike. Associated with the foliations due to ω_μ is the timelike unit normal vector field

$$n^\mu = -g^{\mu\nu}\omega_\nu, \qquad n^\beta n_\beta = -1 \qquad (2.10)$$

which yields the metric $\gamma_{\alpha\beta}$ induced on the slices as

$$\gamma_{\alpha\beta} = g_{\alpha\beta} + n_\alpha n_\beta \ . \qquad (2.11)$$

The mixed form γ^α_β is the projection operator into the slice

$$g^{\alpha\delta}\gamma_{\delta\beta} = \gamma^\alpha_\beta = \delta^\alpha_\beta + n^\alpha n_\beta \equiv \perp^\alpha_\beta \qquad (2.12)$$

while the projection normal to the slice is given by

$$N^\alpha_\beta = -n^\alpha n_\beta \ . \qquad (2.13)$$

($\perp$ without indices will denote the projection of all free indices.)
Using this we can project the covariant derivative ∇_α associated with the four-metric $g_{\alpha\beta}$

into a covariant derivate D_α associated with the three-metric $\gamma_{\alpha\beta}$ ($D_\alpha\gamma_{\beta\gamma} = 0$) on the slice by

$$D_\alpha = \perp \nabla_\alpha \tag{2.14}$$

Using this derivative operator we define the Riemann curvature tensor $R_{\mu\nu\sigma}{}^\gamma$ of a slice in analogy to the curvature tensor of the four-dimensional spacetime by the commutator of the covariant derivative acting on a one-form ω_μ:

$$D_{[\mu}D_{\nu]}\omega_\sigma = \frac{1}{2}\omega_\gamma R_{\mu\nu\sigma}{}^\gamma \tag{2.15}$$

From this the Ricci tensor $R_{\mu\nu}$ and the curvature scalar R follow from the standard definitions by successive contractions.

The foliation $\{\Sigma\}$ is embedded in the four-dimensional spacetime. To describe the embedding we use the extrinsic curvature tensor $K_{\alpha\beta}$. If the embedded slice is bent the normal vector n^α changes along each coordinate. This is expressed by the non-vanishing of the covariant four-derivative $\nabla_\alpha n_\beta$. The projection of this derivative is the change of the normal vector for an infinitesimal displacement within the surface and defines the extrinsic curvature tensor $K_{\alpha\beta}$:

$$K_{\alpha\beta} \equiv - \perp \nabla_{(\alpha}n_{\beta)} \tag{2.16}$$

The triple (Σ, γ, K) represents the complete geometry of an embedded slice and must be specified to obtain an initial data set. However, it cannot be chosen arbitrarily since the Einstein equations must be fulfilled. We find a first condition for the initial data by projecting all indices of the Riemann tensor $R^{(4)}_{\mu\nu\alpha\beta}$ onto the slice. This yields the 'Gauss equation'

$$\perp R^{(4)}_{\mu\nu\alpha\beta} = R_{\mu\nu\alpha\beta} + K_{\mu\alpha}K_{\nu\beta} - K_{\mu\beta}K_{\nu\alpha} \tag{2.17}$$

where the definition of the extrinsic curvature, equation 2.16, was used.

A second relation, the 'Codazzi equation', is found by the contraction of one index with the normal vector and subsequent projection of the remaining indices:

$$\perp R^{(4)}_{\mu\nu\alpha\sigma}n^\sigma = D_\nu K_{\mu\alpha} - D_\mu K_{\nu\alpha} \tag{2.18}$$

The 'Gauss-Codazzi' equations 2.17 and 2.18 represent integrability conditions for the embedding of the foliation (Σ, γ, K) in the four-dimensional spacetime $(\mathcal{M}, g)$. They are directly related to the initial value or constraint equations of the 3+1 formulation: Four of the ten Einstein equations 2.1 which contain no second derivatives of the metric in a timelike direction can be written in terms of the Gauss-Codazzi equations. Thus, these are the initial value or constraint equations. They read, with $trK = \gamma^{\alpha\beta}K_{\alpha\beta}$:

$$R + (trK)^2 - K^{\alpha\beta}K_{\alpha\beta} = 16\pi\rho \tag{2.19}$$

$$D_\beta(K^{\alpha\beta} - \gamma^{\alpha\beta}trK) = 8\pi j^\alpha \tag{2.20}$$

where ρ and j^α are matter terms given by projections of the stress-energy tensor $T_{\mu\nu}$. Equation 2.19 is called the 'Hamiltonian constraint' and equation 2.20 the 'momentum constraint'. Only initial data sets which fulfill these constraint equations are allowed by the Einstein equations.

To derive the evolution equations from the remaining Einstein equations we have to consider how the initial data $\gamma_{\alpha\beta}$ and $K_{\alpha\beta}$ propagates off the initial slice. Thus we need an equivalent to the Newtonian time derivative which here describes the change of a tensor field along a vector field. This mathematical procedure is provided by the 'Lie derivative'. It is a general form of derivatives which, in contrast to the covariant derivative, is independent of the metric. A treatment of Lie derivatives in mathematical form can be found in Wald [52].

The Lie derivative $\mathcal{L}$ can be written as a directional derivative of a tensor $\mathbf{T} = T_\nu$ along a vector field $\mathbf{u} = u^\mu$:

$$\mathcal{L}_u \mathbf{T} = \nabla_u \mathbf{T} - \nabla_T \mathbf{u} \tag{2.21}$$

With this the Lie derivative of the metric $\gamma_{\alpha\beta}$ along the timelike normal vector $\mathbf{n} = n^\alpha$ is

$$\mathcal{L}_n \gamma_{\alpha\beta} = -2K_{\alpha\beta} \tag{2.22}$$

and analogous the Lie derivative of the extrinsic curvature $K_{\alpha\beta}$ is:

$$K_{\alpha\beta} = -\frac{1}{2} \perp \mathcal{L}_n \gamma_{\alpha\beta}. \tag{2.23}$$

For the time vector t^μ in an evolution, i.e. the vector along which the system is evolved, we have a remaining degree of freedom as t^α is only required to be dual to the normalized one-form ω_ν ($t^\mu \omega_\mu = 1$). That is, the time vector is not necessarily normal to the slice. Thus we can decompose the timelike normal vector field $N^\alpha = \alpha n^\alpha$, which connects the slices of the foliation, into a spatial translation and one in time direction. So the vector t^α in time direction is given by a motion along the normal to the slice proportional to the lapse function α and a shift β^α in spatial direction as is illustrated in figure 2.1:

$$t^\alpha = \alpha n^\alpha + \beta^\alpha, \qquad \beta^\alpha \omega_\alpha = 0 \tag{2.24}$$

Equation 2.24 specifies the gauge freedom. The lapse function and the shift vector can be chosen quite arbitrarily (They just have to be spatially continuous and differentiable). Different choices result in different foliations without changing the underlying physics of the four-dimensional spacetime. Only well chosen gauge conditions allow a long time evolution of the Einstein equations in the sense that singularities existing in the spacetime are avoided by the slices.

Up to this point no spacetime basis has been introduced. We can choose the so called 'computational frames' (cf. [54]): We set $t^\alpha = (1, 0, 0, 0)$ and also require the spatial set n^i, ($i = 1, 2, 3$) of the four basis vectors to be purely spacelike. With this the four-metric $\gamma_{\alpha\beta}$ on the slice reduces to a three-metric γ_{ab} with $a, b = 1, 2, 3$ which we use to raise and lower indices. The four-metric $g_{\alpha\beta}$ of the four-dimensional spacetime is then given by

$$g_{\alpha\beta} = \begin{pmatrix} -\alpha^2 + \beta_l \beta^l & \beta_j \\ \beta_i & \gamma_{ij} \end{pmatrix} \tag{2.25}$$

which is equivalent to the line element given by equation 2.8.

In this basis the Lie derivative along the time-like vector t^α reduces to a partial time derivative:

$$\mathcal{L}_t = \partial_t = \alpha \mathcal{L}_n + \mathcal{L}_\beta \tag{2.26}$$

Thus the evolution equations for the metric γ_{ab} and the extrinsic curvature K_{ab} are

$$\partial_t \gamma_{ab} \;=\; -2\alpha K_{ab} + 2D_{(a}\beta_{b)} \tag{2.27}$$

$$\partial_t K_{ab} \;=\; -D_a D_b \alpha + \alpha[R_{ab} - 2K_{ac}K^c{}_b + K_{ab}trK]$$
$$+\beta^c D_c K_{ab} + K_{ac}D_b\beta^c + K_{cb}D_a\beta^c \;. \tag{2.28}$$

Also the constraint equations simplify to

$$R + (trK)^2 - K^{ab}K_{ab} \;=\; 16\pi\rho \tag{2.29}$$

$$D_b(K^{ab} - \gamma^{ab}trK) \;=\; 8\pi j^a \;. \tag{2.30}$$

We have obtained the evolution equations in the standard ADM form and the constraint equations. Appropriate solutions to equations 2.29 and 2.30 provide the initial data sets, which can be evolved by the use of the evolution equations 2.27 and 2.28.

Chapter 3

Initial Data

In the initial data problem of general relativity we are concerned with the solution of the Hamiltonian and the momentum constraint equations given by 2.29 and 2.30.

In this work we only consider solutions to the vacuum Einstein equations representing black hole spacetimes. Such initial data sets are obtained by the introduction of a non-trivial topology onto the hypersurfaces representing the initial data slice. Further, the trace of the extrinsic curvature trK is required to vanish. Since in vacuum the matter terms in the constraint equations vanish the equations simplify to

$$ham \equiv R - K^{ab}K_{ab} \;=\; 0 \tag{3.1}$$

$$mom^b \equiv D_a K^{ab} \;=\; 0. \tag{3.2}$$

We will discuss the procedure for finding initial data according to the review by York [54]. Then we will review several types initial data sets representing black hole systems.

3.1   The conformal decomposition method

York [54] describes a formalism for solving the constraint equations which is based on a conformal transformation of the metric γ_{ij} and the extrinsic curvature K_{ij}. This technique traces back to work of Lichnerowicz [43].

We set, with the 'conformal factor' ψ:

$$\gamma_{ij} = \psi^4 \hat{\gamma}_{ij}; \qquad K_{ij} = \psi^{-2}\hat{K}_{ij} \tag{3.3}$$

Since we have not imposed any restrictions on the form of the metric $\hat{\gamma}_{ij}$ we can choose it to be flat space. Then the three-metric γ_{ij} is conformally flat.
With this the momentum constraint becomes an equation for the extrinsic curvature

$$\hat{D}_a \hat{K}^{ab} = 0 \tag{3.4}$$

and the Hamiltonian constraint becomes an elliptic equation for the scalar field ψ

$$\hat{D}^a \hat{D}_a \psi + \frac{1}{8}\hat{K}^{ab}\hat{K}_{ab}\psi^{-7} = 0 \tag{3.5}$$

where the covariant derivate $\hat{D}_a$ is defined by the flat metric $\hat{\gamma}_{ab}$.

This procedure decouples the Hamiltonian and the momentum constraint equations in the sense that, for a given extrinsic curvature, it remains to solve the elliptic equation for the conformal factor ψ.

We can now solve the constraint equations in three steps:

- First we solve the conformal form of the momentum constraint, equation 3.4, to obtain the extrinsic curvature $\hat{K}_{ab}$. This can be done analytically or numerically.

- Then we solve the elliptic equation for the conformal factor ψ. This is usually done numerically.

- Finally we reconstruct the physical fields γ_{ab} and K_{ab} with the transformation equations 3.3.

3.2   Schwarzschild Initial Data

The Schwarzschild metric is a static spherically symmetric solution to the vacuum Einstein equations. It describes the spacetime of the exterior of a static star or a non-rotating uncharged black hole. In its standard form the metric is given for a mass M of the black hole by

$$ds^2 = -\left(1 - \frac{2M}{r}\right)dt^2 + \frac{1}{1 - \frac{2M}{r}}dr^2 + r^2 d\Omega^2 \tag{3.6}$$

For $r = 0$ this metric exhibits a physical singularity and for $r = 2M$ there is a coordinate singularity. For $r \to \infty$ the metric is asymptotical flat.

Due to the divergence of the g_{rr} term the standard form of the Schwarzschild metric is not amenable to numerical treatment. But for numerical calculations we can write the Schwarzschild metric in isotropic form by the introduction of the isotropic coordinate $\bar{r}$

$$r = \bar{r}\left(1 + \frac{M}{2\bar{r}}\right)^2 . \tag{3.7}$$

Thus the metric is

$$ds^2 = -\left(\frac{2\bar{r} - M}{2\bar{r} + M}\right)^2 dt^2 + \psi(\bar{r})^4 (d\bar{r}^2 + \bar{r}^2 d\Omega^2) \tag{3.8}$$

with the conformal factor

$$\psi(\bar{r}) = 1 + \frac{M}{2\bar{r}} . \tag{3.9}$$

Considered as initial data, the time symmetry of the Schwarzschild solution leads to

$$K_{ab} = 0 . \tag{3.10}$$

Now equation 3.9 is a local solution to the elliptic equation 3.5 for the conformal factor ψ. Hence, the initial data is given by equations 3.10 and 3.9 and the requirement that $\hat{\gamma}_{ij}$ is the metric of flat space.

In isotropic coordinates the Schwarzschild solution does not exhibit the singularity at $r = 2M$ any more. Now there exists an isometry at coordinate radius $\bar{r} = M/2$. That is, inversion through a sphere of this coordinate radius

$$\bar{r} \to \frac{M^2}{4\bar{r}} \tag{3.11}$$

leaves the coordinate sphere $\bar{r} = M/2$ invariant while mapping the entire exterior region into that sphere. Hence, there exists a second asymptotically flat region for $\bar{r} \to 0$. These two asymptotically flat regions are connected by the isometry sphere, which is called the 'throat' or 'Einstein-Rosen bridge'. In this case of a time-symmetric solution to the Einstein equations the throat coincides with the event horizon.

The two asymptotically flat regions together with the throat can be displayed in a Kruskal diagram showing the Schwarzschild spacetime in Kruskal-Szekeres coordinates [45]. The Kruskal-Szekeres coordinates u and v are related to the Schwarzschild coordinates r_s and t_s by:

$$u^2 - v^2 = \left(\frac{r_s}{2M} - 1 \right) e^{r_s/2M} \tag{3.12}$$

$$t_s = \begin{cases} 4M \ tanh^{-1}(v/u) & \text{in I and II} \\ 4M \ tanh^{-1}(u/v) & \text{in II and IV} \end{cases} \tag{3.13}$$

where I to IV denote quadrants of the diagram which is displayed in figure 3.1. As the classical Schwarzschild solution only covers the regions I and II, Kruskal-Szekeres coordinates extend the solution. Furthermore the coordinate singularity at $r = 2M$ vanishes.

In the Kruskal diagram the $t = 0$-line shows the following characteristics: The smallest coordinate distance to the singularity of the initial slice is $r = 2M$ for $u, v = 0$. On the right hand side the slice approaches spatial infinity, $r \to \infty$. Here is one of the two isometric asymptotical flat regions (I). On the left hand side for $r \to \infty$ the other isometric asymptotical flat region (III) is reached. Since the closest distance is $r = 2M$ the initial data slice does not penetrate the event horizon, located at $r = 2M$. Thus, the slice does not enter the interior regions II and IV of the black hole solution.

The character of the Schwarzschild black hole can be also depicted in an embedding diagram as displayed in figure 3.2. This is the classic wormhole picture [45, 23] showing the non-trivial topology of the hypersurface. In the embedding one recognizes both asymptotic flat regions as well as the throat connecting them. The manifold consists of two sheets, each of geometry $\mathbb{R}^3 - S^2$, with the surfaces of the S^2 identified. This excised sphere with coordinate radius $r = 2M$ is the throat of the black hole. Due to the isometry of the two sheets we can treat the initial data on $\mathbb{R}^3 - S^2$ with an inner boundary given by the surface of the excised sphere.

A second possibility in which the Schwarzschild solution in isotropic coordinates, equations 3.8 and 3.9, can be viewed arises from the fact that these equations are also valid when considered as a problem on $\mathbb{R}^3$ with just the point $r = 0$ excised. In this case no isometry exists.
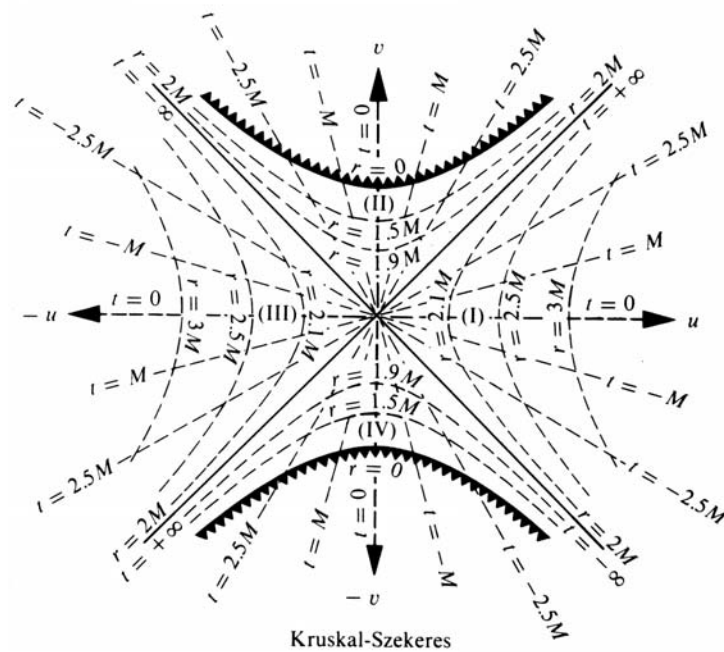
Figure 3.1: Representation of the Schwarzschild black hole in Kruskal-Szekeres coordinates (from [45]). The Schwarzschild geometry consists of four regions I, II, III, IV where I and III are two distinct asymptotically flat regions. The black hole interior is given by the regions II and IV. The classical Schwarschild solution, equation 3.6, covers regions I and II.
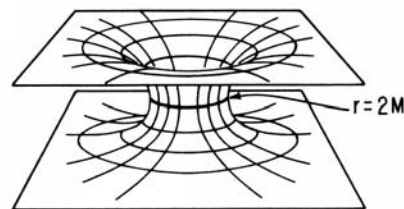

Figure 3.2: The geometry of the slice t = 0 for Schwarzschild initial data as embedded in flat space (from [52]) with one dimension suppressed so that each circle displayed represents a 2-sphere S^2.

Despite the fact that the Schwarzschild spacetime is static, it is of some numerical interest (cf. work by Camarda [28], Anninos et al. [9], and Brügmann [24]). With appropriate slicings we can generate a dynamical evolution. Thus, we can evolve an analytically known system to check the implemented numerics. This is also important since the end state in the evolution of any black hole system without net linear and angular momentum will be a Schwarzschild black hole.

3.3   Brill-Lindquist and Misner Initial Data

For time symmetric and conformally flat initial data the Hamiltonian constraint 3.5 reduces to

$$\Delta \psi = 0 \tag{3.14}$$

where Δ is the standard flat space Laplace operator: $\Delta = \nabla_a \nabla^a$. We are seeking for asymptotic flat solutions ($\psi \to 1$ for $r \to \infty$) to this equation.

Such solutions are known, e.g. from the theory of electromagnetism, to be unity and $1/r$-terms [40]. Hence the general solution is

$$\psi = 1 + \sum_i \frac{D_i}{|\mathbf{r} - \mathbf{r}_i|} \tag{3.15}$$

with parameters D_i. The conformal factor of Schwarzschild initial data equation 3.9 obviously has this form.

To generalize Schwarzschild initial data to initial data describing a time symmetric slice with N black holes located at $\{\mathbf{r}_r\}$ we can simply write

$$\psi_{BL} = 1 + \sum_{i=1}^{N} \frac{M_i}{2|\mathbf{r} - \mathbf{r}_i|} \tag{3.16}$$

where M_i is the mass of black hole i for the case of infinite separation of the holes. The total mass of the spacetime (ADM mass m_{ADM} as will be discussed below) is in this case just the sum over the masses M_i of all holes. This form of initial data is called the 'Brill-Lindquist' solution [23].

The Brill-Lindquist solution can be viewed as a solution on $\mathbb{R}^3$ with several 2-spheres of radius $r_i = 2M_i$ excised. The surface of each 2-sphere can again be identified with the inner boundary of another $\mathbb{R}^3$ with one sphere excised. Each black hole located in the upper asymptotically flat sheet of the manifold has its own lower asymptotically flat sheet as is displayed in figure 3.3(a). Thus the initial data is a $N + 1$-sheeted manifold. Alternatively this solution can be considered on $\mathbb{R}^3$ with several punctures located at the $\{\mathbf{r}_i\}$. In any case, this initial data does not possess an inversion symmetry through 2-spheres.

To obtain initial data which does show inversion symmetry we have to consider an infinite sum of mirror 'charges' with different amplitudes, analogous to the theory of electrodynamics [40]. This calculation yields an initial data set which is specified by a single parameter μ as was reported by Misner [44]. In Cartesian coordinates the conformal factor for two black holes is given by

$$\psi_M = 1 + \sum_{n=1}^{\infty} \frac{1}{\sinh(n\mu)} \left(\frac{1}{+r_n} + \frac{1}{-r_n} \right) \tag{3.17}$$
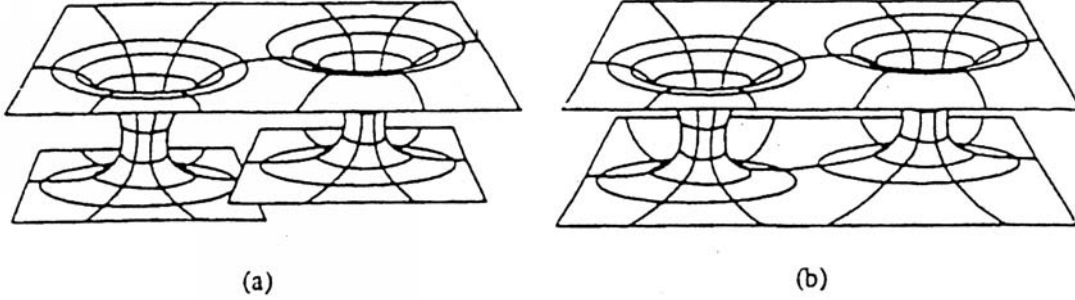
Figure 3.3: Embedding diagrams showing the geometry for two-black hole initial data slices (from [30]). (a) three-sheeted manifold representing Brill-Lindquist two black hole initial data. (b) two-sheeted manifold representing Misner initial data.

with

$$^{\pm}r_n = \sqrt{x^2 + y^2 + (z \pm \coth(n\mu))^2} \; . \tag{3.18}$$

This solution to the Hamiltonian constraint represents a system of two equal mass black holes, which are non-rotating and at rest on the initial slice. The holes are aligned along z-axis, centered at $z = \pm \coth(\mu)$ and with throats of radius $a = 1/\sinh(\mu)$. The parameter μ specifies the total spacetime mass m_{ADM} and the proper distance along the spacelike geodesic connecting the two throats. While increasing μ the centers of the holes approach each other in coordinate space and the throat radii decrease, leading to a decrease in the total mass of the system and a growing proper distance of the two holes. The topology of this solution is a multiply-connected, two-sheeted manifold, each sheet being asymptotically flat. This is displayed in figure 3.3(b) for a system of two black holes.

Misner initial data is of particular interest for numerical relativity as it represents either a system of two black holes or a single black hole dependent on the parameter μ (For $\mu > 1.8$ there are initially separated event horizons [8]). Furthermore the system is axisymmetric. This allows for the treatment with a two-dimensional (2D) computational code which saves computation time and memory. Finally, due to the isometry, this data set allows a rather stable evolution. Since the interior of the throat is often covered only by a very limited number of grid points in discrete numerical grids, this region is only poorly resolved. Considering the isometry and mapping the exterior region into the interior of the throat during an evolution gives more precise data for the interior.

Misner initial data has first been studied in numerical evolutions in 1964 by Hahn and Lindquist [38]. In the recent years this system was again studied intensively by Anninos et al. [7, 10, 11].

There have also been studied a number of other initial data sets which are generalizations of Schwarzschild, Brill-Lindquist or Misner inital data. For the case of a single black hole this have been rotating black holes as well as distorted black holes caused by an superposed gravitational wave (e.g. [21]). Also Misner initial data has been studied for cases with different masses by Brand and Anninos [12]. Usually also the generalized data sets are chosen such that they are still axisymmetric or do show symmetries that allow to compute only an octant of the Cartesian grid to reduce the memory requirements.

3.4 Full 3D Black Hole Initial Data

The data sets presented so far can be further generalized to non-time symmetric initial data. By the introduction of linear momentum and spin on the black holes we can create initial data sets which are full three-dimensional. I.e. they are not showing any symmetries. Hence, these data sets can no longer be treated with 2D computational codes.

The creation of such initial data is based on work of Bowen and York [19]. Cook et al. [30, 31, 32] constructed and studied a generalization of Misner initial data, which is a multiple black hole system with spin and momentum on the holes. Like the Misner data this data is isometric through the throats. The extrinsic curvature is first given analytically and then deformed to be consistent with the isometries. In this case the solution of the Hamiltonian constraint for the conformal factor ψ, which has to be done numerically, is difficult. This arises from the fact that the constraint is an elliptic equation on $\mathbb{R}^3 - \{several\ 2-spheres\}$ with an inner boundary on the excised 2-spheres given by the isometry.

In this work I will focus on another type of full 3D black hole initial data, which was introduced by Brandt and Brügmann [20]. It is based on the idea of a compactification of the internal asymptotically flat regions (lower sheets of the manifold) leading to a simple domain of integration. Analogous to Brill-Lindquist initial data a solution for the initial data on $\mathbb{R}^3 - \{\mathbf{r}_{(i)}\}$ with $\{\mathbf{r}_{(i)}\}$ being the coordinate locations of the black holes. Therefore this type of initial data is also referred to as 'puncture' initial data.

In the case of vacuum, a conformally flat metric γ_{ab}, and a trace free extrinsic curvature, $K_{ab} = 0$, but no time symmetry the conformal Hamiltonian constraint is given by equation 3.5

$$\Delta\psi + \frac{1}{8}\hat{K}^{ab}\hat{K}_{ab}\psi^{-7} = 0 \tag{3.19}$$

with Δ being the flat space Laplace operator. The momentum constraint in this case is, according to equation 3.4

$$\partial_a K^{ab} = 0 \ . \tag{3.20}$$

Following Bowen and York [19], a solution to the momentum constraint for the extrinsic curvature of a slice representing a single black hole at the origin with intrinsic momentum P^a and spin S^a is

$$
\begin{aligned}
\hat{K}^{ab}_{PS} &= \frac{3}{2r^2}[P^a n^b + P^b n^a - (\hat{\gamma}^{ab} - n^a n^b)P^c n_c] \\
&\quad + \frac{3}{r^3}(\epsilon^{acd}S_c n_d n^b + \epsilon^{bcd}S_c n_d n^a) \ .
\end{aligned}
\tag{3.21}
$$

Here n^a is the radial vector $n^a = x^a/r$ ($r = (x^2 + y^2 + z^2)^{1/2}$ in Cartesian coordinates) and ϵ^{abc} is the completely antisymmetric (Levi-Cevita) tensor. The constants are chosen in such a way, that the spacetime mass, the linear, and the angular momentum computed by the integrals which will be introduced in section 5.1, are consistent with the parameters P^a, S^a and the intrinsic mass M appearing in the conformal factor. This extrinsic curvature is smooth and regular on the punctured manifold $\mathbb{R}^3 - \{\mathbf{0}\}$.

Using the extrinsic curvature introduced by Bowen and York, Brandt and Brügmann create an analytic extrinsic curvature for N black holes by setting

$$\hat{K}_{BrBr}^{ab} = \sum_{i=1}^{N} \hat{K}_{PS(i)}^{ab} \ . \tag{3.22}$$

Each term of the sum is defined by equation 3.21 with its own origin $\mathbf{r}_{(i)}$, momentum $\mathbf{P}_{(i)}$, and spin $\mathbf{S}_{(i)}$. Due to the linearity of the momentum constraint this extrinsic curvature is clearly a solution of it.

Since the momentum constraint is solved analytically it remains to solve the Hamiltonian constraint. For this the conformal factor is written as

$$\psi = \frac{1}{\chi} + u \tag{3.23}$$

with

$$\frac{1}{\chi} = \sum_{i=1}^{N} \frac{M_{(i)}}{2|\mathbf{r} - \mathbf{r}_{(i)}|} \tag{3.24}$$

where $M_{(i)}$ is the mass of the i-th black hole. The Laplacian of χ^{-1} is zero on the punctured $\mathbb{R}^3 - \{\mathbf{r}_{(i)}\}$. Hence, the Hamiltonian constraint, equation 3.19, becomes an elliptic equation for u:

$$\Delta u + \frac{1}{8}\chi^7 \hat{K}^{ab}\hat{K}_{ab}(1 + \chi u)^{-7} = 0 \tag{3.25}$$

In general this equation has to be solved numerically. Brandt and Brügmann showed in [20] that the conformal factor u is regular on $\mathbb{R}^3$ since puncture initial data is asymptotically flat at the punctures. Thus, equation 3.25 can be solved on $\mathbb{R}^3$ without excision of points and without inner boundaries which simplifies the numerical implementation.

Mathematically, each puncture represents the "point at infinity" for one of the lower sheets of the $N + 1$-sheeted manifold. Thus solving equation 3.25 on $\mathbb{R}^3$ involves a compactification of N out of $N + 1$ asymptotically flat sheets.

The necessity of a numerical solution of equation 3.25 points to the question of boundary treatment. The elliptic solver implemented into *Cactus* is a multigrid algorithm based on Brügmann's BAM [20, 25]. There are two boundary conditions implemented.

For asymptotic flatness it is required

$$u \to 1 \text{ for } r \to \infty \tag{3.26}$$

Thus, the simplest boundary condition is a static one, requiring

$$u|_{r_{bound}} = 1 \tag{3.27}$$

at the boundary r_{bound}. Generally this works fine as long as the boundary is so far out that the slice is almost flat at the boundary.

A more advanced boundary condition is given by the Robin condition. This arises from a multi-pole expansion for the conformal factor, $\psi = 1 + a/r + \ldots$, (cf. [54, 56]) and is the condition

$$\partial_r u \Big|_{r_{bound}} = \frac{1 - u(r_{bound})}{r_{bound}} \ . \tag{3.28}$$

In the Cartesian numerical grid used in *Cactus* this is implemented as

$$\partial_x u\Big|_{x_{bound}} = \frac{1-u}{r_{bound}^2} x_{bound} \qquad (3.29)$$

where x_{bound} is one of the Cartesian components of the location $\mathbf{r}_{bound}$ of the boundary. This boundary condition gives the correct asymptotic form of u to order $O(r^{-1})$ as it assumes $u = 1 + O(r^{-1})$.

In figure 3.4 the regular part u of the conformal factor for a single black hole of mass $m = 1$ and with a momentum $\mathbf{P} = (1, 0, 0)$ is displayed. As is visible, u is regular also in the vicinity of the puncture where it exhibits a small bump. Furthermore, despite the fact that the function was computed using Robin boundary conditions, the influence of the boundary is visible. This is caused by the influence of $1/r^2$ terms which are not considered in the boundary treatment as this assumes a $1/r$ fall-off. However, the influence of the boundary on the values in the interior of the computational grid diminishes with an increasing location of the outer boundary.

The corresponding rescaled metric component γ_{xx}/ϕ^4 is shown in figure 3.5. For N black holes the factor ϕ is given by

$$\phi = 1 + \sum_{i=1}^{N} \frac{M_i}{2r_i} \ . \qquad (3.30)$$

and results in a rescaling such that the metric components are not diverging.

I will carry out an extensive study of puncture initial data and evolutions of such data sets below in the chapters 6 and 7.
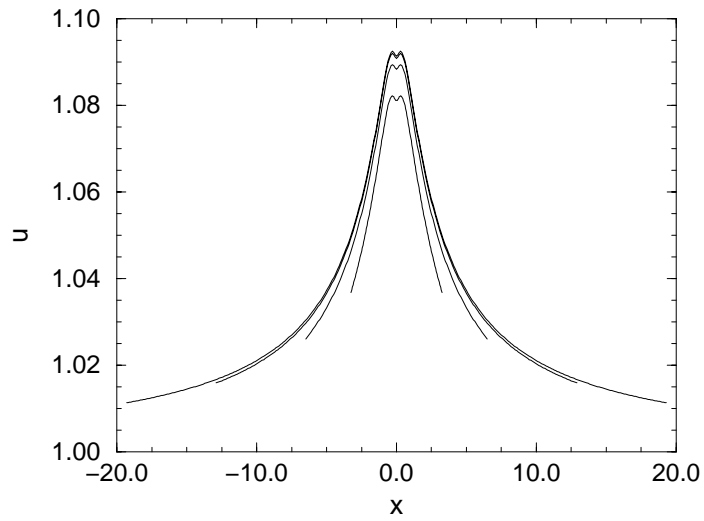
Figure 3.4: Regular part of the conformal factor u for a single black hole with $m = 1$ and with $\mathbf{P} = (1, 0, 0)$ for different boundary locations computed with Robin conditions.
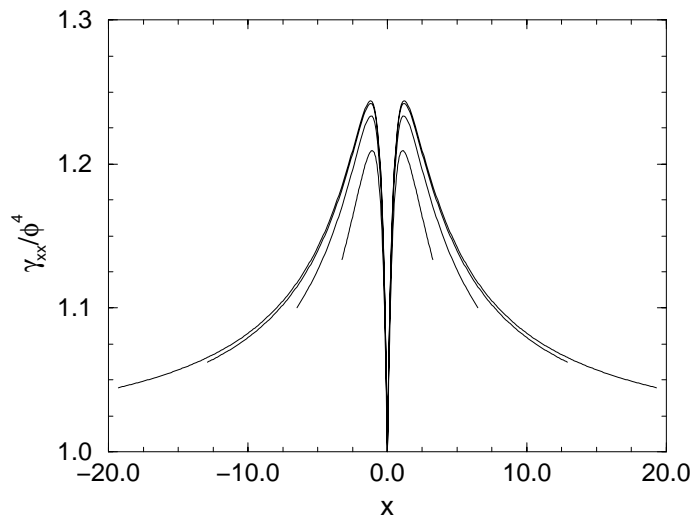

Figure 3.5: Metric component g_{xx} for a single black hole with $m = 1$ and with $\mathbf{P} = (1, 0, 0)$ for different boundary locations computed with Robin conditions.

Chapter 4

Evolution Algorithms & Gauge Conditions

In order to evolve the the initial data, which has been specified using the formalism discussed above, we have to apply the evolution equations resulting from the 3+1 decomposition of the Einstein equation. In the standard ADM form these equations are given by 2.27 and 2.28:

$$\partial_t \gamma_{ab} = -2\alpha K_{ab} + 2D_{(a}\beta_{b)} \tag{4.1}$$

$$\partial_t K_{ab} = -D_a D_b \alpha + \alpha[R_{ab} - 2K_{ac}K_b^c + K_{ab}trK]$$
$$+ \beta^c D_c K_{ab} + K_{ac}D_b\beta^c + K_{cb}D_a\beta^c \tag{4.2}$$

Despite the fact that the derivation of these equations is straightforward they are problematic for numerical implementation. This system of equations is not hyperbolic in any known sense, which can cause stability problems in the numerical code (cf. [14]).

Due to this there have been proposed several alternative, hyperbolic formulations of the evolution equations (e.g. [18]). But, according to Baumgarte and Shapiro [14], it is not yet clear to which degree the non-hyperbolicity of the ADM equations affects the stability of the numerical implementation. They propose a different, ADM-like formalism which is based on the evolution of conformal quantities which we will review in the next section.

Alcubierre et al. [4] have performed a numerical examination of the stability properties of different evolution systems. In particular, they compared evolutions with the ADM formalism with evolutions using the formalism by Baumgarte and Shapiro. This study showed that the instability of the ADM formulation is caused by constraint violating zero speed wave modes, which acquire a finite speed in the Baumgarte-Shapiro formalism.

Having chosen an evolution formalism it remains to specify the gauge conditions. Thus we have to specify the evolution of the shift vector β^a and lapse function α. The choice of α is referred to as 'slicing' since it determines the shape of the foliation. I will discuss gauge choices in section 4.2

4.1 The Conformal ADM Evolution System

Baumgarte and Shapiro [14] propose an evolution system in extending work of Shibata and Nakamura [49]. I will refer to this system as the *BSSN* formalism.

Instead of evolving just the metric γ_{ab} and the extrinsic curvature K_{ab}, we can evolve a conformal factor λ, the trace $K = \gamma^{ab}K_{ab}$ of the extrinsic curvature, and a conformally rescaled metric and extrinsic curvature. We construct the *BSSN* evolution system for vacuum as follows:

We write the conformal metric as

$$\tilde{\gamma}_{ij} = e^{-4\lambda}\gamma_{ij} \tag{4.3}$$

with the choice

$$e^{4\lambda} = \gamma^{1/3} \equiv \det(\gamma_{ij})^{1/3} \ . \tag{4.4}$$

For the trace-free part of the extrinsic curvature K_{ij}

$$A_{ij} = K_{ij} - \frac{1}{3}\gamma_{ij}K \tag{4.5}$$

we set analogous to the conformal decomposition of the metric

$$\tilde{A}_{ij} = e^{-4\lambda}A_{ij} \ . \tag{4.6}$$

Using the trace of the ADM evolution equations the relations

$$\frac{d}{dt}\lambda = -\frac{1}{6}\alpha K \tag{4.7}$$

and

$$\frac{d}{dt}K = -\gamma^{ij}D_iD_j\alpha + \alpha\left(\tilde{A}_{ij}\tilde{A}^{ij} + \frac{1}{3}K^2\right) \ . \tag{4.8}$$

are obtained. The trace-free parts of the ADM evolution equations yield

$$\frac{d}{dt}\tilde{\gamma}_{ij} = -2\alpha\tilde{A}_{ij} \tag{4.9}$$

and

$$\frac{d}{dt}\tilde{A}_{ij} = e^{-4\lambda}\left(-(D_iD_j\alpha)^{TF} + \alpha R_{ij}^{TF}\right) + \alpha(K\tilde{A}_{ij} - 2\tilde{A}_{il}\tilde{A}^l_{\ j}) \tag{4.10}$$

where the superscript TF denotes the trace-free part of a tensor.

Finally we bring the Ricci tensor $\tilde{R}_{ij}$ into a manifestly elliptic form by introducing 'conformal connection functions'

$$\tilde{\Gamma}^i \equiv \tilde{\gamma}^{jk}\tilde{\Gamma}^i_{jk} = -\tilde{\gamma}^{ij}_{\ ,j} \tag{4.11}$$

where the $\tilde{\Gamma}^i_{jk}$ are the connection coefficients associated with $\tilde{\gamma}_{ij}$. With this the evolution equations for the conformal metric 4.9 and the trace-free extrinsic curvature 4.10 reduce to a coupled set of nonlinear, inhomogeneous wave equations, with source terms given by the gauge terms K and $\tilde{\Gamma}_{ij}$ and the conformal factor λ.

In general the connection functions $\tilde{\Gamma}^i$ are pure gauge quantities. However, we impose the gauge by choosing the shift β^i and evolve the $\tilde{\Gamma}^i$ with the evolution equation 4.12 which can be derived by permuting a time derivative with the space derivative in 4.11. It is for vanishing shift

$$\frac{\partial}{\partial t}\tilde{\Gamma}^i = -2\tilde{A}^{ij}\alpha_{,j} + 2\alpha\left(\tilde{\Gamma}^i_{jk}\tilde{A}^{kj} - \frac{2}{3}\tilde{\gamma}^{ij}K_{,j} + 6\tilde{A}^{ij}\lambda_{,j}\right) \tag{4.12}$$

In the *BSSN* formalism the fundamental variables are λ, K, $\tilde{\gamma}_{ij}$, $\tilde{A}_{ij}$, and $\tilde{\Gamma}^i$ which will be evolved with the evolution equations 4.7, 4.8, 4.9, 4.10, and 4.12.

Throughout this work I will use the *BSSN* formalism for evolutions.

4.2 Gauge Choices

In the evolutions to be discussed in chapter 7 a vanishing shift vector

$$\beta^a = 0 \tag{4.13}$$

is used since this simplifies the evolution equations.

For the specification of the lapse function there are several possibilities. A careful study of different conditions has been carried out by Bernstein [15].

The simplest choice is a constant lapse

$$\alpha = 1 \tag{4.14}$$

This choice is called 'geodesic slicing' since grid points correspond to freely falling observers.

The slicing is displayed in a Kruskal diagram in figure 4.1(a). Geodesic slicing is often used to test codes for numerical evolutions of black holes, like e.g. in [25]. For a Schwarzschild black hole a grid point initially on the horizon ($r = 2M$) will hit the singularity in the limited time of πM. Hence, the metric in a numerical evolution will become infinite at this time, causing the 'crash' of the evolution. So this slicing condition only allows for very short evolution times. But the knowledge of the time when the singularity will be hit yields a good test of the implementation of the evolution system.

For long time evolutions one desires a slicing condition which allows for a dynamic evolution of the slice while slowing down the evolution in the vicinity of the singularity. Such the sliced are bent into the past near the singularity. This can be achieved by a lapse function approaching unity for large radii while decreasing in the region near the singularity. Such slicing conditions are called 'singularity avoiding'.

One such slicing which is commonly used is 'maximal slicing'. The name arises from the fact that this condition generates a lapse which maximizes the volume of the hypersurface. Since volume elements decrease when approaching the curvature singularity, a foliation with slices of maximal volume will tend to avoid the singular region.

For slices of maximal volume the mean extrinsic curvature vanishes, $\mathrm{tr}K \equiv 0$. Thus, taking the trace of the evolution equation 4.2 for the extrinsic curvature and considering the vanishing shift and $\partial_t \mathrm{tr}K$ we obtain the equation

$$\Delta\alpha = -\alpha R = \alpha K^{ab}K_{ab} \tag{4.15}$$

where in the last step we applied the Hamiltonian constraint 2.29. This condition on the lapse function is an elliptic equation which has to be solved numerically.

Viewed in a Kruskal diagram, maximal slicings will bent around the $r = 3M/2$ line in Schwarzschild coordinates, which is the limiting slice for this gauge condition. This is displayed in figure 4.1(b). Hence, in an embedding diagram the throat would become more and more stretched while for late times the radius of the throat will be constant. Also for maximal slicing grid points are falling into the black hole.

Since the numerical solution of an elliptic equation is time consuming a promising alternative to maximal slicing are 'algebraic slicings'. These utilize the property of the metric as a measurement of the volume element. The determinant γ of the metric can be regarded as an infinitesimal volume element, which becomes smaller in the region of the singularity.
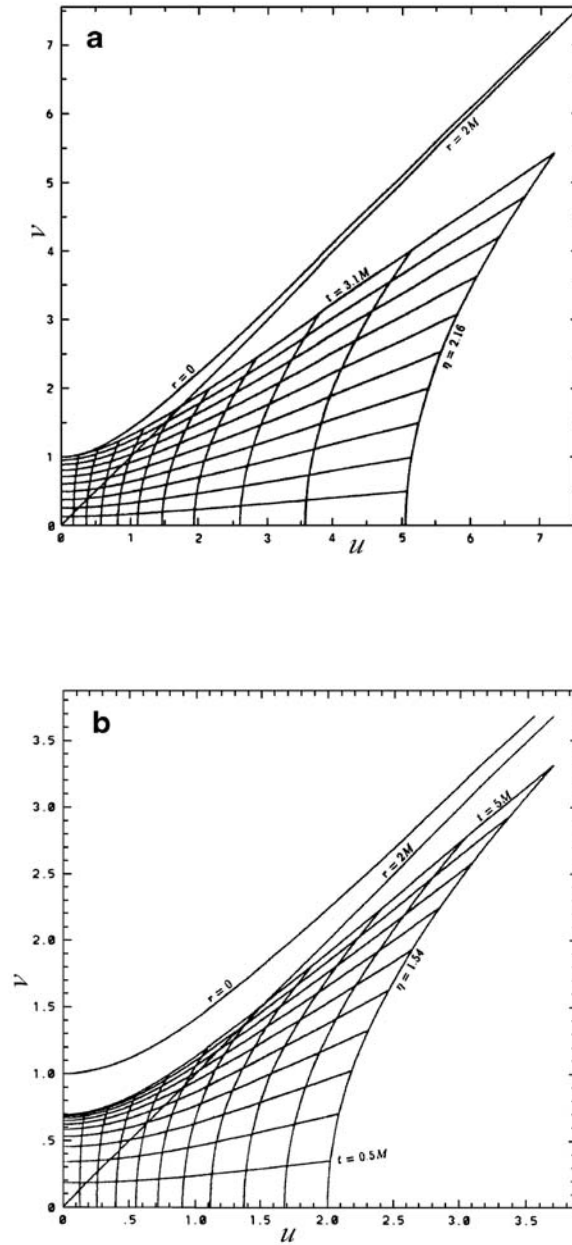
Figure 4.1: Kruskal diagrams showing (a) slices for geodesic slicing and (b) slices for maximal slicing. The slices are evenly spaced in time (from [15]) and the trajectories are displayed with evenly spacing on the radial coordinate η given by $r = 2M \cosh^2(\eta/2)$ where r is the radius in Schwarzschild coordinates.

This can be employed to control the lapse function by considering an algebraic relation between the determinant of the metric and the lapse function

$$\alpha = f(x^a)g(\gamma) \tag{4.16}$$

where $f(x^a)$ is an arbitrary function of the spatial coordinates x^a and $g(\gamma)$ is a function of the determinant γ of the metric γ_{ab} on the slices.

A common choice is given by the '1+log' slicing

$$\alpha = f(x^a)(1 + log(\gamma)) \tag{4.17}$$

which mimics the action of maximal slicing.

Algebraic slicings do have the drawback that they are calculating the lapse locally. So, if some feature develops at a particular point in the 3-metric, the algebraic lapse responds instantly and locally. This is in sharp contrast to maximal slicing which exhibits non-local character due to the elliptic equation to be solved.

In order to decrease the locality of the algebraic lapse condition we can use an evolution equation for the lapse α which allows for the introduction of diffusion terms. This will smooth out local features of higher frequency leading to a more stable evolution. Thus the condition for the lapse can be expressed as

$$\partial_t \alpha = -\alpha^2 f(\alpha) tr K + \epsilon_1 \Delta_F \alpha + \epsilon_2 \Delta \alpha \tag{4.18}$$

with Δ_F being the flat space laplacian and Δ the curved space laplacian. The variables ϵ_1 and ϵ_2 are the diffusion parameters. The choice of the function f specifies the type of the algebraic slicing. For $f(\alpha) = 1/\alpha$ we obtain 1+log slicing as $\alpha = g(x_i) + log|\gamma^{1/2}|$ with a function g dependent on the initial data. For $f(\alpha) = N/\alpha$ the resulting lapse condition is a 'power log' condition $\alpha = g(x_i) + log|\gamma^{N/2}|$. Several different algebraic slicing conditions have been discussed by Bernstein [15].

The drawback of all singularity avoiding slicing conditions is that the retarded evolution in the neighborhood of the singularity results in a 'stretching' of the grid: The proper distance between neighboring grid points increases which leads to large gradients in the metric functions. This finally causes errors in the numerical evolution and finally the 'crash' of the code.

To avoid the problem of grid stretching it has been proposed by Unruh [50] that an excision of the black hole interior from the numerical grid together with an inner boundary condition should lead to stable evolutions since the large gradients in the metric functions disappear. This technique is referred to as 'black hole excision', or when the inner boundary conditions are applied at the apparent horizon as the 'Apparent Horizon Boundary Condition' (AHBC). The problem is not yet fully solved, but it has been shown in one and two dimensions that this technique works. A review on the AHBC can be found in [53].

4.3   Boundary Conditions

For the evolution of Cauchy data several boundary conditions have to be considered. Appropriate boundary conditions are necessary for the calculation of the lapse function. Further, boundary values for the evolution variables need to be specified.

As described in the previous chapter puncture initial data has the benefit that it can be solved and evolved without inner boundaries. Thus, only outer boundary conditions have to be applied.

A simple choice for the initial lapse of 1+log slicing would be $\alpha = 1$ for the whole computational domain. In the following time steps the lapse would be calculated according to the 1+log slicing. The evolutions in this work which use 1+log slicing utilize a more elaborate form of the initial lapse, which stabilizes the evolution to a high degree. For the first time step a solution for the maximal slicing condition is used. The boundary values for this are given by the Schwarzschild value:

$$\alpha = \frac{1 - \left(\sum_i \frac{m_i}{2|\mathbf{r}-\mathbf{r}_i}|\right)}{1 + \sum_i \frac{m_i}{2|\mathbf{r}-\mathbf{r}_i|}} \tag{4.19}$$

where the sum is over all black holes i with mass m_i and coordinate location $\mathbf{r}_i$. The Schwarzschild value is supported to the maximal solver as a static condition.

The boundary of the evolution variables, which are ϕ, K, $\tilde{\gamma}_{ij}$, $\tilde{A}_{ij}$, and $\tilde{\Gamma}^i$ in the BSSN formalism, can be treated as a static boundary condition. With this the boundary values of all evolution variables and the lapse α are kept at their initial value.

Alternatively 'radiative' boundary conditions are possible. This boundary treatment assumes an outgoing radial wave given by a function g with falloff $1/r$ which is propagating at speed v. Therefore, the boundary value is given by:

$$f = f_0 + \frac{g(r - vt)}{r} \tag{4.20}$$

Since the function g is unknown one considers the time derivative of equation 4.20 leading to the condition

$$\frac{x_i}{r}\partial_t f + v\partial_i f + v\frac{x_i(f - f_0)}{r^2} = 0 \tag{4.21}$$

where x_i is the normal direction to the given boundary. f_0 is chosen to be 1 for the diagonal metric components γ_{ii} and the lapse α, and to be 0 for all other variables. The asymptotic speed v is chosen to be 1 for all evolution variables except the gauge variables $\{\alpha, \phi, K\}$. For these variables the speed is set to be the asymptotic gauge speed (cf. [17])

$$v = \sqrt{N} \tag{4.22}$$

where N is the exponent from the 'power log' slicing described in the last section.

Despite the fact that radiative boundary conditions yield better results than static conditions there will still be errors running inwards from the boundary. However, usually not this error from the outer boundaries but rather the increasing grid stretching cause evolutions to terminate. Thus the technique of black hole excision with inner boundary conditions should really allow for longer evolution times.

Chapter 5

Extraction of Physical Quantities

From the numerical calculations the metric γ_{ij} and the extrinsic curvature K_{ij} on the slices Σ are obtained. Although all the physics is contained within this quantities, they depend on the coordinate system and the gauge in which the system is evolved. This complicates the physical interpretation of the numerical results.

In this chapter I will present several techniques to extract physical information from the numerically generated slices (Σ, γ, K). This will be at first the calculation of the spacetime (ADM) mass together with the computation of linear momentum and total angular momentum of the black hole system under examination. Further I will review algorithms for finding horizons whose existence shows the presence of black holes in the examined spacetimes. Finally the gauge invariant extraction of gravitational waves from numerical evolutions of the black hole systems is reviewed.

5.1   Extraction of Mass and Momentum

5.1.1   The Algorithm for Extraction of Mass and Momentum

The spacetime mass or energy, the linear and the angular momentum can be extracted from the slice (Σ, γ, K) by integration over a sphere of constant coordinate radius r in the limit of an infinite radius which encloses the black hole system. This is possible since, due to the asymptotic flatness of the initial slice, the initial data represents an isolated system of black holes.

As is shown e.g. in [47] the energy or mass of the spacetime (ADM mass) m_{ADM} is given by

$$m_{ADM} = \frac{1}{16\pi} \lim_{r\to\infty} \oint_r \gamma^{ij}\gamma^{kl}(\gamma_{ik,j} - \gamma_{ij,k})n_l d^2A \tag{5.1}$$

where n^l is the unit normal vector to the sphere $(n^l = x^l/r)$ and d^2A the area element.

Similar the linear momentum p^j is given by (cf. [52])

$$p^j = \frac{1}{8\pi} \lim_{r\to\infty} \oint_r (K^{ij}n_i - K^i{}_i n^j)d^2A \ . \tag{5.2}$$

Together the linear momentum p^j and the ADM mass m_{ADM} form a four-vector p^μ with $p^0 = m_{ADM}$ and $p^i = p^i$, i.e. it transforms as a vector. Further p^j and m_{ADM} are gauge invariant under asymptotic coordinate transformations, as is shown e.g. in [55].

The extraction of angular momentum is a more severe problem. We derive an integral for the angular momentum by considering the analogy to the linear momentum p^i. From the general viewpoint, the total linear momentum p^i in the direction of a translational Killing vector ϕ^i of the flat metric is given by [55]

$$p^i \phi_i = p_\phi = \frac{1}{8\pi} \lim_{r \to \infty} \oint_r (K^i{}_j - \delta^i_j tr K) \phi^j d^2 S_i \tag{5.3}$$

with the oriented area element $d^2 S_i$.

In analogy to this the angular momentum vector J^i can be calculated from the same integral 5.3 with ϕ^i being a "rotational Killing vector of the flat metric to which γ_{ij} is asymptotic." [55] This description of the rotational Killing vector is quite ambiguous unless ϕ^i is an exact symmetry (and hence Killing vector) of γ_{ij}. The ambiguity is due to the coordinate gauge freedom of the metric γ_{ij}. Without exact symmetry there is no way to distinguish the action of ϕ^i and the action of an asymptotic gauge transformation on the data as was shown by York in [55]. At least there is a dependence on the origin for constant translations of the origin.

However, for frames in which $p^i = 0$ the angular momentum J^j should be well defined, so that the angular momentum is "intrinsic", as is stated by York. Then the angular momentum is also well defined if the asymptotically dominant term of the extrinsic curvature K_{ij} possesses the form

$$K^{ij} = \frac{3}{r^3} (\epsilon_{kil} S^l n^k n_j + \epsilon_{kjl} S^l n^k n_i) \tag{5.4}$$

with S^l being the intrinsic angular momentum and ϵ_{ijk} the Levi-Civita tensor. This extrinsic curvature defines also the explicit angular momentum term in puncture initial data as described in section 3.4. According to this the angular momentum is well defined for black hole spacetimes with an extrinsic curvature given by equation 3.21 as long as the total linear momentum of the system vanishes. Hence, in this work I will concentrate on black hole systems with vanishing net linear momentum.

With ϕ^j as a tangential vector to the surface of integration it follows from equation 5.3 for the total angular momentum in analogy to equation 5.2 (cf. [56])

$$J_i = \frac{1}{16\pi} \lim_{r \to \infty} \epsilon_{ijk} \oint_r (x^j K^{kl} - x^k K^{jl}) n_l d^2 A \tag{5.5}$$

where x^i is the normal vector to the integration sphere $(n^i = x^i/r)$.

5.1.2   Extrapolation of Extracted Quantities

The integrals 5.1, 5.2, and 5.5 provide the information for the ADM mass, the linear, and the angular momentum. For a numerical implementation the remaining problem is the finite size of the computational domain. At least for three-dimensional problems the limit of large radii is impossible due to limited computer resources.

However, in the computational domain there are two distinct regions. Innermost is the 'multi-pole' region which is the direct neighborhood of the black hole system. The extent of this region depends on the mass of the black holes and their intrinsic momenta. In the example displayed in figure 5.1 the multi-pole region extends out to a coordinate radius of about $r = 10$.
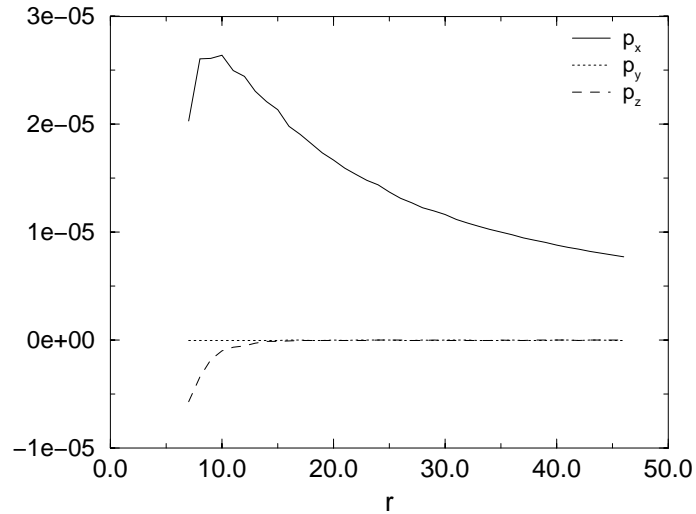
Figure 5.1: Extracted linear momentum components for a system of two black holes. Shown is the dependence on the extracted momentum value in dependence on the coordinate radius where this extraction has been done.

Exterior to the multi-pole region the 'asymptotic' region is located. Here the initial data quantities K_{ij} and γ_{ij} show their behavior of asymptotic decay. Thus, also the extracted values which are derived from K_{ij} and γ_{ij} exhibit an asymptotic behavior. For the linear momentum this is visible in figure 5.1 for $r > 10$. The distinction between multi-pole region and asymptotic region becomes visible for example in the radial dependence on p_x as shown in figure 5.1. However, the distinction between theses regions is not always as obvious as in this example.

Since the asymptotic behavior of the quantities K_{ij} and γ_{ij} is given by

$$f(r) = a + \frac{b}{r} + \frac{c}{r^2} + O(r^{-3}) \tag{5.6}$$

with parameters a, b, and c, also the extracted quantities will show this asymptotic behavior according to the integrals 5.1, 5.2, and 5.5. Thus, we can approximate the radial dependence on the extracted quantities by

$$f(r) = a + \frac{b}{r} + \frac{c}{r^2} \ . \tag{5.7}$$

By omitting terms of higher order on r one should not cause extra error since, at least for the described Robin boundary conditions, the boundary is correct to order $O(r^{-2})$. With this approximation the parameter a gives the extrapolated value of f for $r \to \infty$.

Thus the procedure to extract the asymptotical value for the ADM mass, the linear momentum, and the angular momentum will be as follows:

- First we extract the quantities at different radii large enough to be in the 'asymptotic' region.

- Then we fit the extracted dependence according to equation 5.7 to obtain the value at infinity if the extracted quantity, i.e. its extrapolated value, by reading it off the zero order term a in equation 5.7.
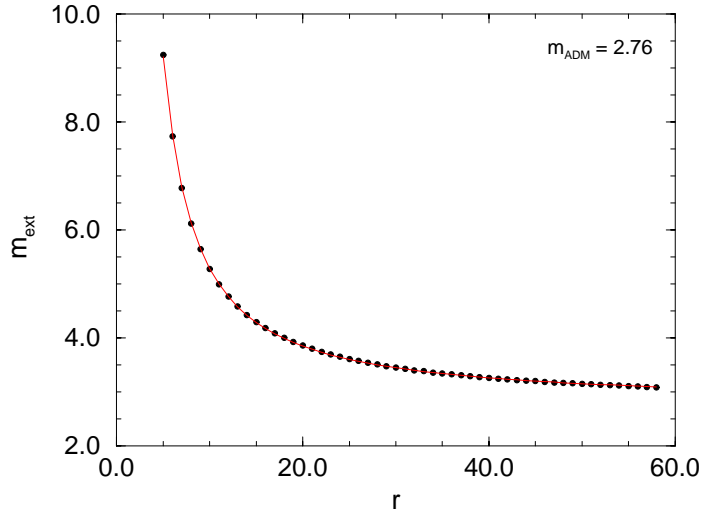
Figure 5.2: Extracted mass m_{ext} for a binary black hole system dependent on the extraction radius compared with the fitted dependence according to equation 5.7. The agreement is excellent.

The integral for the mass extraction had already been coded in one of the *Cactus* thorns. For a better characterization of the black hole systems under examination I added the integrals for both types of momentum. The numerical integration is performed on a Cartesian grid by the introduction of a spherical coordinate system and interpolation of the metric and extrinsic curvature from the Cartesian grid onto a coordinate sphere.

In figure 5.2 the extracted mass for a black hole system similar to that in figure 5.1 is shown. Also displayed is the interpolation according to equation 5.7. The agreement of the curve fit with the extracted behavior is excellent and leads to an extrapolated mass value of $m_{ADM} = 2.76$.

Finally I consider how the boundary treatment in the initial data solver affects the extraction from the initial data and the subsequent curve fitting. In figure 5.3 the radial dependence on the extracted mass m_{ext} for different boundary locations is shown for a binary black hole system with different masses and both linear momentum and spin. Also the extrapolated value of the mass m_{ADM} for different boundary locations and different minimal interpolation radii is displayed. The extraction from data computed with static and Robin boundary conditions is compared.

The major advantage of the Robin boundary condition is obvious. In diagram (b) all five curves of the extracted mass for the different boundary locations are displayed but they are all lying on top of each other. In diagram (a) the static boundary treatment has led to a significant difference in the radial dependence. However, the independence from the boundary with Robin conditions is only true for large grids, as was discussed in connection with figure 3.4.

According to the diagrams (c) and (d) also the extrapolated mass is less dependent on the boundary location for Robin boundary conditions. For a boundary location at $r_{bound} = 16$ the extrapolated mass is only 0.5 percent larger than the mass extrapolated from the extraction

with boundary location at $r_{bound} = 32$. In addition, the extrapolated value settles down very fast to a fixed value of about $m_{ADM} = 3.01$. For static boundary conditions the differences are much bigger. Here the extrapolated masses differ by 4.5 percent in the upper example. Also the extrapolated mass does not settle down as fast as with Robin conditions.

It is obvious that for the different boundary treatments the extrapolated masses differ also for large grids and large minimal extrapolation radii. (In this example by about 5 percent.) This is caused by the fact that the solutions of the initial data solver are distinct due to the different boundary treatments.

In figure 5.4 an analogous examination for the angular momentum is shown for the same initial data set. The basic features are the same as in the case of mass extraction. However, the agreement of the extraction for Robin boundary conditions is worse with about 4 percent mass difference in the upper example. For larger grids and minimal interpolation radii the settling of the extrapolated value is slower. However, also the angular momentum can be extracted to within 1 percent for larger grids.

5.1.3 Validation of the Procedure for a Single Black Hole

In the preceding section I examined the boundary dependence on the extraction for a system where the analytic values were unknown. Now I will examine and validate the formalism with the test case of initial data which represents a single black hole with known values of the extracted quantities. Again the two different boundary treatments are compared.

In figure 5.5 the extracted and extrapolated mass m_{ADM} dependent on the intrinsic mass M of a black hole for vanishing linear momentum and spin is displayed. The solid line shows the expected linear behavior of the mass. For an intrinsic mass up to $M = 10$ the mass m_{ADM} shows the linear dependence, too. For larger intrinsic masses the extracted mass shows a non-linear behavior where the extracted mass value becomes reasonably bigger than the expected mass value. This is due to the fact that the multi-pole region grows for increasing intrinsic masses shifting the extraction into the multi-pole region. The behavior is about the same for both boundary treatments. The influence of the boundary location can be made visible by considering an extraction much further out. This is included in figure 5.5 for the extracted mass of data computed with the outer boundary at $r_{bound} = 144$ but the same grid spacing and a minimal interpolation radius of $r_{min} = 60$. In this case the difference to the intrinsic mass is much smaller and it will still diminish when one increases the minimal interpolation radius.

The extraction of the linear momentum can be studied from figure 5.6. Analogous to the examination of the mass the extracted momentum p_x is shown in dependence on the intrinsic momentum P_x of a single black hole. The right momentum is again only extracted for small intrinsic momenta. With applied Robin boundary conditions the correct value is given with an accuracy of 1 percent up to an intrinsic linear momentum of $P_x = 17$. The deviation when static conditions are applied is much bigger, leading to an error of about 29 percent for $P_x = 17$.

The extraction of angular momentum is displayed in figure 5.7. Here the extracted angular momentum J_x is shown in dependence on the value of the spin parameter S_x. In this case the extraction from initial data computed with Robin boundary conditions is again much better than with static conditions. The extraction errors are of the same order as for the extraction of linear momentum.
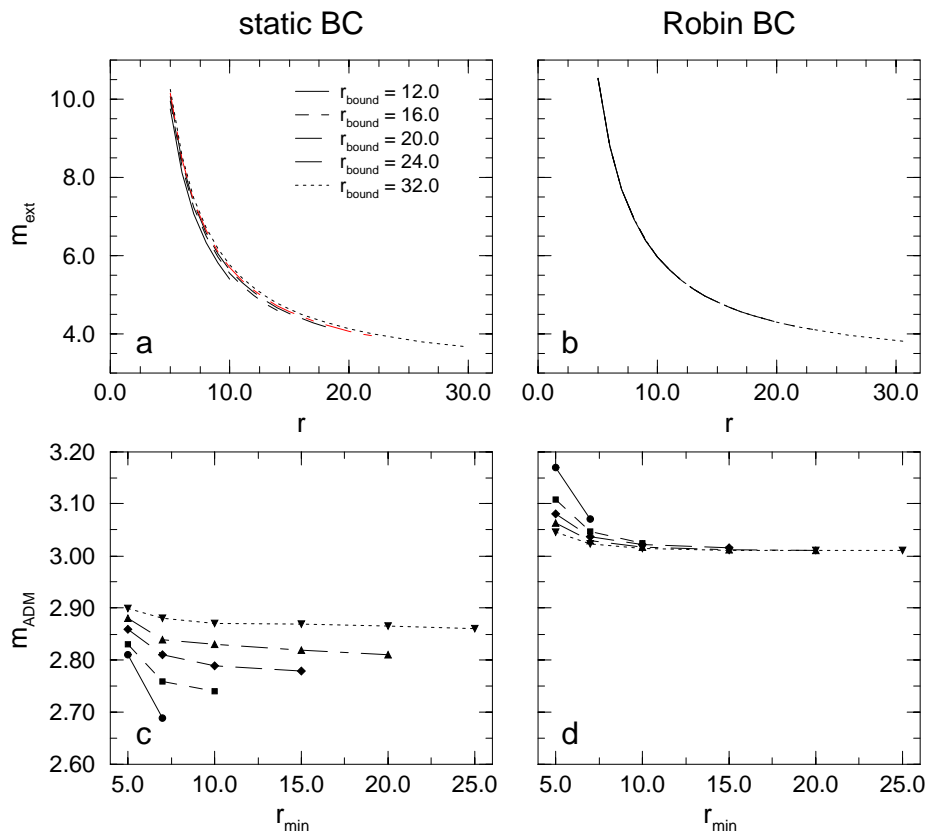
Figure 5.3: Extracted and extrapolated mass for a binary black hole system with masses $M_1 = 1.5, M_2 = 1.0$, linear momenta $\mathbf{P} = (\pm 1.5, 0, 0)$, and spins $\mathbf{S}_1 = (-0.5, 0, -0.5)$ and $\mathbf{S}_2 = (0, 1.0, -1.0)$. Displayed is the dependence on the location of the boundary and the minimal interpolation radius. The extracted mass m_{ext} for different boundary locations is displayed in (a) for static boundary conditions and in (b) for Robin conditions. The bottom diagrams show the extrapolated ADM mass m_{ADM} for different boundary locations and different minimal interpolation radii. (c) shows the dependence for static conditions and (d) for Robin ones. All calculations have been done with a resolution of $h = 0.5$.
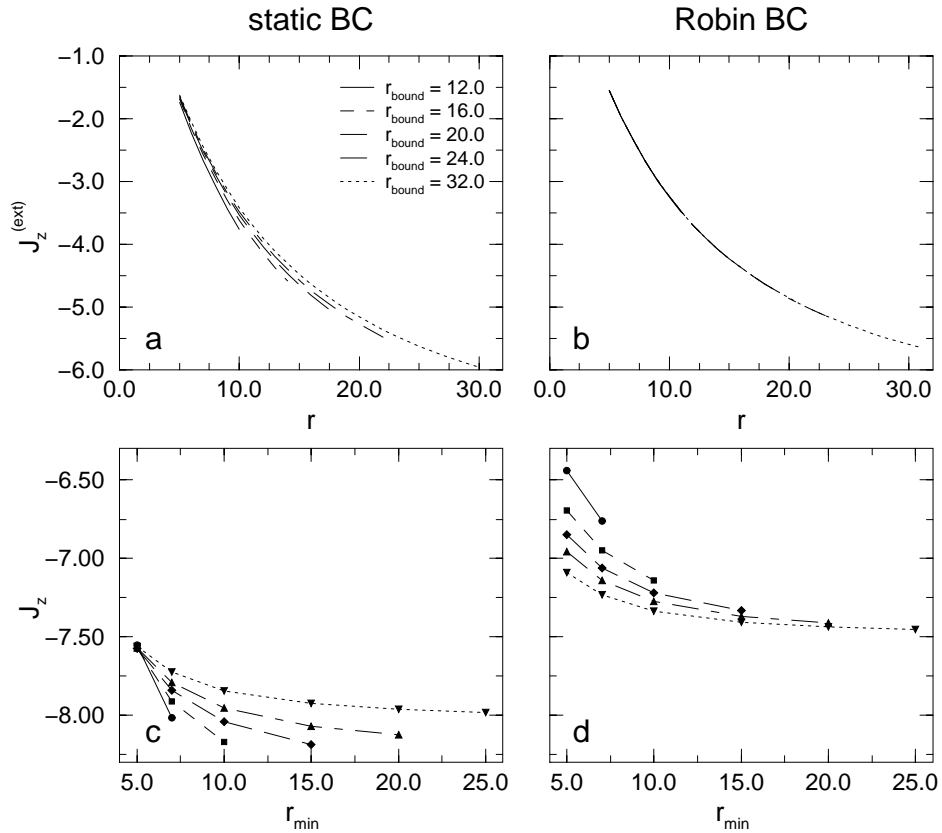
Figure 5.4: Extracted and extrapolated total angular momentum J_z for the same binary black hole system as in the previous figure. Shown is the extracted value $J_z^{(ext)}$ in dependence on the boundary location in (a) for static boundary conditions and in (b) for Robin conditions. Below the z-component of the extrapolated angular momentum J_z for the different boundary distances and different minimal radii of the extrapolation is displayed. (c) shows the dependence for static and (d) for Robin boundary conditions. The resolution of all calculations was $h = 0.5$.
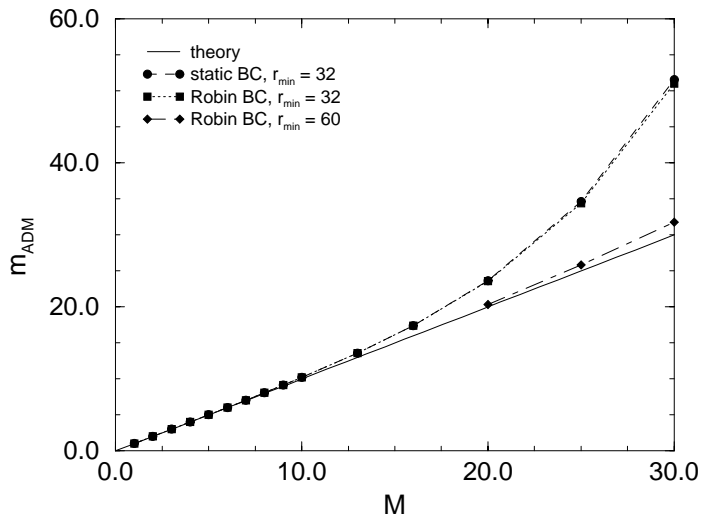
Figure 5.5: Extracted mass m_{ADM} in dependence on the mass parameter M for the single black hole initial data computed with static and with Robin boundary conditions. Also shown is the theoretical linear mass dependence. The resolution of all runs has been $h = 0.75$; the boundary has been at $r_{bound} = 60$ for the minimal curve-fitting radius of $r_{min} = 32$ and at $r_{bound} = 144$ for $r_{min} = 60$.
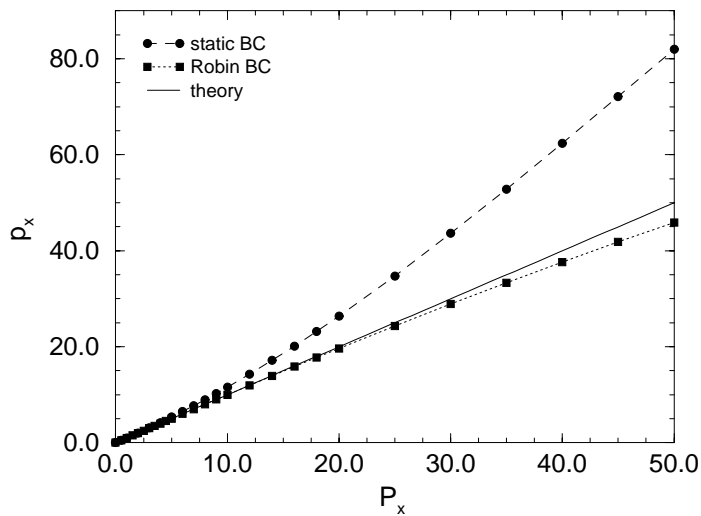

Figure 5.6: Extracted linear momentum p_x for the single black hole dependent on the momentum parameter P_x. The extracted value for initial data computed with static and with Robin boundary conditions are compared with the theoretical linear momentum dependence is shown. The boundary location was $r_{bound} = 60$ while the minimum radius of the curve fitting was $r_{min} = 32$.
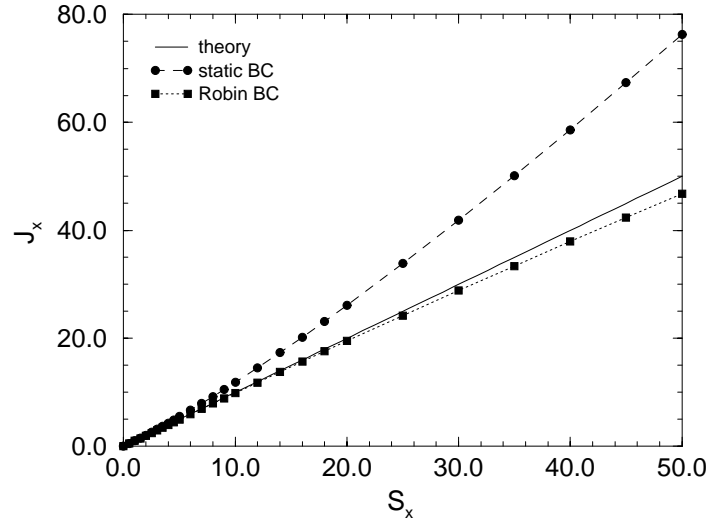
Figure 5.7: Extracted angular momentum for the single black hole for varying spin an the black hole computed for static and Robin boundary conditions. For comparison the theoretical linear spin dependence is shown, too. The configuration of the grid was identical with the study of the linear momentum dependence.

In conclusion from this examination, I will focus on initial data computed with Robin boundary conditions for the extraction of mass and momenta in the next chapter where puncture initial data will be studied.

5.2 Apparent Horizons

Since black holes are defined by the existence of a horizon, it is important to also find horizons in the numerically generated spacetimes. Usually the black hole is defined by the existence of an 'event horizon' (EH) (cf. [39]). The event horizon is defined as the boundary of the causal past of the future null infinity $\mathcal{I}^+$. This is, the event horizon separates null geodesics (light rays) which reach infinity from those which will fall into the singularity. Thus the event horizon is a global property of a spacetime and can numerically only be found if one evolves a black hole system far into the future.

In contrast to the global definition of the even horizon the 'apparent horizon' (AH) is defined locally in time as the outermost marginally trapped surface on a slice. That is, the apparent horizon is defined on a given slice as a surface with a vanishing expansion of outgoing null geodesics [39]. Since there may exist multiple marginally trapped surfaces the outermost one is referred to as the apparent horizon. If an apparent horizon exists an event horizon must exist enclosing it. Thus, the AH guarantees the existence of a black hole, too.

Since in this work the focus will be on initial data and evolutions of full 3D data sets which are currently possible are not long enough for the examination of event horizons, only apparent horizons will be studied here.

5.2.1   Finding Apparent Horizons

To review an algorithm for finding apparent horizons we follow the descriptions by Gundlach [37] and Alcubierre et al. [5]. This algorithm is implemented in *Cactus*.

We want to find an AH on a slice Σ which is a smooth spacelike hypersurface $(\Sigma, \gamma_{ab}, K_{ab})$ embedded in a spacetime $(\mathcal{M}, g_{\mu\nu})$. Let S be a closed smooth two-dimensional surface embedded in Σ and k^μ be a future-pointing null geodesic congruence whose projection on Σ is orthogonal to S. Then for a marginally trapped surface the expansion H of this congruence is:

$$H = \nabla_\mu k^\mu = 0 \tag{5.8}$$

Let s^μ be the outward pointing normal vector on S which is spacelike and normal to the normal n^μ to Σ. Thus, on S we have

$$k^\mu|_S = s^\mu + n^\mu \ . \tag{5.9}$$

Then we can write the expansion H as

$$H = D_i s^i + K_{ij} s^i s^j - tr K \ . \tag{5.10}$$

For a numerical treatment of equation 5.10 we need to parameterize the surface. We can do this using the level set

$$F(x^i) = 0; \qquad s^i = \frac{D^i F}{|DF|} \tag{5.11}$$

which allows us to rewrite H in terms of F and its derivatives. The zero-level of F now defines the marginally trapped surface.

We expect that a single AH has the topology S^2. Hence, we choose

$$F(r, \theta, \phi) = r - h(\theta, \phi) \tag{5.12}$$

and expand the function $h(\theta, \phi)$ in terms of spherical harmonics $Y_{lm}(\theta, \phi)$ up to order l_{max} as

$$h(\theta, \phi) = \sum_{l=0}^{l_{max}} \sum_{m=-l}^{m=l} \sqrt{4\pi} a_{lm} Y_{lm} \theta, \phi \tag{5.13}$$

where we use a real basis of spherical harmonics where terms with $m < 0$ represent an angular dependence $cos(m\phi)$ and terms with $m > 0$ a dependence $sin(m\phi)$. With the factor $\sqrt{4\pi}$ the coefficient a_{00} is the average radius of the surface and a_{10} its average displacement in radial direction.

With this we can start now from a given trial function h and calculate the expansion H via the construction of F. At the points with $r = h(\theta, \phi)$ we interpolate H onto a two-dimensional grid in $\{\theta, \phi\}$ and compute the surface integral of H^2. Using a minimization algorithm we can find the values of the coefficients a_{lm} for which the integral is minimal.

This minimization algorithm is implemented into *Cactus* (see [5] for tests). The drawback is, that the algorithm becomes extremely slow for full three-dimensional horizon searches, in which all m-modes have to be taken into account. Thus, the focus here will be on the fast

flow algorithm as proposed by Gundlach [37], which is faster in the 3D problems examined in this work. However, even with this algorithm finding an apparent horizon is extremely time consuming. In contrast to the one-dimensional case where the horizon is given by an algebraic equation and the two-dimensional case where a simple iteration procedure can be applied [8, 37] the horizon search in 3D is much more complicated. For the studies presented in this work the procedure typically takes about 10 minutes for a single horizon to be found.

The fast flow algorithm, as is detailed in [37], starts from a large sphere as an initial guess and approaches the AH through an iteration procedure given by

$$a_{lm}^{(n+1)} = a_{lm}^{(n)} - \frac{A}{1 + Bl(l+1)}(\rho H)_{lm}^{(n)} \ . \tag{5.14}$$

Here ρ is a 'weight' function and $(\rho H)_{lm}^{(n)}$ are the Fourier components of the function ρH. The iteration step is labeled by (n). A and B are parameters which can be chosen in order to tune the algorithm.

Gundlach names three different choices for the weight ρ:

$$\text{H flow :} \quad \rho \ = \ 1 \tag{5.15}$$
$$\text{C flow :} \quad \rho \ = \ |DF| \tag{5.16}$$
$$\text{N flow :} \quad \rho \ = \ 2r^2 |DF|[(\gamma^{ij} - s^i s^j)(\bar{\gamma}_{ij} - \bar{D}_i r \bar{D}_j r)]^{-1} \tag{5.17}$$

where $\bar{\gamma}_{ij}$ is the flat background metric associated with the coordinates on the Cartesian grid and $\bar{D}$ the corresponding covariant derivative. A and B are usually rescaled as

$$A = \frac{\alpha}{l_{max}(l_{max}+1)} + \beta; \qquad B = \frac{\beta}{\alpha} \tag{5.18}$$

such that α and β are independent of the value of l_{max}.

For the calculations presented in this work typically the weight ρ as defined in equation 5.16 (C flow) and $\alpha = 0.01, \beta = 0.5$ was used. According to Gundlach he obtained the best results using the 'N flow' (equation 5.17). Since this weight was not yet implemented in the horizon finder routine by Alcubierre [5] used in this work, I coded the weight for the 'N flow'. Unfortunately there was no speedup using the 'N flow' instead of the 'C flow' as described above.

The file output of the horizon finder routine consists in an output of the expansion coefficients which allows the three-dimensional reconstruction of the AH. Also the level function F and the expansion H can be written into files as two-dimensional slices along the coordinate planes of the Cartesian numerical grid. Since the expansion H has to vanish for an apparent horizon, the comparison of the zero-level of the quantities F and H allows an visual estimate whether the surface found by the algorithm is really an apparent horizon. The expansion coefficients as well as the level function F represent the shape of the horizon with respect to the curved slice. Thus, images based on these quantities do not represent embeddings of the horizons in Cartesian space.

The particular choice for the parameterization, introduced with equation 5.12, limits the algorithm to find only a single surface of topology S^2. Since I am concerned with binary black hole systems which will merge after finite evolution time I have to cope with topologies different from S^2. However, the topology of a single AH will still be S^2. According to this I changed the implementation in that way that the routine starts the search three times with

a different center of expansion in spherical harmonics and a different radius of the initial trial surface. This allows to find three different surfaces. The found expansion coefficients are written into separate files for each surface while the two-dimensional slices of the level function are simply multiplied for the three searches and written into a single output file. These changes allow to apply the apparent horizon finder routine in evolutions of binary black hole systems. The routine searches for the two separated horizons, one around each puncture, and for the common horizon enclosing both punctures.

5.2.2   Horizon Analysis

After a horizon has been found by the horizon finder algorithm we can analyze its geometry to study physical properties of the black hole data. For this the 2-metric on the surface is calculated and the geometric properties are derived from this.

A measure of interest is the area of the apparent horizon A_{AH}. It can be calculated from the integration over the surface where the area element is given by the square root of the determinant of the 2-metric associated with the surface.

From the horizon area we derive the irreducible mass m_{ir} which is the corresponding mass of a Schwarzschild black hole. It is given by (cf. [22])

$$m_{ir} = \sqrt{\frac{A_{AH}}{16\pi}} \; . \tag{5.19}$$

The apparent horizon mass m_{AH} for a rotating black hole with angular momentum **J** is then given as

$$m_{AH}^2 = m_{ir}^2 + \frac{J^2}{4m_{ir}^2} \; . \tag{5.20}$$

This apparent horizon mass can also serve as a dynamic mass during an evolution.

To study the shape of the horizon some circumferences of the surface can be used. This was often done in axisymmetric studies as in this case one only needs to compare the equatorial circumference with the polar circumference as was done e.g. in [22]. Here the horizon shape is oblate if the equatorial circumference is larger than the polar one and prolate if it is smaller.

However, with full three-dimensional data sets the situation is more complex since no special notion an equator exists. If the vector of total angular momentum of a black hole system is chosen such as to point in the direction of the pole in the spherical coordinate system used in the horizon finder routine (i.e. $\theta = 0$) an 'equator' can be defined. In this case it remains to choose the particular direction (i.e. ϕ-direction) for the calculation of the polar circumference. In the horizon finder routine next to the equatorial circumference C_e the polar circumferences for $\phi = 0$ (C_{p0}) and $\phi = \pi/2$ (c_{pp}) are calculated. Thus, as measures for the shape of the horizons, the ratios

$$C_{r(p0)} = \frac{C_{pp}}{C_{p0}}; \quad C_{r(pe)} = \frac{C_{pp}}{C_e}; \quad C_{r(0e)} = \frac{C_{p0}}{C_e} \tag{5.21}$$

can be considered.

These quantities provide some information on the horizon's shape but the situation can still be ambiguous since we hardly obtain the extremal circumferences in polar direction for surfaces far from axisymmetry.

Horizon dynamics have been studied for evolutions of different black hole initial data sets, usually in axisymmetry like in [8]. However, due to the very high time requirements for the horizon finder algorithm in full 3D it is not yet possible to do such studies in evolutions of data sets without symmetries.

5.2.3 Convergence of the Horizon Finder

Before examining initial data with the horizon finder routine I will study its convergence behavior for analytic initial data.

In figure 5.8 the position of the AH given by the condition $F = 0$ is shown in the three coordinate planes. The initial data is a puncture initial data set representing Brill-Lindquist data of two black holes with masses $M_1 = 1$, $M_2 = 1.5$ located at $c_{1,2} = (\pm 0.6, 0, 0)$ and with vanishing linear and angular momentum. This initial data set is expected to hold a common apparent horizon and has the benefit to be analytical. The location of the AH is displayed for the three resolutions $h = 0.03125$, 0.0625, and 0.125. Visually the difference in the found surface for the three resolutions is very small and the surface seems to converge with the resolution. This is true for the area of the surface as well as for its shape as is shown in figure 5.9 where next to the area also the largest expansion coefficients of the surface are displayed. The difference of the surface area between the coarsest resolution shown, $h = 0.125$, and the finest resolution, $h = 0.03125$, is only of order 10^{-4}.

For a quantitative examination of the influence of the grid spacing on the surface found by the horizon finder algorithm I will consider the convergence of the area as well as of the major expansion coefficients.

The convergence is computed in the following way: A function S can be approximated at any grid point $\mathbf{x}$ and for any grid spacing h by a Taylor expansion with a truncation error of order σ by

$$S(h, \mathbf{x}) = \bar{S}(\mathbf{x}) + h^\sigma \epsilon(h, \mathbf{x}) \tag{5.22}$$

where $\bar{S}$ is the exact solution of the function and $\epsilon(h)$ is a smooth error term of order one in h.

Since the exact solution $\bar{S}$ is generally unknown we can utilize three functions S which are numerically computed at three different resolutions and calculate the convergence from these. For a refinement of b, i.e. the resolutions h, bh, and $b^2 h$, we consider the ratio

$$\frac{L}{M} = \frac{S(b^2 h, \mathbf{x}) - S(bh, \mathbf{x})}{S(bh, \mathbf{x} - S(h, \mathbf{x})} \ . \tag{5.23}$$

With equation 5.22 we obtain at a grid point $\mathbf{x}$

$$\frac{L}{M} = \frac{(b^2 h)^\sigma - (bh)^\sigma}{(bh)^\sigma - h^\sigma} = b^\sigma \ . \tag{5.24}$$

Thus we can calculate the convergence exponent as the three-level convergence σ_3 by

$$\sigma_3(h, \mathbf{x}) = log_2 \frac{S(b^2 h, \mathbf{x}) - S(bh, \mathbf{x})}{S(bh, \mathbf{x}) - S(h, \mathbf{x})} \ . \tag{5.25}$$

where the minus denotes a point-wise subtraction of the values which is only valid if the grid points for the three resolutions coincide. If the grid points do not coincide we can compute
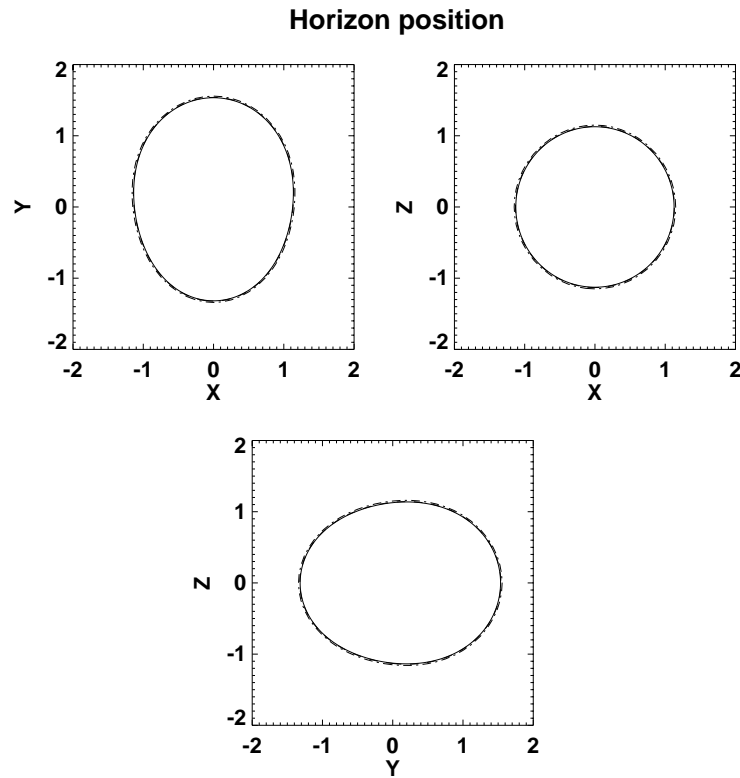
Horizon position

Figure 5.8: Location of the apparent horizon in the three coordinate planes along the axes for Brill-Lindquist initial data with black hole masses $M_1 = 1$, $M_2 = 1.5$ and locations $c_{1,2} = (\pm 0.6, 0, 0)$. The data is computed with Robin boundary conditions for the three resolutions $h = 0.03125, 0.0625, 0.125$.
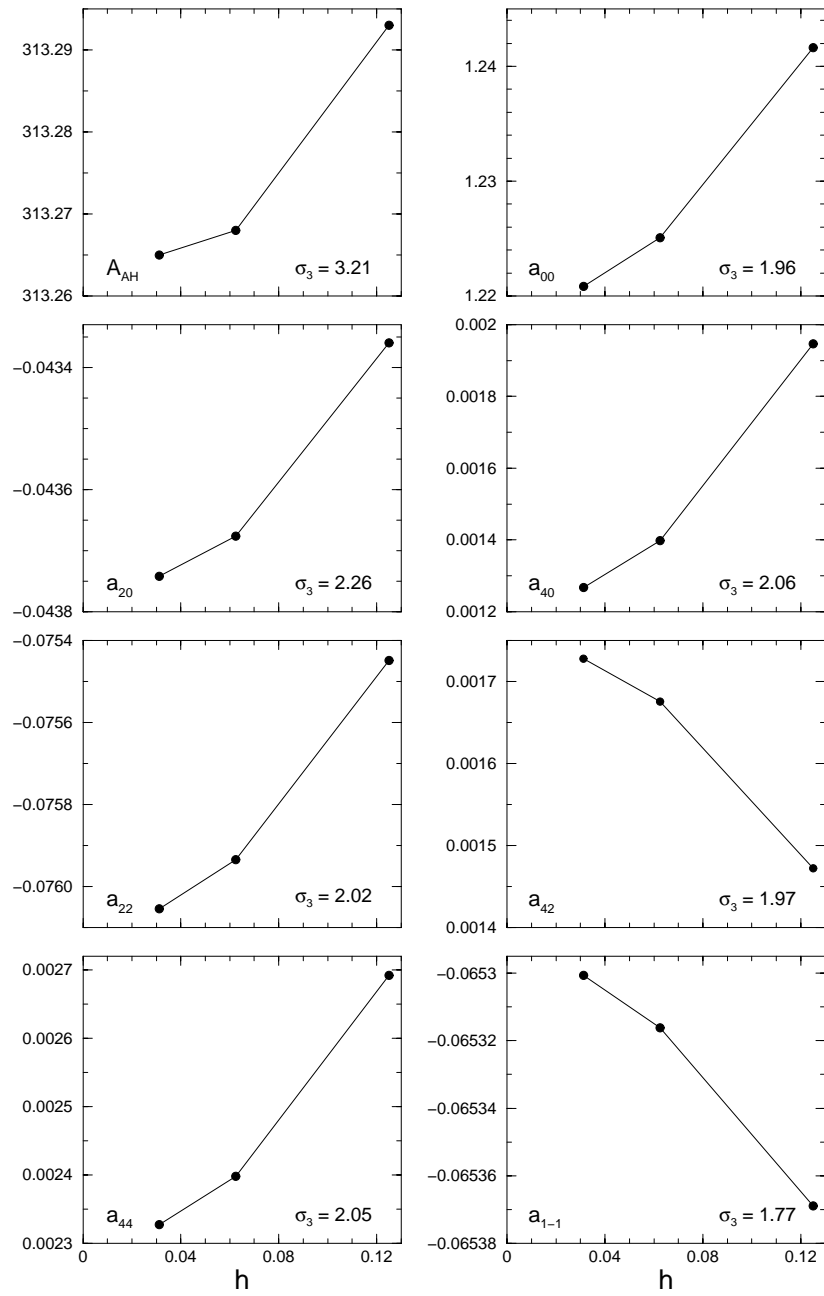
Figure 5.9: Area A_{AH} and major expansion coefficients a_{lm} of the apparent horizon for the same initial data as in figure 5.8. Also shown are the convergence exponents σ_3.

the $l2$-norm of the function first and perform the subtraction afterwards. This leads to a convergence exponent which is position independent.

If the exact solution $\bar{S}(\mathbf{x})$ of the function under examination is known, it suffices to calculate the two-level convergence σ_2 as

$$\sigma_2(h, \mathbf{x}) = log_2 \frac{S(bh, \mathbf{x}) - \bar{S}(\mathbf{x})}{S(h, \mathbf{x}) - \bar{S}(\mathbf{x})} \ . \tag{5.26}$$

This can also be computed with the $l2$-norm of the functions if the grid points do not coincide. From equation 5.26 results that, when the grid spacing is doubled the error must increase by a factor of four and for a grid spacing which is coarser by a factor of four the error increases 16 times.

Equations 5.25 and 5.26 generally allow for the calculation of the convergence exponent. If an algorithm is implemented to be accurate to second order it should show second order convergence. Thus an implementation can be tested in this way, as I will do in section 6.1 with solutions for puncture initial data. Furthermore also the calculation of the convergence in numerical evolutions is possible. As convergence can be lost during an evolution, e.g. due to boundary effects, an evolution can be verified by its convergence. I will do so in chapter 7.

Applied to the apparent horizon area and the expansion coefficients equation 5.25 yields the following result. The convergence exponent σ_3 for the area is $\sigma_3 = 3.21$ and for the expansion coefficients the convergence order is between 1.7 and 2.3. As the initial data is implemented to be second order convergent there should be second order convergence in each coordinate direction. Hence a surface in this data is expected to be convergent to fourth order. Nonetheless, the surface found by the apparent horizon finder algorithm is convergent. Later, in chapter 6, I will study the case of an apparent horizon in initial data which has been calculated numerically.

5.3   Gravitational Waves

As gravitational waves emitted from a system of colliding black holes are of particular astrophysical interest I will examine such waves, which will be extracted from the numerical evolutions of binary black hole systems, in chapter 7. As there are a number of ways to treat the problem of radiation extraction I will focus here on the first order gauge invariant extraction technique developed by Abrahams [2] and is implemented into *Cactus*.

The method uses the fact that the spacetime surrounding a perturbed black hole is basically spherical, with some non-spherical perturbation superposed. This enables us to examine the spacetime applying perturbation theory while it is still evolved fully nonlinear by the numerical code. We can extract two independent wave modes, even- and odd-parity which correspond to two polarization modes of the waves (The odd-parity perturbations have parity $(-1)^{l+1}$ and involve angular momentum). The procedure is detailed in [1].

We assume the numerically calculated metric $g_{\mu\nu}$ to be of the form

$$g_{\mu\nu} = \hat{g}_{\mu\nu} + h_{\alpha\beta} \tag{5.27}$$

where $\hat{g}_{\mu\nu}$ is a static background metric and $h_{\mu\nu}$ a metric perturbation tensor.

The spherical symmetric background metric in general exhibits the form

$$\hat{g}_{\mu\nu} = diag(-N^2, A^2, R^2, R^2 sin^2\theta) \tag{5.28}$$

where N, A, and R are functions of the coordinate radius r and time t.

The non-spherical perturbation tensor for even-parity perturbations is then

$$h_{\mu\nu} = \begin{pmatrix} -N^2 H_0^{(lm)} Y_{lm} & H_1^{(lm)} Y_{lm} & h_0^{(lm)} Y_{lm,\theta} & 0 \\ H_1^{(lm)} Y_{lm} & A^2 H_2^{(lm)} Y_{lm} & h_1^{(lm)} Y_{lm,\theta} & 0 \\ h_0^{(lm)} Y_{lm,\theta} & h_1^{(lm)} Y_{lm,\theta} & R^2 \left(K^{(lm)} + G^{(lm)} \frac{\partial^2}{\partial\theta^2}\right) Y_{lm} & 0 \\ 0 & 0 & 0 & R^2 F Y_{lm} \end{pmatrix} \tag{5.29}$$

with

$$F \equiv K^{(lm)} sin^2\theta + G^{(lm)} \left(\frac{\partial^2}{\partial\theta^2} + sin\theta \, cos\theta \, \frac{\partial}{\partial\theta} \right) . \tag{5.30}$$

The functions $H_0, H_1, H_2, h_0, h_1, K, G$ are referred to as the 'Regge-Wheeler perturbation functions'. They are functions of the radial and the time coordinates only. The Y_{lm} are the usual spherical harmonic functions of order (l, m).

The perturbation functions are determined by projecting the full numerical metric $g_{\mu\nu}^{(num)}$ onto the perturbed metric by integration over a coordinate two-sphere surrounding the source. This utilizes the orthogonality of the spherical harmonics Y_{lm} leading e.g. to

$$\frac{1}{A^2} \oint_S g_{rr}^{(num)} Y_{lm} d\Omega = H_2^{(lm)} . \tag{5.31}$$

Since the metric $g_{\mu\nu}$ is gauge dependent the found perturbation functions are gauge dependent, too. According to Moncrief [46] certain linear combinations of the perturbation functions and their derivatives are gauge invariant. Thus we can construct a gauge invariant function ψ which is a solution to the 'Zerilli equation'. This wave equation describes the propagation of even-parity gravitational waves and reads

$$\frac{\partial^2}{\partial t^2}\psi - \frac{\partial^2}{\partial r_*^2}\psi + V^{(l)}(r)\psi = 0 \tag{5.32}$$

with the 'tortoise coordinate'

$$r_* = r + 2Mln\left(\frac{r}{2M} - 1\right) \tag{5.33}$$

and a gravitational scattering potential $V^{(l)}(r)$.

When we assume the form of A to be $1 - 2M/R$ the gauge invariant function ψ_{lm}^ϵ, the 'Zerilli function', can be written as (cf. [28])

$$\psi_{lm}^\epsilon = \sqrt{\frac{2(l-1)(l+2)}{l(l+1)}} \frac{4RS^2 k_2^{(lm)} + l(l+1)Rk_1^{(lm)}}{l(l+1) - 2 + \frac{6M}{R}} \tag{5.34}$$

for any value of l and m, with

$$S \equiv 1 - \frac{2M}{R} \tag{5.35}$$

and the Moncrief functions

$$
\begin{aligned}
k_1^{(lm)} &\equiv K^{(lm)} + SRG_{,R}^{(lm)} - 2\frac{S}{R}H_1^{(lm)} \\
k_2^{(lm)} &\equiv \frac{H_2^{(lm)}}{2S} - \frac{1}{2\sqrt{S}}\frac{\partial}{\partial R}\left(\frac{RK^{(lm)}}{\sqrt{S}}\right) \; .
\end{aligned}
\tag{5.36}
$$

The energy radiated in each lm-mode is given by

$$
E_{lm}^{(even)} = \frac{1}{32\pi}\int\left(\partial_t\psi_{lm}^e\right)^2 dt \; .
\tag{5.37}
$$

The extraction of odd-parity waves is analogous to the even-parity extraction. The perturbation tensor has a slightly different form and the gauge invariant linear combinations building the odd-parity wave modes ψ_{lm}^o have to fulfill the Regge-Wheeler equation, which is of the same form as the Zerilli equation with a different scattering potential.

The energy emitted from any odd-parity lm-mode is

$$
E_{lm}^{(odd)} = \frac{1}{32\pi}\int(\psi_{lm}^o)^2 dt \; .
\tag{5.38}
$$

The described wave extraction procedure has been implemented into *Cactus* by Allen [6].

Chapter 6

Examination of Puncture Initial Data

Now I turn to the study of puncture initial data. I will focus on data sets representing a binary black hole system with finite linear and/or angular momentum, i.e. initial data with a numerically generated metric due to the numerical solution for the conformal factor, as described in section 3.4. I will study some regions of the parameter space for binary black hole initial data. This will be in respect to the extraction of mass and momentum as well as in the examination of apparent horizons.

As was explained in section 3.4 puncture initial data is defined by the analytical extrinsic curvature given by the sum (eq. 3.22)

$$\hat{K}^{ab}_{BrBr} = \sum_{i=1}^{N} \hat{K}^{ab}_{PS(i)} \tag{6.1}$$

where each term of the is defined by eq. 3.21:

$$
\begin{aligned}
\hat{K}^{ab}_{PS} &= \frac{3}{2r^2}[P^a n^b + P^b n^a - (\hat{\gamma}^{ab} - n^a n^b)P^c n_c] \\
&+ \frac{3}{r^3}(\epsilon^{acd} S_c n_d n^b + \epsilon^{bcd} S_c n_d n^a)
\end{aligned} \tag{6.2}
$$

and by the conformal factor (equations 3.23 and 3.24)

$$\psi = \frac{1}{\chi} + u; \qquad \chi = \sum_{i=1}^{N} \frac{M_{(i)}}{2|\mathbf{r} - \mathbf{r}_{(i)}|} \tag{6.3}$$

where the regular part u is a numerical solution of the elliptic equation (eq. 3.25)

$$\Delta u + \frac{1}{8}\chi^7 \hat{K}^{ab}\hat{K}_{ab}(1 + \chi u)^{-7} = 0 . \tag{6.4}$$

This initial data solves the constraint equations given by 3.1 and 3.2:

$$
\begin{aligned}
ham &\equiv R - K^{ab}K_{ab} &=& \quad 0 \tag{6.5} \\
mom^b &\equiv D_a K^{ab} &=& \quad 0 \tag{6.6}
\end{aligned}
$$

However, in numerical calculations on discrete grids these equations can be violated. This yields a test for the quality of the numerical solution which we will perform below.

6.1   Convergence of the Initial Data Solver

For puncture initial data with finite linear and/or angular momentum the conformal factor
has to be calculated numerically as was described in section 3.4. For the convergence test I
will focus on a particular data set which has already been studied by Brügmann [26]. This
had been done with Brügmanns code 'BAM' which was later ported to Cactus. The multigrid
algorithm for solving the elliptic equation 3.25 is coded to be second order convergent.

The overall scale of all examined data sets will be set by the
mass M_2. Here the data set has the following parameters: masses:
$M_1 = 1.5$, $M_2 = 1.0$, location: $c_{1,2} = (0,0,\pm 1.5)$, linear momentum
$P_{1,2} = (\pm 2,0,0)$, and angular momentum (spin) $S_1 = (0.5, -0.5, 0)$,
$S_2 = (0, -1, -1)$. The orientation of the system and the momenta
and spins is sketched beside. (The sign of the spin components have
been switched here in comparison to [26] since it appeared that in
'BAM' there had been a sign error for the spin part of the extrinsic
curvature. With this switched spin signs I obtain the same data set
as was studied in [26].)
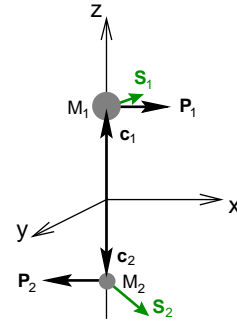
6.1.1   Convergence with Grid Points Next to Punctures

The first convergence check is for data where the grid is chosen in a way that next to the
punctures always a grid point is located in a coordinate distance of just 0.01 along each of
the coordinate axis. Further, static boundary conditions are applied to the elliptic solver.
This should resemble the case which was studied by Brügmann.

The results of the convergence test are shown in figure 6.1. In figure 6.1 (a) the rescaled
metric component γ_{zz}/ϕ^4 is displayed for four different resolutions. There is not really a
tendency to the 'right' metric visible, i.e. a tendency to the metric we would expect theo-
retically for infinite resolution. Rather the three finer grid solutions seem to show the same
metric while the solution on the coarsest grid is clearly distinct. It seems that there is kind
of a 'pathological' resolution below which the multigrid solver for the initial data does not
converge. However, we have also to take into account that for the coarsest resolution there
are only 32 grid points along the z-axis.

In figure 6.1(b) the solution of the Hamiltonian constraint is shown. The solution has
been rescaled under consideration that a resolution coarser by a factor of two should lead to
an error four times as big. Thus due to the rescaling the curves should lie on top of each
other. This condition seems to be fulfilled in a wide range of the computational region. Only
near to the punctures where the extrinsic curvature has its extrema the convergence rate is
smaller. The solution on the coarsest grid is again distinct. Further in the case of the finest
grid there are negative values for the Hamiltonian constraint at the puncture. Obviously the
constraint is not convergent at these points.

An even stronger statement about the convergence can be drawn out of the calculation
of the convergence exponents. In part (c) of figure 6.1 the two- and three-level convergence
exponents are shown calculated from the three coarser grids.

The initial data solver is at best first order convergent at the punctures, since here u is
only C^2 here. This is reproduced as is visible in the diagram where the convergence expo-
nents in the vicinity of the punctures are less than 2 and undefined for the grid points nearest
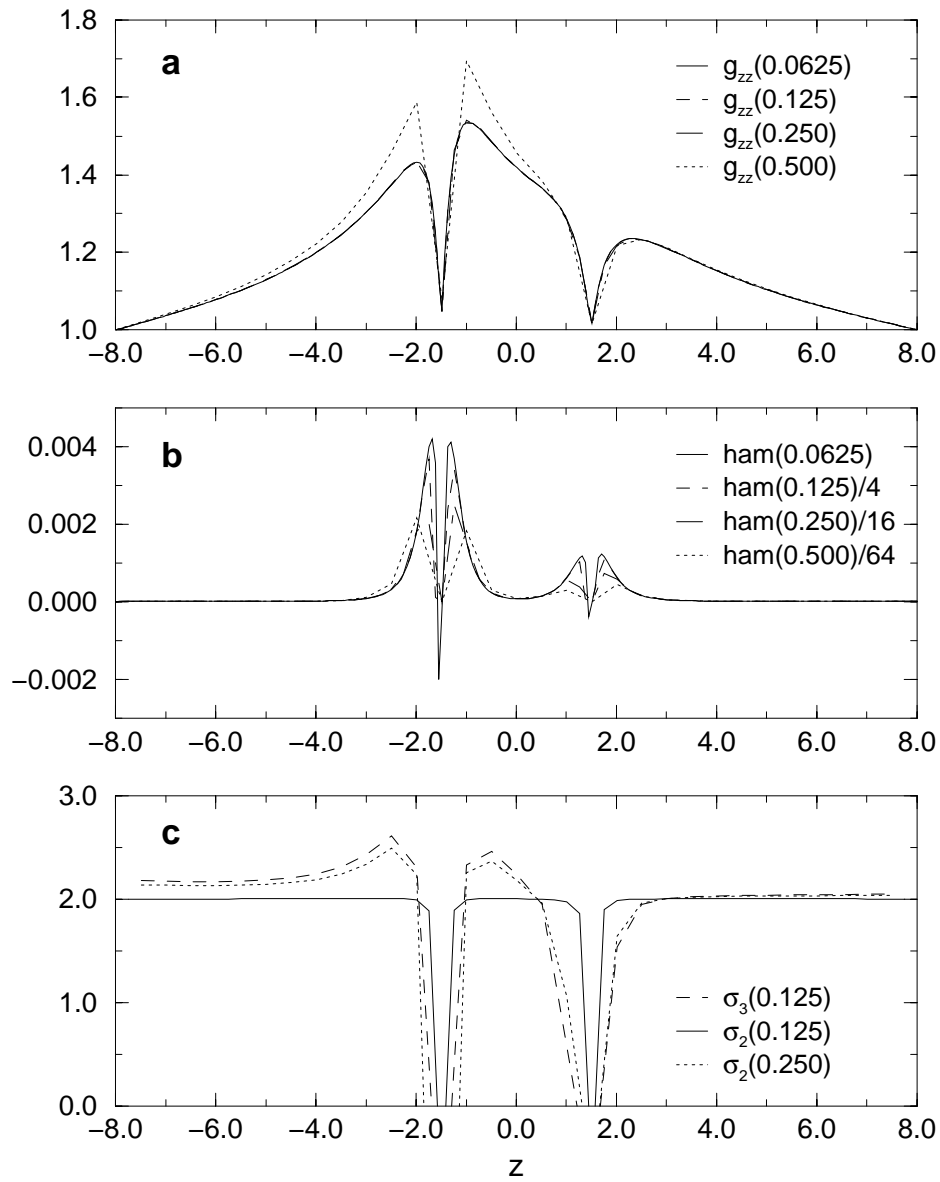
Figure 6.1: Convergence of the binary black hole initial data for grid points 0.01 next to the punctures in the three coordinate directions calculated with static boundary conditions: a) The rescaled metric for different resolutions, b) The Hamiltonian constraint for different resolutions, c) convergence exponents for the Hamiltonian constraint.

to the punctures when the finest grid is considered. The convergence exponents $\sigma_3(0.125)$ and $\sigma_2(0.250)$ which include the coarsest grid in the calculation are clearly distinct from the expected convergence exponent of 2. This is even stronger for negative values of z, the direction where the black hole with the larger mass is located. This effect cannot be seen in diagram (b), since the deviation lies mostly in the region where the Hamiltonian constraint is almost zero. Hence, the difference in the values of the Hamiltonian constraint can not be resolved. However, the convergence exponent $\sigma_2(0.125)$, which does not involve the coarsest grid, shows very good second order convergence in the whole computational domain except in the direct neighborhood of the punctures.

In conclusion this examination of the convergence shows that the solutions for the initial data with the initial data solver implemented in Cactus does not reproduce the results which have been presented in [26]. However, for finer grids, i.e resolutions of $h \leq 0.25$, the solutions are convergent as expected on nearly the whole computational region. But there exists a resolution below which the solution is not convergent any more.

6.1.2   Convergence with Grid Points at the Punctures

In contrast to a configuration with grid points in the direct vicinity of the punctures it is possible to arrange the grid such that grid points will be located directly at the punctures. Analytically the conformal factor ψ diverges at these points but one can avoid this in the numerics by explicitly introducing a very large, but numerically manageable value for the conformal factor at the puncture. In *Cactus* this is done by the choice $\psi|_{puncture} = 5 \cdot 10^{11} M$ with the black hole mass M.

In figure 6.2 the convergence test for the same initial data as in the preceding section is shown. But here grid points are located at the punctures. In this case the rescaled metric component γ_{zz}/ϕ^4, displayed in diagram 6.2(a), is approaching the shape of the metric for the finest grid from the lower side. With finer grids the difference between the solutions decreases. Hence, the solution seems to converge. The rescaled solution of the Hamiltonian constraint also shows a convergent behavior as is displayed in figure 6.2(b). In difference to the case with grid points located near the punctures the solution for the Hamiltonian constraint has no negative values and shows second order convergence over the whole computational domain except in the neighborhood of the punctures. Considering the convergence exponents as shown in diagram 6.2(c) there is a good second order convergence for all examined resolutions. The convergence exponents obtained from the coarser grids are slightly smaller than two.

To conclude, the convergence behavior of the solution for initial data with grid points at the punctures is better defined as that for grid with points near the punctures. The behavior here is comparable to the results of Brügmann [26].

Finally in figure 6.3 a convergence test for initial data with Robin boundary conditions is shown. In this initial data set spin components with flipped signs are used. Thus the initial data is defined by the following parameters: masses: $M_1 = 1.5$, $M_2 = 1.0$, location: $\mathbf{c}_{1,2} = (0, 0, \pm 1.5)$, linear momentum $\mathbf{P}_{1,2} = (\pm 2, 0, 0)$, and spins $\mathbf{S}_1 = (-0.5, 0.5, 0)$, $\mathbf{S}_2 = (0, 1, 1)$. In addition, the boundary is at 18 as opposed to 8 in the two preceding convergence studies. The rescaled metric, displayed in diagram 6.3(a), seems again to be convergent as in the previous convergence study. This is also true for the Hamiltonian constraint in 6.3(b).
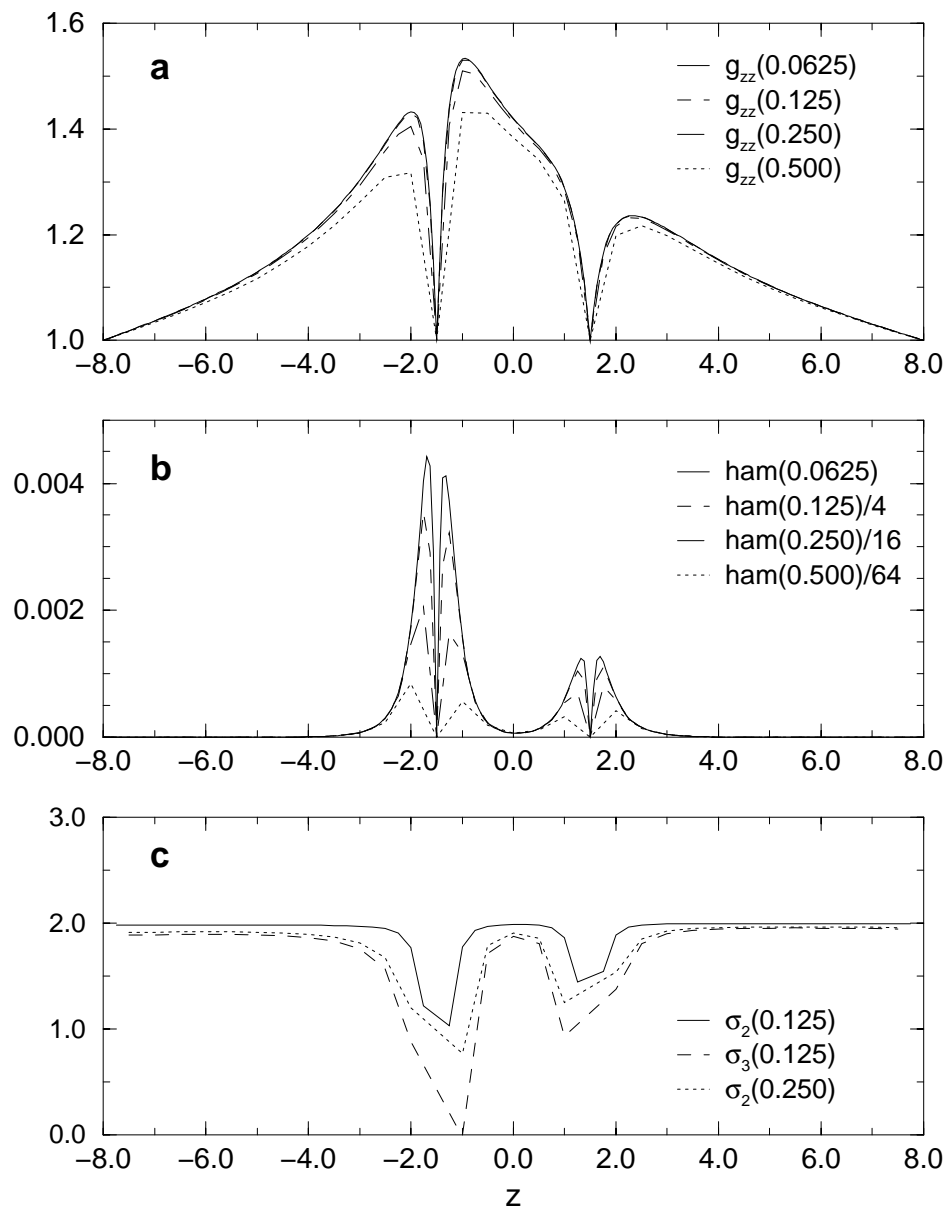
Figure 6.2: Convergence of the binary black hole initial data with grid points on the punctures computed with static boundary conditions: a) The rescaled metric for different resolutions, b) The Hamiltonian constraint for different resolutions, c) convergence exponents for the Hamiltonian constraint.
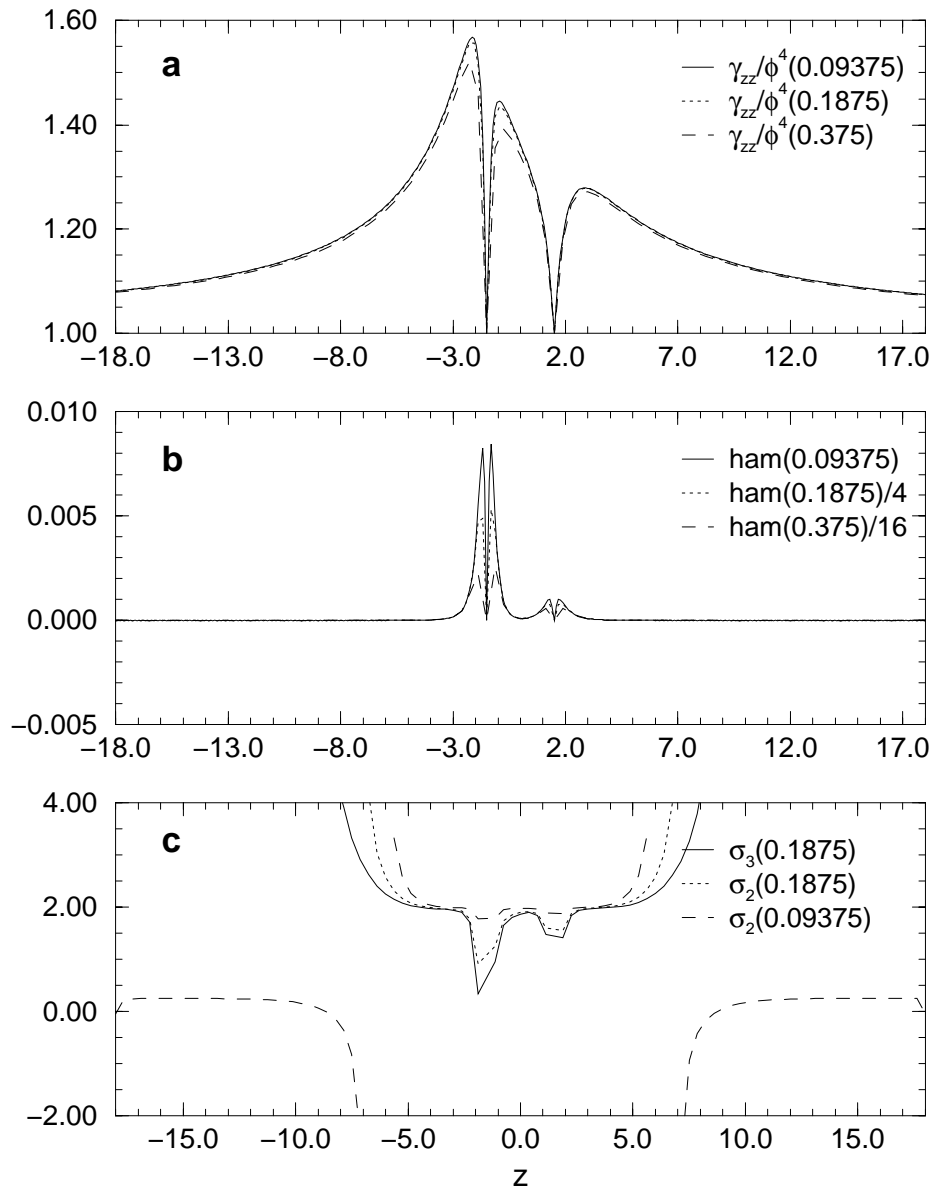
Figure 6.3: Convergence of the binary black hole initial data computed with Robin boundary conditions for grid points located at the punctures: a) The rescaled metric for different resolutions, b) The Hamiltonian constraint for different resolutions, c) convergence exponents for the Hamiltonian constraint.

Diagram 6.3(c) shows the convergence exponents for the Hamiltonian constraint. In the inner region, $z < 5$, of the computational domain the convergence is second order. Further out, where the absolute values of the constraint are already very small, there is a singularity in the convergence exponents resulting from a line crossing of the Hamiltonian constraint values for the different resolutions. That is, when we consider the definition for the three-level convergence (equation 5.25)

$$\sigma_3(h, \mathbf{x}) = log_2 \frac{S(b^2 h, \mathbf{x}) - S(bh, \mathbf{x})}{S(bh, \mathbf{x}) - S(h, \mathbf{x})}$$

is it obvious that the denominator becomes zero when the lines of the constraint for the two finer grids cross each other. Thus, in the limit to the crossing point the ratio becomes infinite. If $S(bh, \mathbf{x})$ is greater than $S(h, \mathbf{x})$ the difference becomes positive infinite at the crossing point. If the crossing point is approached from the other side $S(bh, \mathbf{x})$ does have the smaller value and the difference becomes negative infinite in the limit to the crossing point. This leads to the particular shape of the dependence on the z-coordinate.

Further out in the computational domain only the two-level convergence for the finest grid ($\sigma_2(0.09375)$) is defined, since, due to the line crossing, the ratio in equations 5.25 or 5.26 for the other convergence exponents is negative.

This analysis shows that the convergence in the outer regions of the computational domain differs from that of initial data computed with static boundary conditions when Robin conditions are applied. This particular difference is caused by the form of the Robin condition. As opposed to static conditions, Robin conditions are dependent on the boundary location, which is obvious from equation 3.29. This introduces additional terms in the ratio 5.23 modifying the convergence exponent. However, the deviations from second order convergence in the study done here, occur only in the outer region of the grid, where for example the value of the Hamiltonian constraint is already very small. Since the inner region still converges as expected I will apply Robin boundary conditions for most of the mass and momentum extractions in the next sections and also in the task of evolving the initial data as presented in chapter 7.

6.2   Connection to Analytic Data

The puncture initial data invented by Brandt and Brügmann [20] is a generalization of the analytic initial data sets describing a Schwarzschild black hole and the Brill-Lindquist initial data as was depicted in chapter 3. I will study now how the numerical solution for the conformal factor which has to be computed for finite linear and/or angular momentum emerges from the analytic Brill-Lindquist solution. This will give more insight in the character of this type of initial data.

Due to the finite momentum the analytically given extrinsic curvature will be nonzero. I.e. the initial slice will be curved as embedded in three-dimensional Cartesian space. Furthermore the regular part u of the conformal factor will be different from unity as was already visible in figure 3.4 for a single black hole. Due to the numerical solution of the conformal factor on a discrete grid the Hamiltonian and momentum constraints are expected to be violated at least slightly.

6.2.1   Small Momenta

In figure 6.4 the solution of puncture initial data for small linear mo-
menta is shown. The examined system is a binary black hole system
with the punctures located at $c_{1,2} = (0,0,\pm1.5)$ and vanishing spins on
both holes. The initial data solutions are shown for linear momenta
$\mathbf{P} = (P_x, 0, 0)$ which are oriented collinearly on both holes. That is, the
momentum of hole number 1, located at $c_1 = (0,0,+1.5)$, is $+P_x$ and
the momentum of hole number 2, located at $c_2 = (0,0,-1.5)$, is $-P_x$ as
is sketched in the neighboring figure.
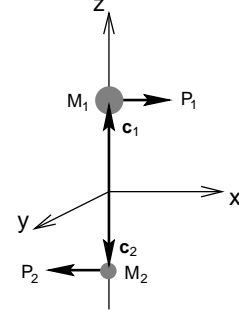
In diagram 6.4(a) the regular part u of the conformal factor in z-direction is shown for
static boundary conditions fixing the boundary value of u to unity. For vanishing linear
momentum the initial data is of the analytical Brill-Lindquist type. Thus it is, according to
equation 6.3, $u \equiv 1$ in the whole computational domain which is also visible in the diagram.
For increasing linear momentum u grows symmetrically about $z = 0$ in the interior of the
computational domain. As expected the maxima of u are at the punctures with a local
minimum between them. This behavior is also reproduced by the rescaled metric component
γ_{zz}/ϕ^4 shown in diagram 6.4(b). The dependence on the maxima of these quantities is non-
linearly on P_x.

Diagram 6.4(c) displays the extrinsic curvature component K_{xz} in z-direction. This com-
ponent is the only one which has finite value along one of the coordinate axes. According to
equation 3.3 it is given by

$$K_{xz} = \psi^{-2}\hat{K}_{xz} \ .$$

K_{xz} is zero for vanishing linear momentum since $\hat{K}_{ij} = 0$ for the whole computational do-
main. For finite momentum K_{xz} becomes non-zero around the punctures. The values of K_{xz}
are linearly dependent on the momentum as can be read off the diagram. At the punctures
the extrinsic curvature is zero due to the division by the square of the conformal factor.

The values of the constraint equations for the initial data with small momenta are dis-
played in figure 6.5. For the analytic case of $P_x = 0$ the constraints are fulfilled by being
zero. For non-zero momentum the constraints are increasingly violated due to the numerical
solution for u. However, the violation is very small and only appears near the punctures. It
is due to the discretization of the grid and are not pointing to a problem with the initial data
solver.

For comparison initial data computed with Robin boundary conditions is shown in figure
6.6. Due to the different boundary treatments the regular part u of the conformal factor
is now also distinct from unity at the boundary and grows with the linear momentum P_x.
Due to this the conformal factor has bigger values in the whole computational domain than
for data computed with static conditions. Also this is true for the metric as is shown by
the metric component γ_{zz}/ϕ^4 in diagram 6.6(b). The extrinsic curvature component K_{xz}
in diagram 6.6(c) is visually not distinguishable from that for static boundary treatment.
However, taking the difference of both quantities shows a difference below 0.02 for $P_x = 0.5$.
This is caused by the different values of the metric components and the conformal factor.

The constraint equations are violated to about the same order as for the initial data com-
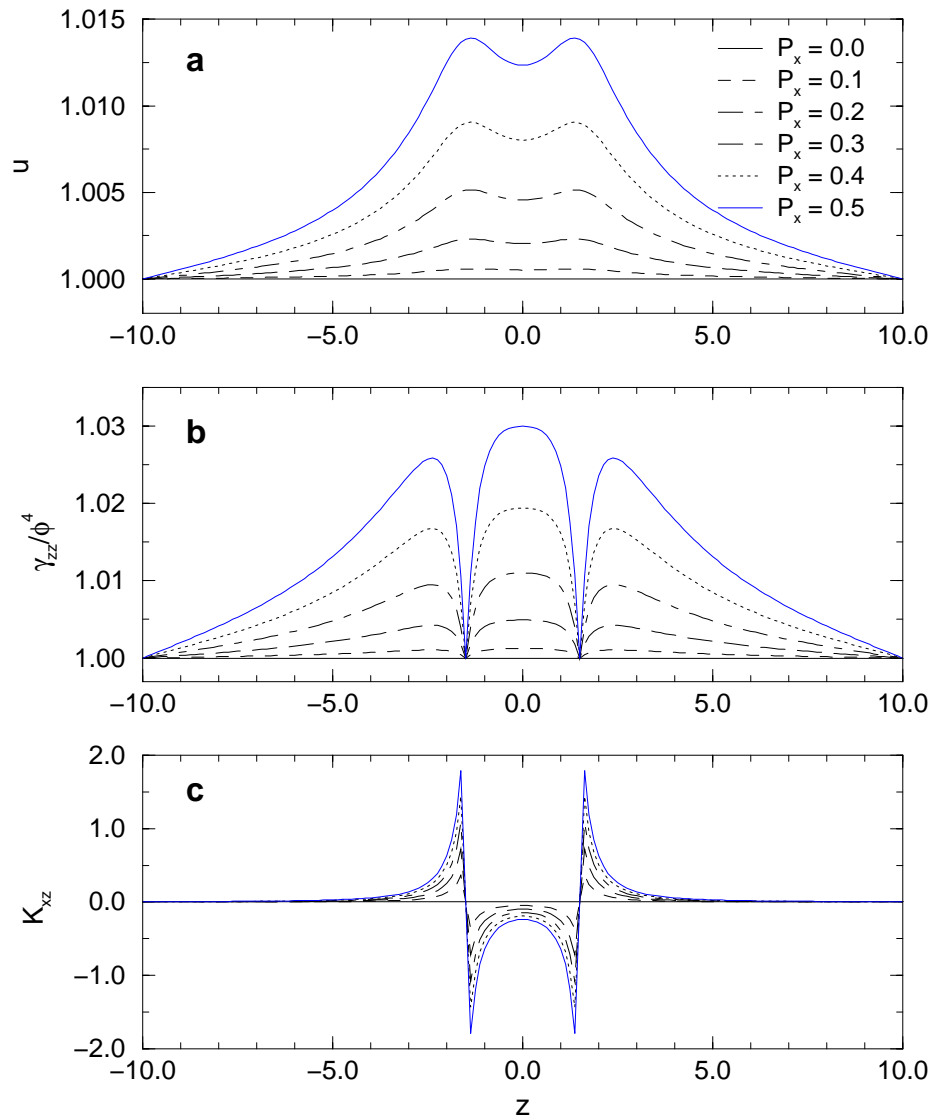puted with static boundary conditions.

Figure 6.4: Solution of the initial data solver for a binary black hole system with small linear momenta in x-direction, P_x, computed with static boundary conditions: a) regular part u of the conformal factor, b) rescaled metric component γ_{zz}/ϕ^4, c) non-vanishing component of the extrinsic curvature.
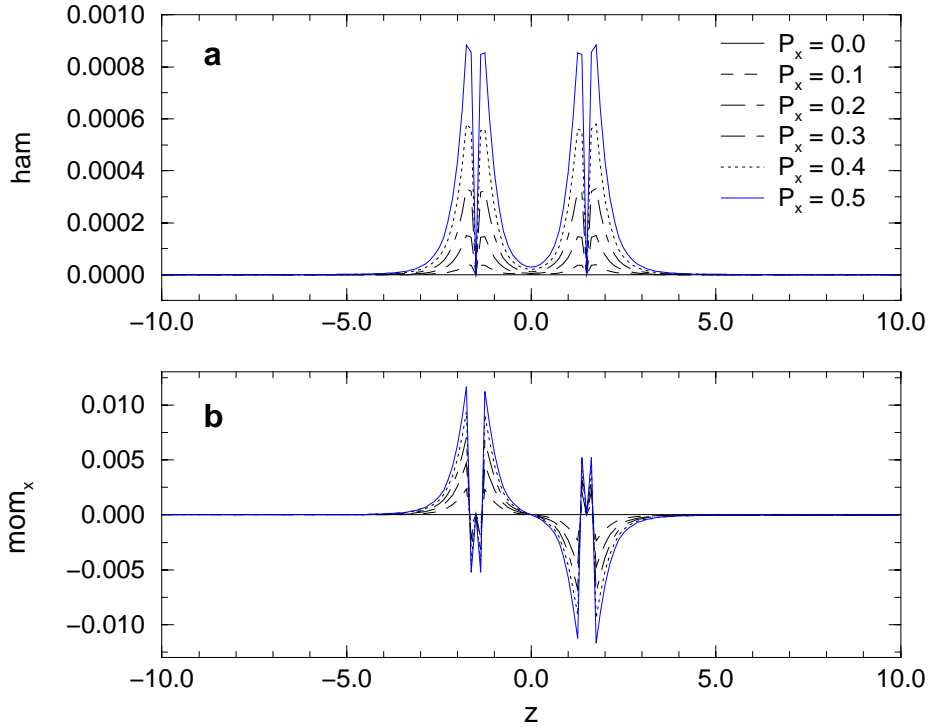
Figure 6.5: Constraints for the initial data for the binary black hole system with small linear momenta in x-direction with static boundary conditions: a) Hamiltonian constraint, ham, b) x-component of the momentum constraint, mom_x.

In figure 6.7 the extracted quantities ADM mass m_{ADM} and angular momentum in y-direction J_y are displayed as a function of the linear momentum P_x. The mass is increasing with the linear momentum in a non-linear way which is to be expected since the mass is calculated from the metric γ_{ij} which itself shows a non-linear dependence on the momentum. In contrast to this the total angular momentum shows a linear increase with the linear momentum. This can be explained by the spin's dependence on the extrinsic curvature.

When we rewrite the part of the extrinsic curvature $\hat{K}^{ij}_{BrBr}$ (cf. equation 3.22) depending only on the linear momentum parameter P^a with reference to the origin, we obtain new terms of $O(r^{-3})$ as was discussed by York in [56]. These terms can be separated into two distinct types:

$$\hat{K}^{ij}_{BrBr} = \hat{K}^{ij}_J + \hat{K}^{ij}_P \tag{6.7}$$

The latter term, $\hat{K}^{ij}_P$, carries no angular momentum while the first one does. It has the form of the normal spin part of the Bowen-York extrinsic curvature (equation 3.21)

$$\hat{K}^{ij}_J = \frac{3}{r^3}(\epsilon^{acd}J_c n_d n^b + \epsilon^{bcd}J_c n_d n^a) \tag{6.8}$$

where r is considered in respect to the origin and the angular momentum $\mathbf{J}$ is given by the classical definition

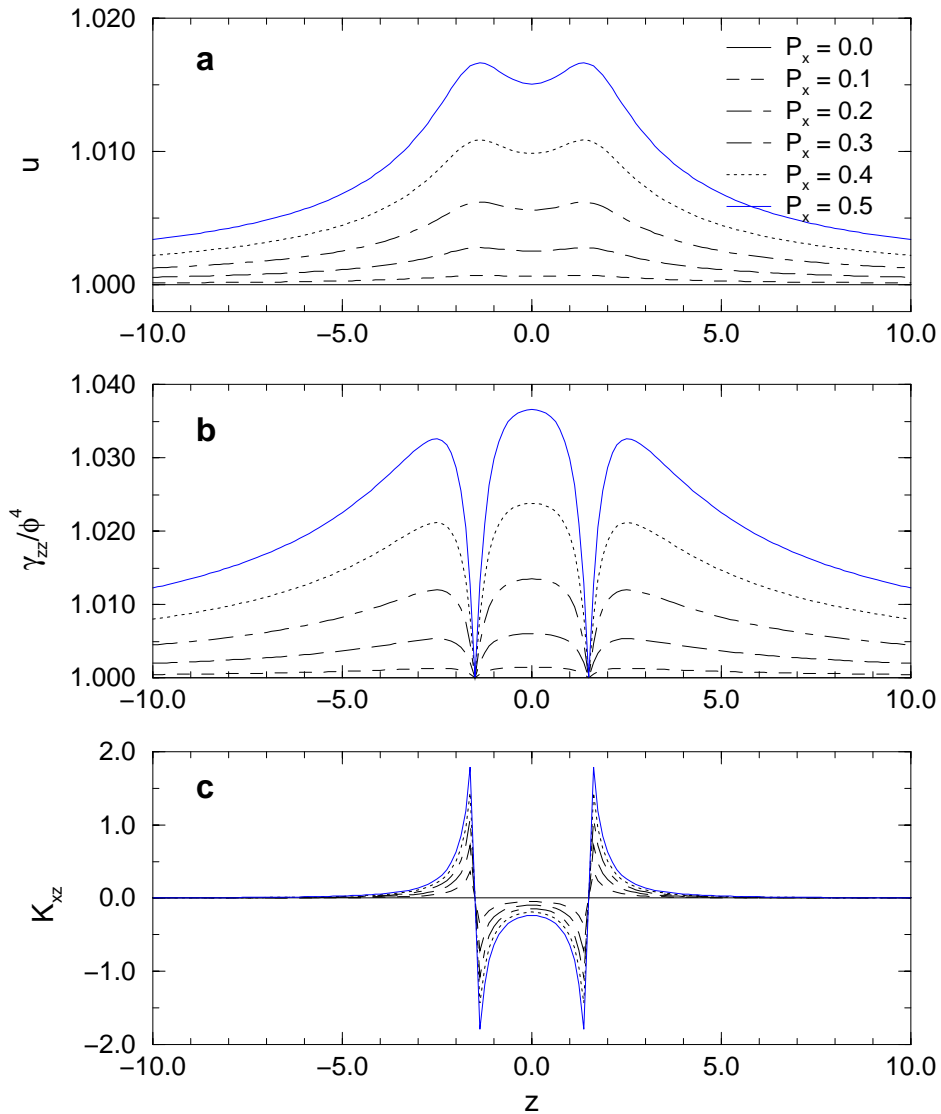$$\mathbf{J} = 2\,\mathbf{c} \times \mathbf{P}\ . \tag{6.9}$$

Figure 6.6: Initial data for small linear momenta in x-direction on the black holes of the binary black hole system computed with Robin boundary conditions: a) regular part u of the conformal factor, b) rescaled metric component γ_{zz}/ϕ^4, c) non-vanishing component of the extrinsic curvature.
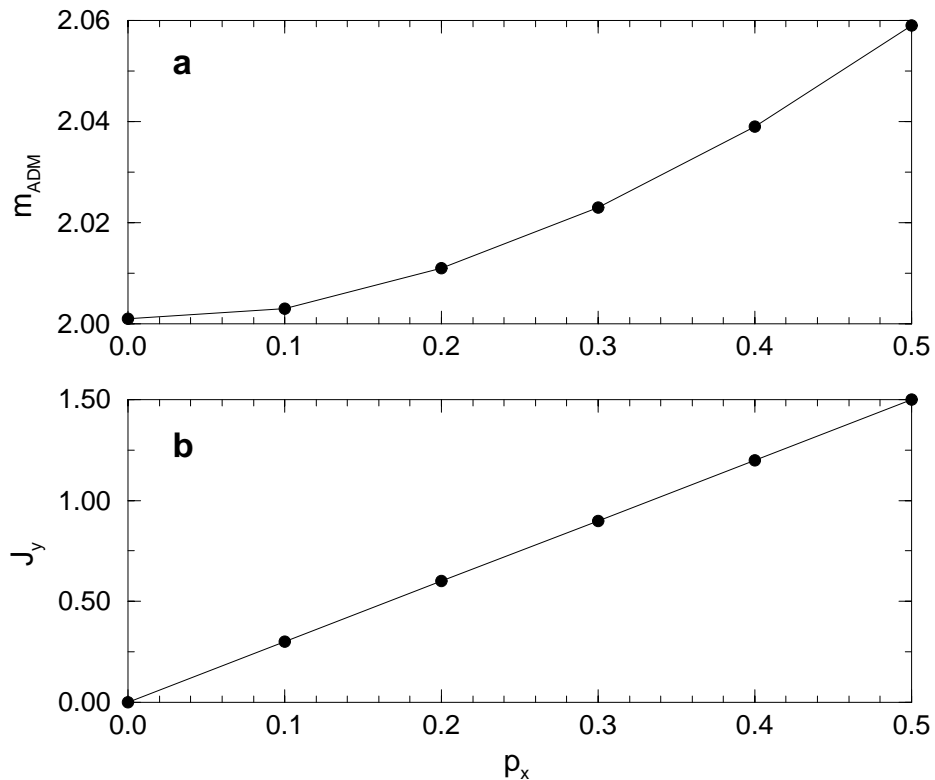
Figure 6.7: Extrapolated ADM mass (a) and angular momentum (b) for puncture initial data representing a binary black hole system with small linear momenta on the black holes. The numerical solution for the conformal factor u was performed using Robin boundary conditions.

This relation is directly reproduced by the extraction as is obvious from diagram 6.7(b).

I will use this relation below to strengthen the confidence in the extraction procedure when considering initial data sets with higher momenta.

The momenta in this study were chosen such that the total linear momentum of the binary system is expected to vanish. The dependence on the extracted linear momentum on the extraction radius for the case of $P_x = 0.5$ was shown in figure 5.1 for the case of. The extrapolated momentum components are less than 10^{-6}. The largest component is p_x, the direction of the intrinsic linear momenta while the two other components are at least two orders less in size.

6.2.2   Small Spins

The alternative to finite linear momentum to obtain non-analytic initial data sets is the application of finite spin on the black holes.

In figure 6.8 the solution for puncture initial data for a small spin S_x on the upper black hole ($\mathbf{c}_1 = (0, 0, +1.5)$) is shown. Diagram 6.8(a) shows the rescaled metric component γ_{zz}/ϕ^4. For increasing spin the metric grows around the location of the upper puncture where also the maximum of the regular part of the conformal factor u locates. The particular shape of the metric is due to the rescaling by ϕ. The values of the Hamiltonian constraint and the y-component of the momentum constraint are displayed in diagrams 6.8(b) and (c), respectively. As expected the constraints are slightly violated in the neighborhood of the upper black hole. Again, there is also a small violation of the constraints in the vicinity of the lower black hole due to the numerical solution of the elliptic equation 3.25. This is directly visible in the Hamiltonian constraint where the violation around the upper black hole is about one order less than around the lower black hole. For the momentum constraint the violation on the lower black hole is a factor of about 10^5 smaller than on the upper black hole.

The components of the extrinsic curvature K_{ab} which are non-zero along the coordinate axes are shown in figure 6.9. In contrast to initial data with only finite linear momentum several components have finite values. This is due to the terms in the extrinsic curvature involving the Levi-Cevita tensor ϵ^{abc} (cf. equation 6.2). The highest curvature is located directly around the upper black hole as displayed by K_{yz} in z-direction the in lower right diagram of the figure.

The quantities due to the extraction procedure are displayed in figure 6.10. The dependence on the ADM mass m_{ADM}, displayed in diagram 6.10(a), is non-linear on the amount of spin, as in the case of finite linear momentum. The total angular momentum (fig. 6.10(b)) has to be linearly dependent on the intrinsic spin. The extraction reproduces this linearity in numerical accuracy. Finally the linear momentum, which should vanish here too, shows no special dependence on the intrinsic spin. Its extracted value is less than 10^{-6}.

6.3   Examination of the Parameter Space

After examining the region of small linear and angular momentum I will now turn to the examination of the parameter space of binary black hole initial data with respect to the extraction of the ADM mass and the momenta.

In general, the parameter space possesses 20 dimensions. Each black hole possesses a location $\mathbf{c}$, a linear momentum $\mathbf{P}$, and a spin $\mathbf{S}$. Since these quantities are vectors with three components each there are ten degrees of freedom for each black hole when we consider also the intrinsic mass M of the hole. Due to symmetries these degrees reduce effectively to 12 degrees of freedom: The orientation of the black holes in the grid is not of interest. Thus the location reduces to one parameter, the coordinate distance d of the punctures. In addition only the mass ratio M_1/M_2 of the holes is important reducing the mass parameters to one. Finally the system has a rotational invariance around the axis connecting the punctures. This adds a further reduction of degrees of freedom by two, one for the linear momentum and one for the spin. I.e. we can specify both spin (or momentum) vectors each in a plane in which the connection line of the punctures lies and choose the angle between these planes.
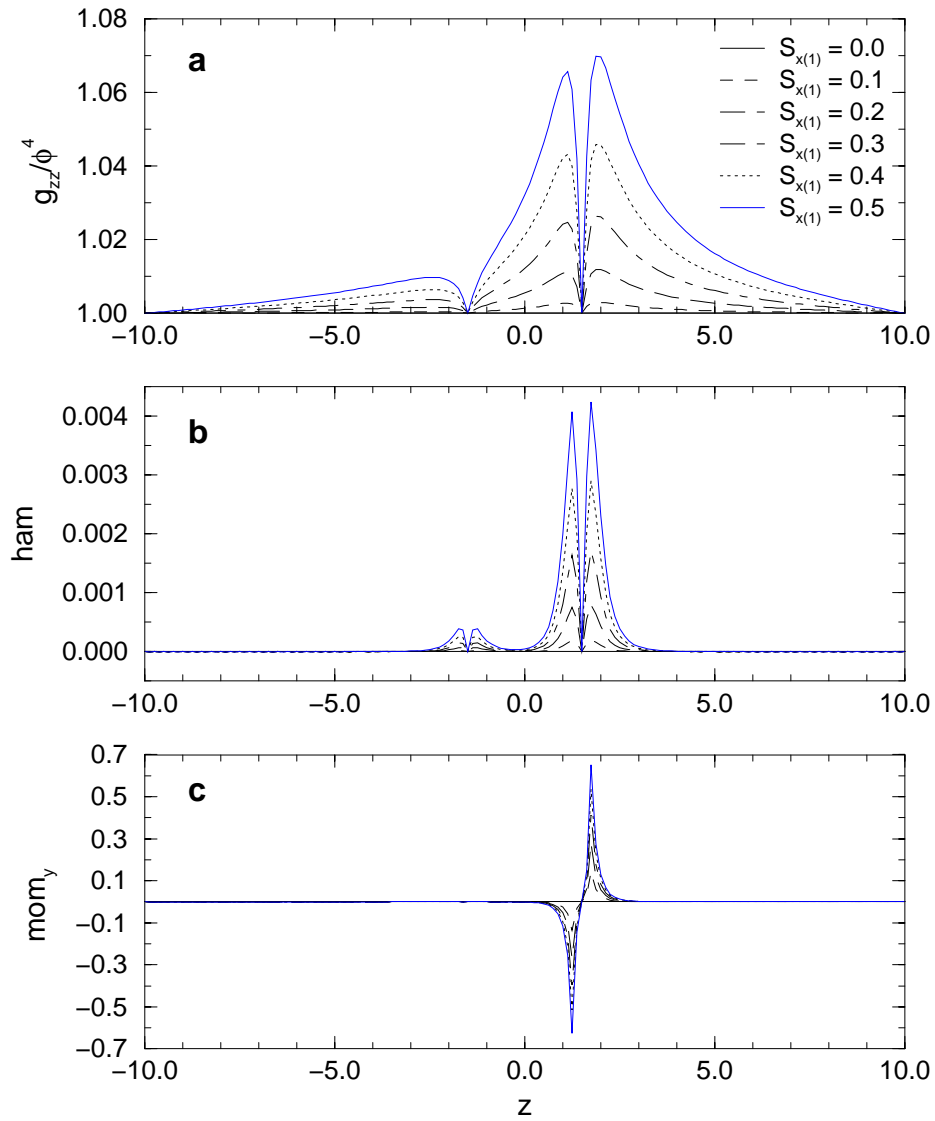
Figure 6.8: Solution of the initial data solver for a binary black hole system with small spin S_x in x-direction on the upper black hole computed with static boundary conditions: a) rescaled metric component γ_{zz}/ϕ^4, b) Hamiltonian constraint ham, c) y-component of the momentum constraint mom_y.
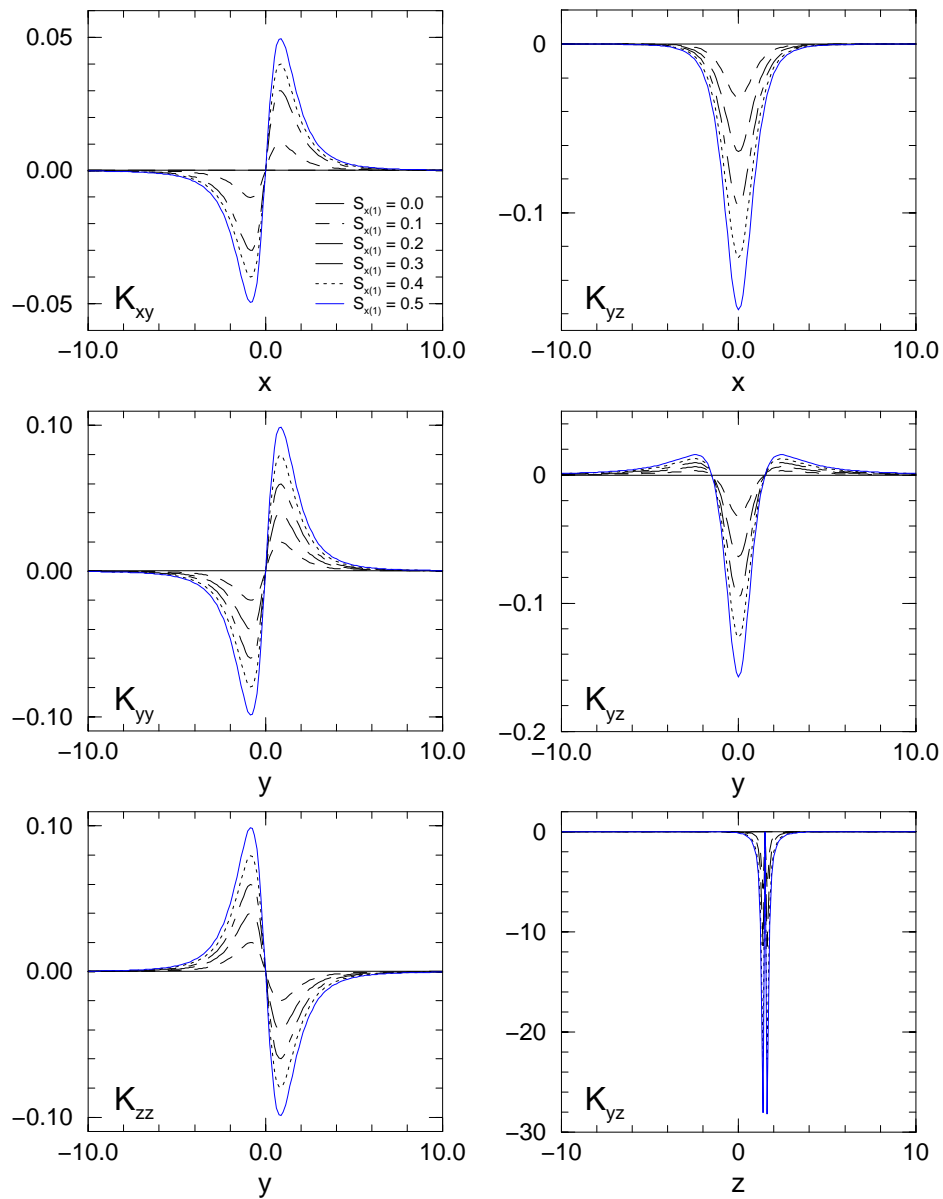
Figure 6.9: Nonzero components of the extrinsic curvature along the Cartesian coordinate directions for the initial data representing a binary black hole system with small spin in x-direction on the upper black hole displayed along the Cartesian coordinate directions.
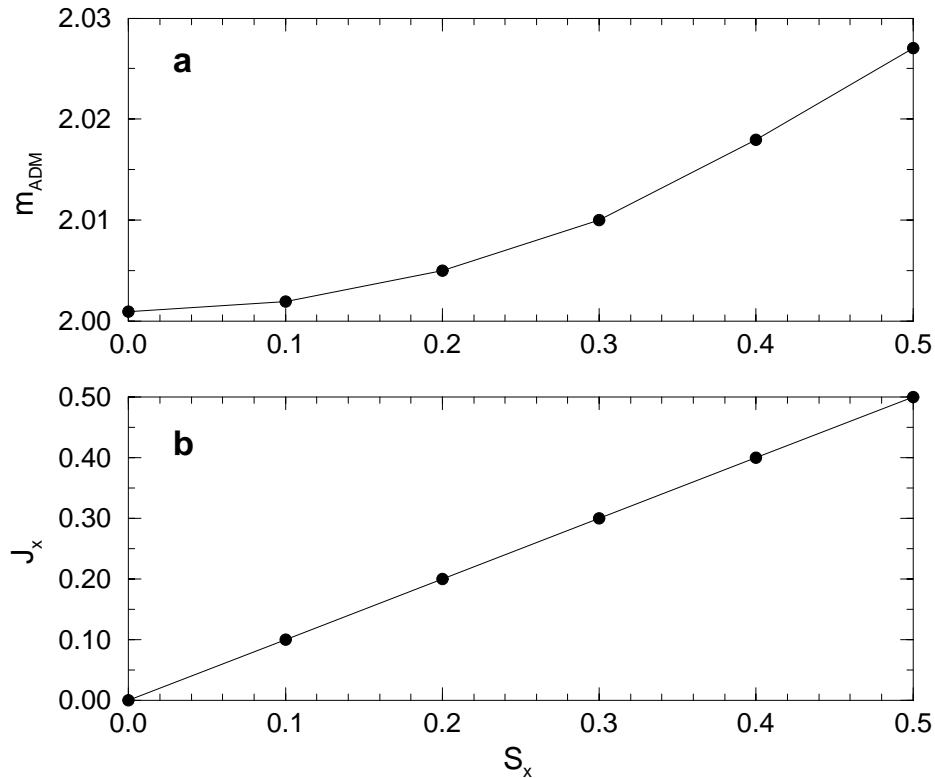
Figure 6.10: Extracted ADM mass m_{ADM} (a) and angular momentum J_x (b) for binary black hole initial data with small spin on the upper black hole.

This large number of degrees of freedom makes it intractable to examine the whole parameter space. Therefore I will focus on some tests to examine areas of the parameter space in order to point out general features and dependencies. Furthermore, in all tests the parameters are chosen such that the total linear momentum of the black hole system vanishes, as this is necessary for the total angular momentum to be well defined as was depicted in section 5.1.1. In particular the linear momentum on each black hole is chosen to be oriented normal to the axis connecting both punctures and the amount of linear momentum is equal for each hole.

I will examine the dependence on the extracted physical quantities on the coordinate separation of the black holes, on the size of the linear momentum, and on the mass ratios and the spin of the holes. Further I will examine the case of large total angular momentum due to high linear momenta on the holes.

6.3.1　Variation of Black Hole Separation

Figure 6.11 displays the dependence on the extracted ADM mass on the coordinate separation d of the punctures for vanishing and for three finite linear momenta.

For vanishing momentum the extracted mass is not dependent on the separation of the punctures. The mass is just the sum of the intrinsic masses of the single black holes as was already shown by Brill and Lindquist [23]. But this is no longer true for systems with finite linear momentum as the mass increases here with the puncture separation. The increase rate
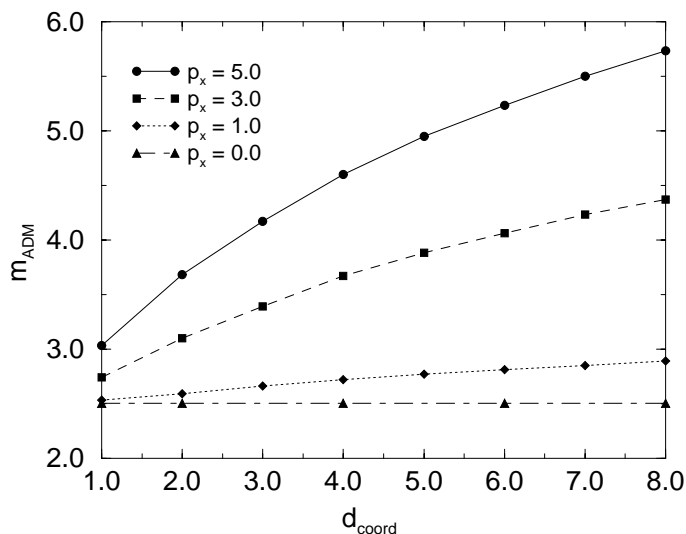
Figure 6.11: Extrapolated ADM mass m_{ADM} in dependence on the separation of the black holes holes for different momenta of the holes.

diminishes with increasing coordinate distance of the punctures pointing to the possibility that, for the limit of very large separations, the mass will approach a constant value. Such a behavior is physically motivated since the mass of a system of two black holes which are so far separated from each other that they are effectively independent will be just the sum of the single black hole masses.

The ADM mass for single black holes with intrinsic masses $M = 1.0$ and $M = 1.5$ can be extracted for $P_x = 3$ to be $m_{ADM} = 3.33$ and $m_{ADM} = 3.55$, respectively. The comparison of the sum of this masses ($m_{tot} = 6.88$) with the extracted mass for the correlated binary system, which is $m_{binary} = 4.4$ for $d = 8$, shows that the correlation of the black holes is still strong at this distance. Hence the correlation will extend much further out. The ratio of these masses is 1.56. Compared to the analogous mass ratio of 1.94 for the data set with $P_x = 5$, it is obvious that the correlation region is increasing with the intrinsic momentum. However, in the numerical simulations which are currently possible such large separations that the correlation is negligible can hardly be reached.

In figure 6.12 the extracted total angular momentum J_z dependent on the puncture coordinate separation d is shown for the three linear momenta $P_x = 1$, 3, and 5. As for the initial data with small linear momentum on the black holes, studied in section 6.2.1, the dependence on the linear momentum is linear as is the dependence on the distance. This reflects again the validity of equation 6.9.

However, for larger distances there is a slight difference to the theoretical value for the angular momentum. This is best visible in the case of $P_x = 5$. Here equation 6.9 yields for $d = 8$ a total angular momentum of $J_z = 40$ but the extracted value is about 39. For $P_x = 3$ and $d = 8$ a small difference is visible, too. But it is smaller, in percentage terms, than for $P_x = 5$. This error is due to the extraction procedure: The masses were extracted with a minimal extraction radius of $r_{min} = 20$. Since the multi-pole region increases with the separation and also with the momenta of the black holes the extraction with constant minimal radius can lead to errors as in this case. This can be prevented by applying larger
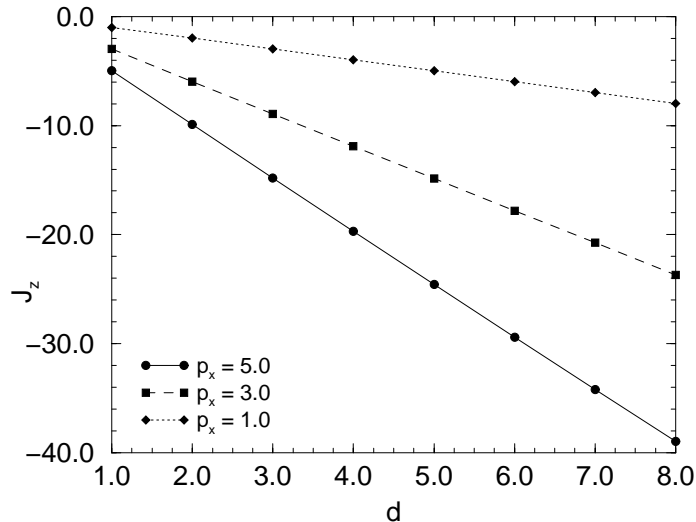
Figure 6.12: Extracted total angular momentum J_z in dependence on the separation of the black holes for different momenta of the black holes.

grids and using a bigger minimal extraction radius which pushes the extraction procedure further out into the asymptotic region.

6.3.2 Variation of Black Hole Momenta

In section 6.2.1 I have shown that for small linear momentum the ADM mass increases non-linearly with the momentum. In figure 6.13 the ADM mass is shown for momenta up to $P_x = 5$ and three different puncture separations. For $d = 5$ and $d = 3$ the mass grow is non-linear for momenta up to $P_x < 1.5$. With higher momentum the mass increases linearly. For $P_x > 3.5$ the slope of the mass curve decreases which is again due to the limited extraction radius.

In contrast to the described linear behavior is the dependence on the mass on the momentum for the case of a coordinate separation of $d = 1$. Here the extracted mass does not show a linear growth with the momentum. This might be caused by the small separation and hence strong correlation of the two black holes. The extent of the region of non-linear mass growth seems to increase with diminishing puncture separation, as is visible in figure 6.13. Thus, it has grown so much in the $d = 1$-case that no real linear dependence on the momentum is visible any more.

The dependence on the total angular momentum J_z on the intrinsic black hole momentum is linear as is shown in figure 6.14. This is expected according to equation 6.9. For larger separations of the punctures the rising extraction error is again visible. The error is about 2 percent for $d = 5$ and $P_x = 5$.

6.3.3 Variation of the Black Hole Mass Ratio

In figure 6.15 the extracted ADM mass is shown in dependence on the mass ratio M_1/M_2 of both black holes. The mass M_2 of the lower black hole will be kept fixed as $M_2 = 1$. Hence, the mass ratio is simply given by the mass M_1 of the upper black hole. Four different distance-momentum configurations have been tested.
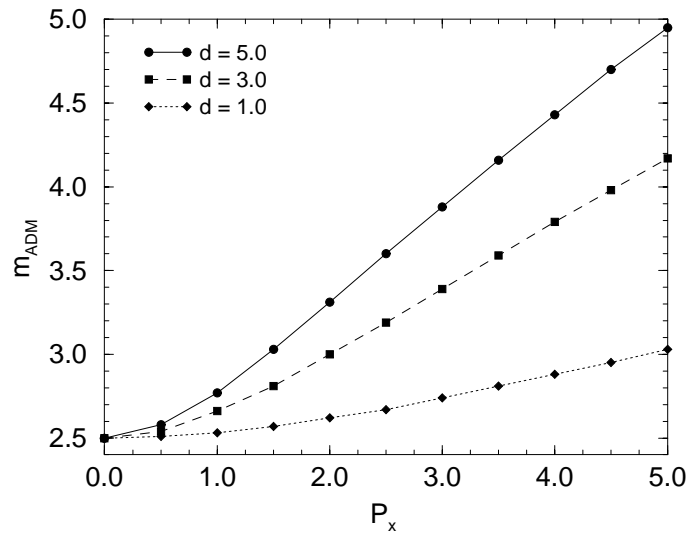
Figure 6.13: Extrapolated ADM mass of the binary black hole system for different intrinsic momenta and three different puncture separations.
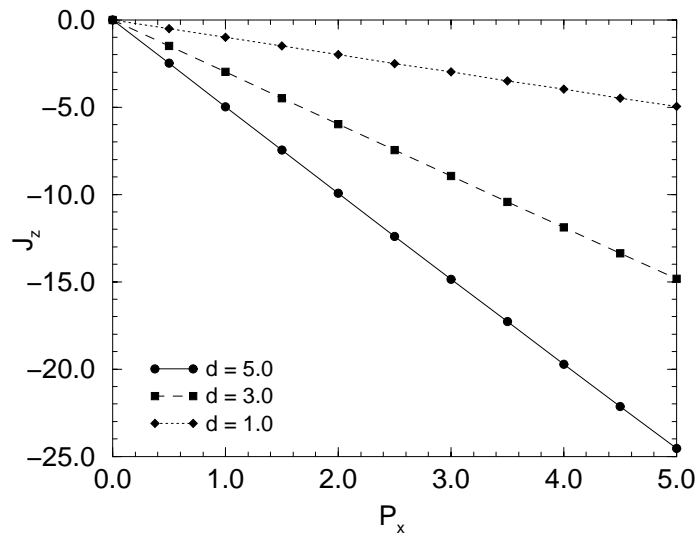

Figure 6.14: Total angular momentum of the binary black hole system for different intrinsic momenta and three different puncture separations.
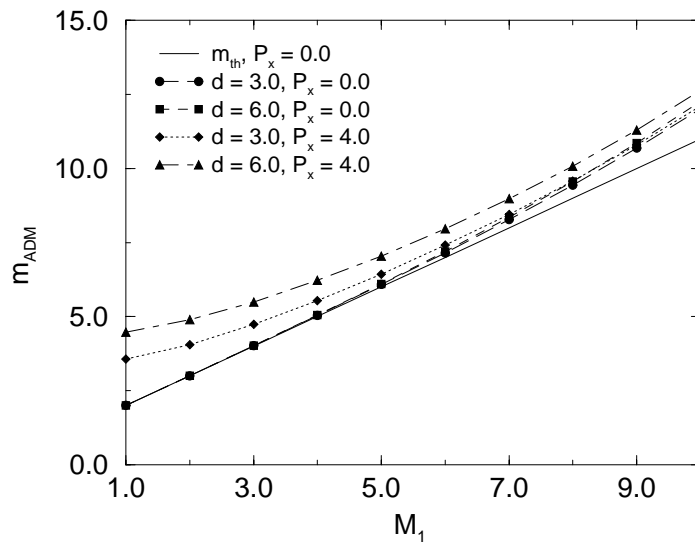
Figure 6.15: Extracted mass of the binary black hole system for different ratios of the mass parameters given by M_1. Displayed are four configurations of puncture separation and linear momentum and the theoretical mass increase for $P_x = 0$.
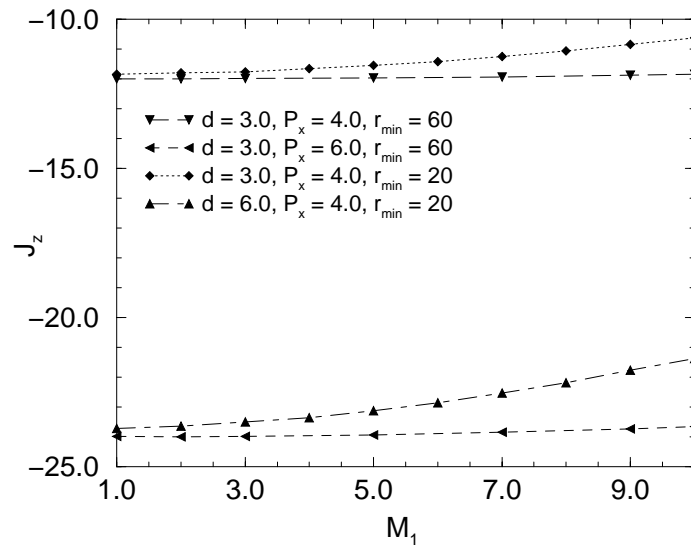

Figure 6.16: Extracted total angular momentum J_z of the binary black hole system for different mass ratios and two puncture separations.

Two cases with vanishing linear momentum are displayed in figure 6.15. For this initial data of Brill-Lindquist type the extracted mass should equal for the two puncture separations $d = 3$ and $d = 6$. This is reproduced up to a small error by the extraction procedure. Since the theoretical mass m_{th}, which is also shown in figure 6.15, is given by

$$m_{th} = \frac{M_1}{M_2} + M_2 = M_1 + 1 \tag{6.10}$$

it is obvious that the extraction error also increases with the mass ratio. The behavior of the extracted mass is analogous to that of the extracted mass for a single black hole, as was presented in section 5.1.3. The extraction error is even bigger for the larger separations of the punctures. For $M_1 = 10$ the error is already about 9 percent for $d = 3$ and 11.5 percent for $d = 6$. These large errors point out that the effect of the mass parameter on the size of the multi-pole region is much bigger than the effect of linear or angular momentum. But larger puncture separations still increase the error.

The extracted masses for finite linear momentum of size $P_x = 4$ show again the mass increase effect with the puncture distance. The masses for both separations are significantly bigger than for vanishing momentum and grow with the puncture separation. The difference to the masses extracted for $P_x = 0$ diminishes with increasing mass M_1. This is due to the fact that the parameter for the Bowen-York extrinsic curvature is the intrinsic momentum, not some velocity. Hence the system is expected to be less 'dynamic' for higher mass ratios and constant intrinsic linear momentum. This causes a mass increase which is smaller than for the initial data with $P_x = 0$. For higher mass ratios the $d = 3$ cases are of comparable mass but the 'dynamic' $d = 6$ case still shows a higher ADM mass than the 'static' ($P_x = 0$) one. This is also due to the growing extraction error which is even bigger for finite momentum and larger puncture separations.

In figure 6.16 the corresponding total angular momentum in dependence on the mass M_1 is shown for the 'dynamic' ($P_x \neq 0$) initial data sets. Since here equation 6.9 with $\mathbf{J} = 2\, \mathbf{c} \times \mathbf{P}$ holds again the expected total angular momenta are $J_z(d = 3) = 12$ and $J_z(d = 6) = 24$. However, for the small minimal extraction radius of $r_{min} = 20$ these values are only reproduced for equal masses. For larger mass ratios the extracted angular momentum decreases due to the wider multi-pole region of the black hole system. The error reaches about 12 percent for both puncture separations for the mass of $M_1 = 10$. This coincides with the large error in the mass extraction.

The results are by far better when an extraction on a much bigger grid is considered. In figure 6.16 also the extraction of angular momentum with a minimal extraction radius of $r_{min} = 60$ on a grid with boundary at $r_{bound} = 96$ is shown. There is still a very small decrease in the amount of extracted spin but the error amounts only to 1.5 percent for $M_1 = 10$.

This analysis shows that the intrinsic black hole masses have a very large influence on the size of the multi-pole region in the slice. Thus an accurate extraction of the mass and angular momentum is only possible on very large computational grids.

6.3.4 Spinning Black Holes

In addition to intrinsic linear momentum I will now examine binary black hole systems which also include intrinsic spin. In figure 6.17 the mass extraction for three different data sets is shown. These data sets possess two punctures located at $\mathbf{c}_{1,2} = (0, \pm 1.5, 0)$ and a mass
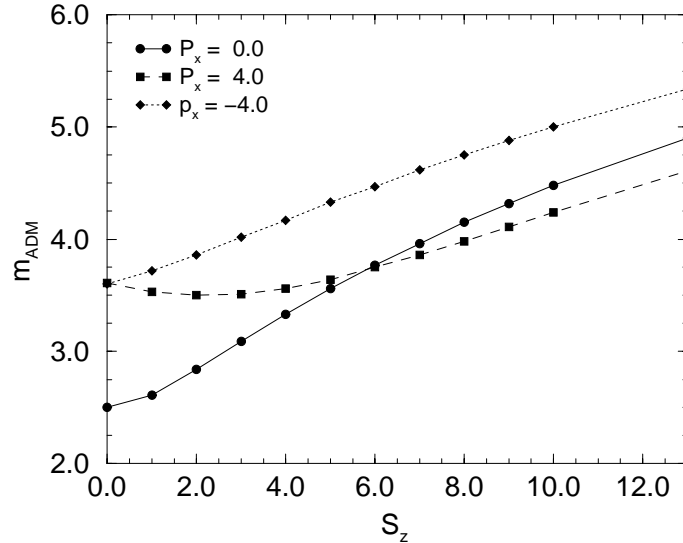
Figure 6.17: Mass m_{ADM} of the binary black hole system for different spins on the holes and two different linear momenta.

$M_1 = 1.5$ of the upper black hole. To examine systems in dependence on the intrinsic spins the same spin vector **S** is applied on both holes.

The first case examined is a system with vanishing intrinsic linear momentum. If the spin vanishes too, the extracted mass is $m_{ADM} = 2.5$ which is just the sum of the single black hole masses as is expected for this Brill-Lindquist type data set. For finite spin the mass increases non-linearly with the spin. The decreasing slope of the dependence for higher spins should again be due to errors caused by the very limited size of the computational domain, as was discussed in section 6.3.2. Thus the behavior of the extracted mass in dependence on the spin is analogous to that in dependence on intrinsic linear momentum.

The other two systems examined in figure 6.17 are data sets with $P_x = 4$ and $P_x = -4$. Analytically the total angular momentum just due to the linear momentum is $J_z = -12$ and $J_z = 12$, respectively. This can also be extracted from the numerical data, as is shown in figure 6.18. For vanishing spin both systems exhibit an equal mass of $m_{ADM} = 3.61$. For increasing spin the extracted mass of the system with $P_x = -4$ increases almost linearly up to about $S_z = 7.5$ where the slope decreases again due to the limited size of the computational domain. In contrast to this the extracted mass for the $P_x = 4$ system exhibits a decrease of about 4 percent up to a spin of $S_z = 3$. For higher spins the mass increases and shows a behavior which is parallel to the mass of $P_x = -4$ system in figure 6.17.

This deviating mass dependence for the data sets with momentum is caused by the fact that the spin adds to the angular momentum due to the intrinsic linear momenta of the holes for the system with $P_x = -4$. As is visible in figure 6.18 the total angular momentum is $J_z \approx 12$ for $S_z = 0$ in this system. For finite spin the total angular momentum further increases with the spin. In contrast to this the spin subtracts from the angular momentum due to the intrinsic linear momenta for $P_x = 4$. Thus, the total angular momentum of $J_z \approx -12$ for vanishing spin decreases in its absolute value up to the point where the spin parameter reaches $S_z = 6$. Here the angular momentum vanishes. Since the spin is applied on each hole the angular momentum of the system due to the spins is $J_{(spin)} = +12$ for $S_z = 6$ which leads
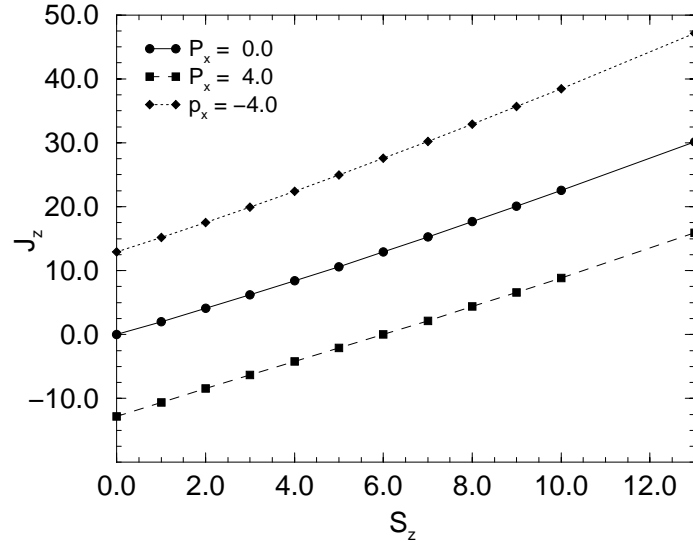
Figure 6.18: Total angular momentum of the binary black hole system for different black hole spins and two linear momenta.

to the vanishing total angular momentum as shown in figure 6.18. For higher spin the total angular momentum increases further as now the angular momentum due to the spin exceeds the angular momentum due to the linear momentum.

The effect of the diminishing amount of angular momentum in the system is reflected in the decrease of the extracted ADM mass. But, due to non-linear effects, the minimum of the mass does not coincide with the minimal amount of angular momentum.

6.3.5 High Angular Momentum

The tests up to now showed that the extraction of ADM mass and angular momentum is possible to within a few percent up to spins and linear momenta of about a value of 10. I will now consider the case of a binary black hole system with very high intrinsic linear momentum on the holes and hence a very large total angular momentum. Here the question is how well the extraction works for such high momentum.

In figure 6.19 and 6.20 the extracted mass M_{ADM} and total angular momentum J_z are shown in dependence on the intrinsic momentum, respectively. There are two extractions with different grid sizes and different minimal extraction radii for a constant grid spacing of $h = 0.75$ where static boundary conditions have been applied. Further there is one extraction for initial data computed with Robin boundary conditions.

According to figure 6.19 the mass extraction exhibits an almost linear dependence up to about $P_x = 10$. However, even in this regime the mass of the data sets computed with static conditions show deviations by a slower than linear increase. For higher momentum the increase slows down further and finally turns into a decrease of the extracted mass. As is obvious from the diagram this is caused by the limited size of the computational domain since the growth in the extracted mass keeps on longer for the larger grid and larger minimal extraction radius than for the smaller grid. For initial data computed with Robin boundary

conditions the extracted mass is increasing up to the highest linear momentum tested which is $P_x = 200$. But also in this case the slope in dependence on momentum decreases.

Thus the mass extraction from initial data computed with Robin conditions looks much more reasonable than that for static conditions, since at least the mass decrease can not be physical. However, there are no analytical mass values available for comparison. Thus, a final decision up to which momentum the mass extraction reproduces the right result is not possible here.

In contrast to this the theoretical value of the total angular momentum for the binary black hole system is known. It is given by equation 6.9 and shown in figure 6.20. For $P_x < 10$ the extraction of the total angular momentum is right for initial data computed with either static or Robin boundary conditions. For initial data computed with static boundary conditions the extracted angular momentum for higher linear momentum shows deviations from the theoretical behavior by being to large in amount. This is even more striking for the extraction with small minimal extraction radius. For $P_x = 200$ the deviation is about 81 percent for the larger grid and extraction radius and about 117 percent for the smaller grid.

The extraction error is much smaller for initial data computed with Robin boundary conditions. Further, in contrast to the static boundaries, the extracted total angular momentum is of smaller amount than the theoretical value. For $P_x = 50$ the absolute value of the extracted angular momentum is about 8 percent to small. For comparison the extracted angular momentum is already 60 percent too big at this point when static conditions are used. Up to a linear momentum of $P_x = 200$ the deviation increases to 38 percent, which is again much smaller than for static boundary conditions.

To conclude, for initial data computed with Robin boundary conditions, it is possible to extract the spin with an accuracy of about 10 percent if the value of linear momentum on the black holes (P_x) equals the location r_{bound} of the boundary. For initial data computed with static boundary conditions the error is about 5 times bigger. Thus, the size of the grid imposes limits to the parameters settings which allow an accurate simulation of the black hole system. This is independent of the size of the apparent horizons, which are usually small compared to the extension of the grid as will be discussed below.
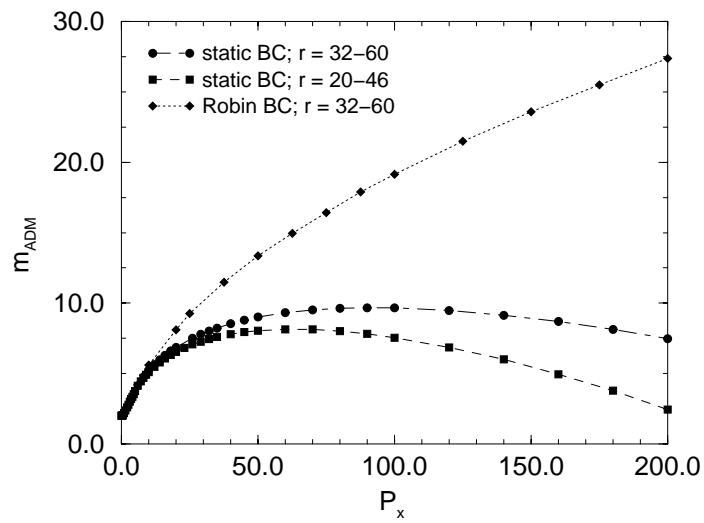
Figure 6.19: Extracted ADM mass of the binary black hole system for high angular momentum J_z due to high linear momenta P_x.
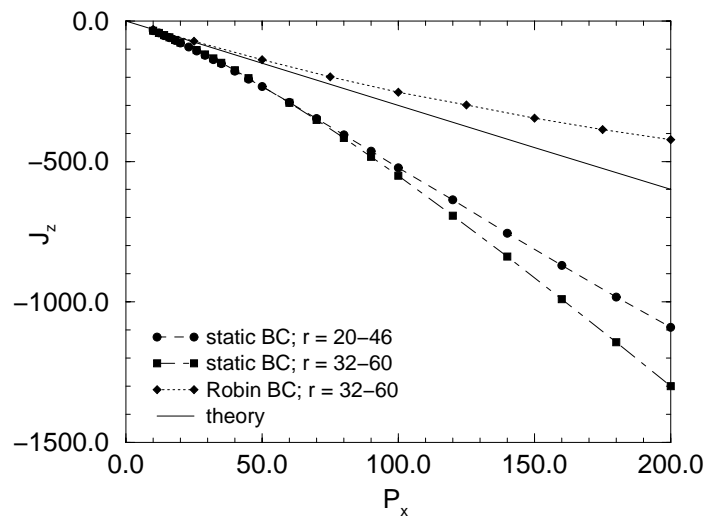

Figure 6.20: Total angular momentum J_z of the binary black hole system for systems with high angular momentum due to high linear momenta.

6.4   Apparent Horizons

In the last section I discussed several configurations of puncture initial data in order to study the parameter space for data sets representing binary black hole systems. In this discussion I focused on the extraction of the ADM mass and the linear and angular momentum. These examinations allowed for the discussion of several effects appearing in the initial data.

In this section I will focus on apparent horizons. As the finder algorithm for apparent horizons in three dimensions is very time consuming I will restrict the examination even more to some particular data sets.

6.4.1   Convergence for Numerically Created Initial Data

In section 5.2.3 I studied the convergence of the surface which was found by the apparent horizon finder algorithm presented in section 5.2.1. For the analytical Brill-Lindquist data studied, the shape of the found apparent horizon converged to about second order.

In figure 6.21 the shape of the apparent horizon for numerically generated puncture initial data is shown in the three coordinate planes. This data set exhibits equal masses ($m_{1,2} = 1.0$) for the punctures located at $\mathbf{c}_{(1,2)} = (\pm 0.4, 0, 0)$. The intrinsic momenta are $\mathbf{P}_{(1,2)} = (0, \pm 0.8, 0)$ and $\mathbf{S}_{(1,2)} = (\pm 0.8, 0, 0)$. This data set is currently under examination as a close limit case studied with perturbation theory [48].

Like in the case with analytical initial data the shape of the found surface is converging to some surface, too. Considering the area of the horizon and the expansion coefficients shown in figure 6.22 the convergence of the surface is clear. Despite this, the convergence exponents show the dependence on the numerical solution for the conformal factor. In contrast to the Brill-Lindquist case studied in section 5.2.3 with convergence exponents for the expansion coefficients between 1.7 and 2.3, the convergence exponents here lie in a wider range, as shown in figure 6.22. There are even cases like the coefficient a_{30} which does not show a defined convergence at the considered resolutions. These effects are due to the fact that the numerical solution for the conformal factor itself converges to second order as was shown in section 6.1. Thus the numerical horizon finder algorithm is acting on the numerical generated solution for the metric which can lead to deviations in the solution of the horizon finder.

6.4.2   Apparent Horizons for Varying Mass Ratios

In figure 6.23 the location of the surfaces found by the apparent horizon finder algorithm are shown in the x-y plane for different mass ratios and three different linear momenta p. This binary black hole data is analog to the systems examined in section 6.3.3 with vanishing spin and the punctures located at $\mathbf{c}_{(1,2)} = (0, \pm 1.5, 0)$. Again the upper black hole possesses a linear momentum of $P_x = +p$ and the lower by has a linear momentum of $P_x = -p$.

For $p = 0$ the horizon finder algorithm locates separated marginally trapped surfaces for all mass ratios probed. However, only for the smaller mass ratios these surfaces really represent apparent horizons. In the interval $M_1 \in [3.2, 3.4]$ the transition from separated horizons to a single common horizon occurs. The location of the surface at these masses is shown in figure 6.23. For $M_1 = 3.2$ the surface found by the algorithm seems already to be the right one, but since the mean square of the expansion is not small enough, the horizon finder does not output this surface as an apparent horizon.
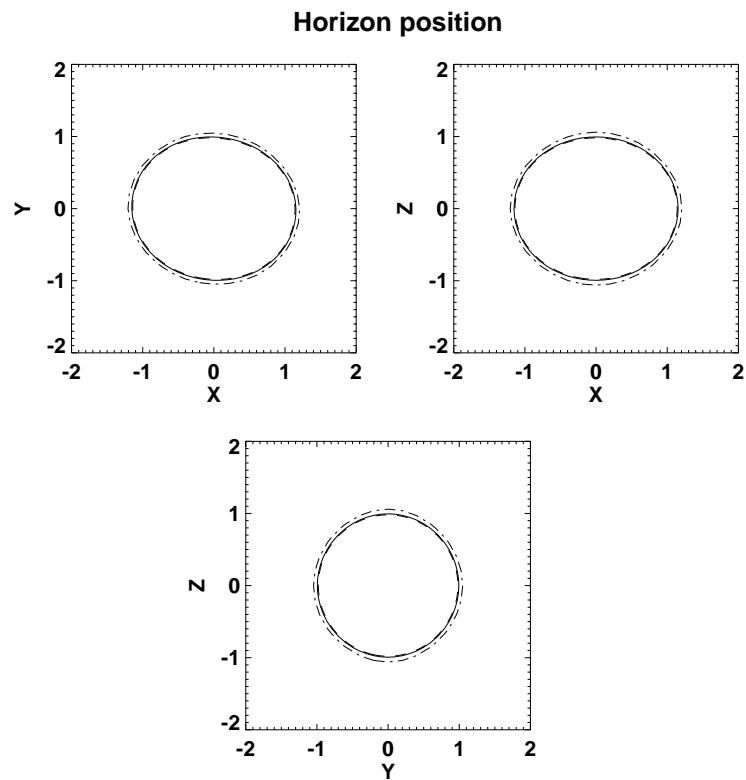
Horizon position

Figure 6.21: Location of the apparent horizon in the three coordinate planes along the axes for the close limit case. The resolution is from the outer side inwards $h = 0.05, 0.1, 0.2$.
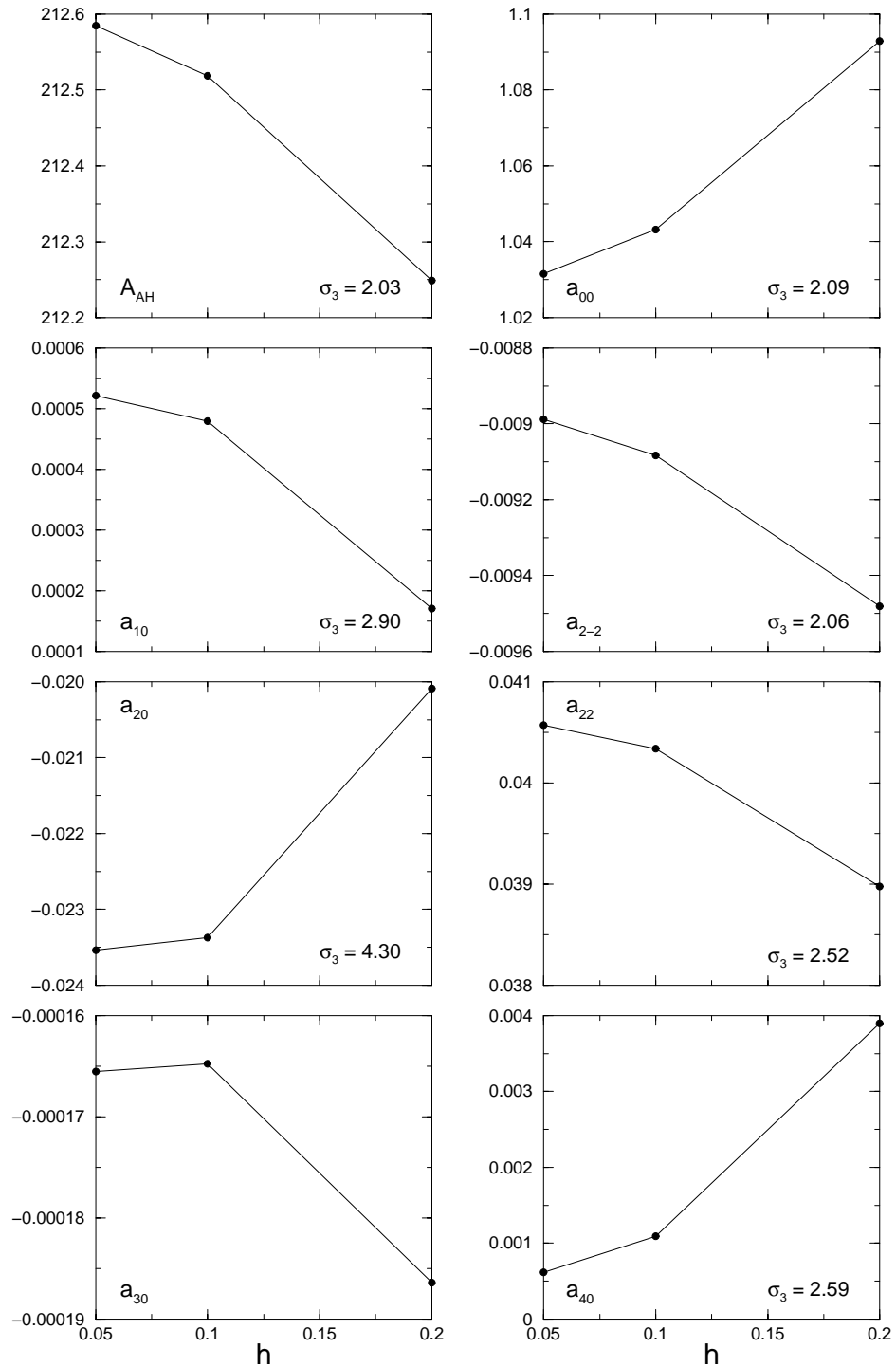
Figure 6.22: Area and major expansion coefficients of the found apparent horizon for the close limit case in dependence on the resolution. Also shown are the three-level convergence exponents.
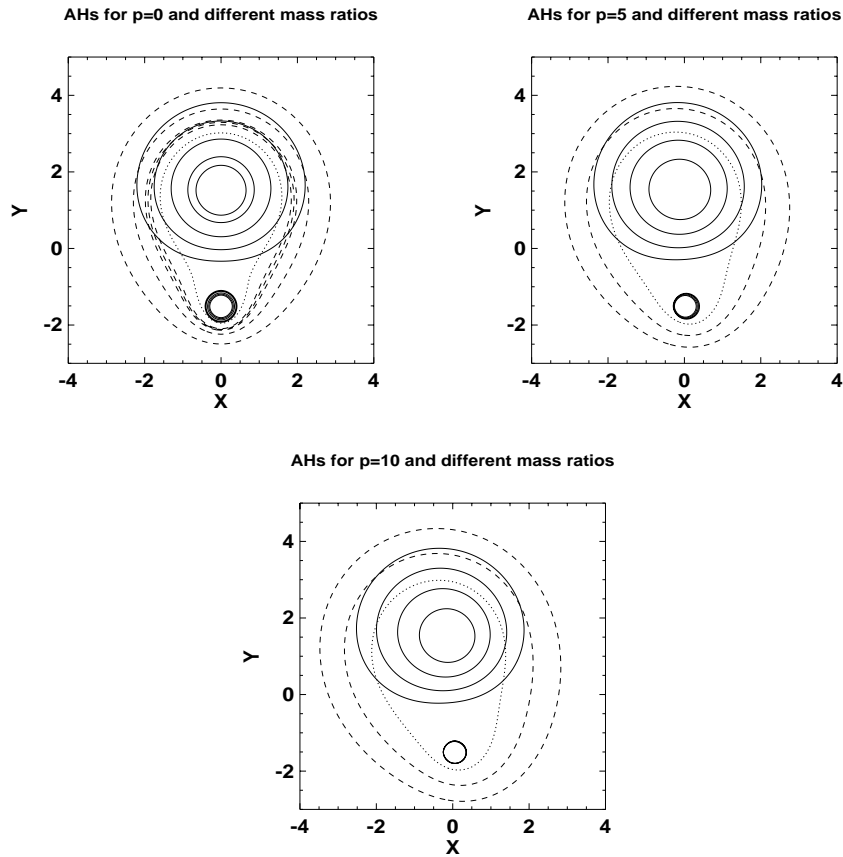
AHs for p=0 and different mass ratios

AHs for p=5 and different mass ratios

AHs for p=10 and different mass ratios

Figure 6.23: Location of the apparent horizons in the xy-plane for different mass ratios and three different momenta. The solid lines show the separated trapped surfaces while the dashed lines show the location of the common horizon. The dotted line is a surface where the horizon finder algorithm stopped without finding a horizon. For the data sets with $p = 5$ and $p = 10$ the separated surfaces are shown for the masses $M_1 = 5, 4, 3, 2$ (Beginning from the outermost one.) The common surface is shown for $M_1 = 5, 4, 3$. For $p = 0$ the separated surfaces correspond from the outermost surface inwards to $M_1 = 5, 4, 3, 2, 1.5$ and the common horizons to $m_1 = 5, 4, 3.4, 3.3, 3.2, 2$.

But for $M_1 = 3.3$ also the mean square of the expansion vanishes. Hence for $M_1 \geq 3.3$ the common horizon exists. According to the definition of apparent horizons as the outermost marginally trapped surface the common surface is now the apparent horizons. The separated horizons are then simply marginally trapped surfaces but no apparent horizons.

For $p = 5$ and $p = 10$ the horizon search has been performed with larger mass intervals. However, for $M_1 = 4$ an apparent horizon is found while none is found for $M_1 = 3$ in both cases.

It is also obvious from figure 6.23 that the area of the found surfaces increases with the mass ratio. This can be quantified in terms of the apparent horizon mass m_{AH}. This quantity has been defined in equation 5.20. Since here each of the separated horizons does just correspond to a black hole with finite linear but vanishing angular momentum the horizon
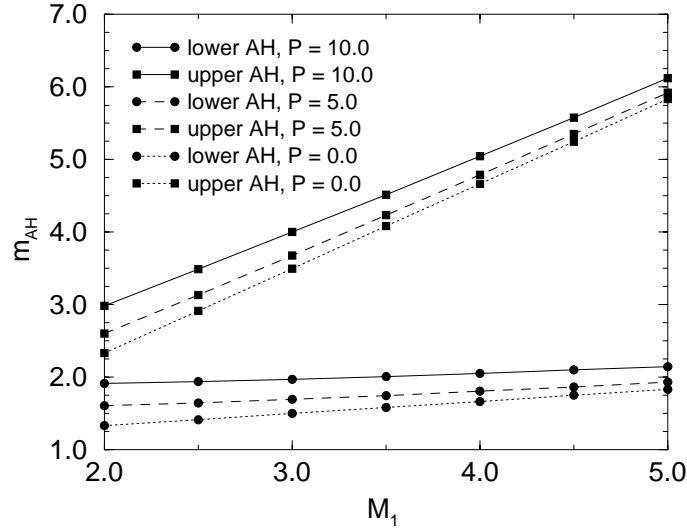
Figure 6.24: Mass of the separated apparent horizons in dependence on the mass M_1 and different momenta P.

mass is simply given by the irreducible mass m_{ir}. Hence the horizon mass is here

$$m_{AH} = m_{ir} = \sqrt{\frac{A_{AH}}{16\pi}} \; . \tag{6.11}$$

In figure 6.24 the horizon masses of the separated horizons are shown for the three momentum studies shown in figure 6.23. It is obvious that, despite the fact that only the mass of the upper black hole is increased, the mass of both apparent horizons increases. This shows the correlation between both black holes and is also true for Brill-Lindquist data ($P = 0$). The masses increase linearly with the momentum for both horizons.

For the Brill-Lindquist type data it is also visible that the sum of the horizon masses is bigger than the ADM mass of the initial data which is just the sum of the mass parameters. This effect can be explained analytically: According to Brill and Lindquist [23] the mass m_{BL} of an apparent horizon ("bare mass" in the notation of Brill and Lindquist) in binary Brill-Lindquist data is given by

$$m_{BL(i)} = M_i + \frac{M_1 M_2}{2d} \tag{6.12}$$

where i is the black hole index. Using this relation we can exactly reproduce the masses m_{AH} found numerically by the horizon finder algorithm 6.24. The difference between the sum of the horizon masses and the mass of the entire black hole system

$$m_{int} = \sum_i m_{BL(i)} - m_{ADM} \tag{6.13}$$

is the so called 'interaction energy' m_{int}. It is negative due to the "attractive forces" [23] between the black holes. The amount of interaction energy increases with the mass M_1 as is shown in figure 6.28 below.

For initial data with finite momentum this analytical study is not possible. However it is at least possible to study the interaction energy. I will do this in the next sections to study the interaction energy in dependence on the momentum and spin of the black holes.

Another feature, which can be deduced from figure 6.23, is the shape and location of the horizons in dependence on the momentum. For higher momentum the upper horizon is displaced in the direction of negative values of x and the lower horizon to positive values. Hence, the horizons trail the coordinate dependent "motion" of the black hole system, as was discussed by Alcubierre [5]. For an event horizon one would expect the shift in the opposite direction, i.e. in the direction of the momentum, since avoiding to fall into a black hole should be harder if the hole is moving towards the observer. The displacement of the apparent horizons is motivated by mathematical arguments considering equation 5.10. Mainly the term $K_{ij}s^i s^j$ which is odd under reversal of P^i and n^i causes the displacement. Also the common apparent horizon which exists for a higher mass M_1 is rotated in this way.

6.4.3 Separated Horizons for Finite Momentum and Spin

In sections 6.3.2 and 6.3.4 I studied the dependence on a binary black hole system on the intrinsic linear momentum and on the spin of the black holes in respect to the extraction of mass and total angular momentum. I will now examine apparent horizons of such systems.

In figure 6.25 the location of the apparent horizons in dependence on intrinsic momentum and vanishing spin for the data set with $d = 3$ is displayed. As in the last section, the displacement of the horizons with increasing momentum is visible. Again it is oriented contrary to the momentum vectors and grows with the momentum.

Further, the horizon shrinks in the coordinates used for computation. Despite this the horizon area which is computed from the 2-metric on the surface increases as is displayed in terms of the horizon mass in figure 6.27. Since the horizons shrink in the computational coordinates while the coordinate location remains fixed the proper distance of the horizons increases.

However, the shrinkage of the horizon in the computational coordinates is mostly due to the increasing extrinsic curvature, cf. equation 5.10, which is a property of the slice on which the horizon is calculated. Thus, a statement if the proper separation between the black holes, i.e. the physical distance of the black holes, increases with the intrinsic momentum is not possible based on the apparent horizon study. Such a statement is only possible based on the event horizon as this encloses the apparent horizon.

The location of the apparent horizons for varying spin on the holes and vanishing linear momentum is shown in figure 6.26. The data sets are analogous to the systems with $P_x = 0$ and $d = 3$ examined in section 6.3.4. Here, the surface shrinks in the computational coordinate system for increasing spin but the horizon remains centered around the puncture. However, the area of the horizons is again increasing with the spin. In figure 6.27 the corresponding horizon mass m_{AH} is shown. Since the holes possess finite spin the horizon mass is given by equation 5.20 which involves the spin **S** of the black hole.

The behavior of the horizon mass when either the intrinsic linear momentum or the spin is changed is non-linear with a transition to a linear dependence for higher values of spin or momentum. Thus, this dependence is analogous to that of the ADM mass on momentum and spin, as was depicted in sections 6.3.2 and 6.3.4. The growth in the mass is bigger in

dependence on the spin than on the linear momentum. This is partly due to the spin term in equation 5.20 which gives no contribution for the purely linear momentum case. However, the irreducible mass m_{ir} increases faster for the spin case, too.

In figure 6.28 the interaction energy m_{int}, as defined by equation 6.13, rescaled by the ADM mass is displayed for data sets with different mass ratio, with different intrinsic linear momentum, and with different spin. For vanishing spin and momentum on the holes the total amount of interaction energy m_{int} increases linearly with the mass ratio of the black holes. Normalized by the ADM mass this dependence is non-linear. Considering equations 6.13 and 6.12 for the interaction energy and the mass m_{BL} together with equation 6.10 for m_{ADM} it is obvious that m_{int}/m_{ADM} will approach $-1/3$ in the limit of a high mass ratio $M_1/M_2 \gg 1$ for a puncture separation of $d = 3$. This is consistent with the computed interaction energy but the numerical extraction has not reached this limit. As was discussed in section 6.4.2 the ADM mass and the horizon mass m_{AH} for the system with vanishing spin and momentum are fully consistent with the calculations by Brill and Lindquist [23]. Hence also the computed interaction energy must be right.

If only the spin is finite the total amount of interaction energy rescaled by m_{ADM} decreases with growing spin from its analytical value of -2/9 to about -3.9 at $S_y = 4$. For larger spin the normalized interaction energy remains almost constant with a small increase for spin bigger than $S_y = 6$. This should be due to numerical errors. Thus, in dependence on the spin an asymptotic value for the normalized interaction energy is reached much faster than in dependence on the mass ratio.

Depending on the linear momentum P_x the behavior of the normalized interaction energy is quite different. Starting, of course, from the analytical value of $m_{int}/m_{ADM} = -2/9$ for $P_x = 0$ the total amount of interaction energy diminishes up to a momentum of about $P_x = 5$ where it amounts to zero. For higher linear momentum the rescaled interaction energy increases to positive values. From a classical Newtonian viewpoint, this would mean that the attraction of the black holes diminishes leading finally to a non-attractive system, i.e. to a system of two black holes which will not merge in the course of an evolution.

However, the size of the errors in the numerical extraction and in the found horizons is not obvious. The extraction of ADM mass is correct up to errors of about one percent as was discussed in previous sections. Since in the convergence studies of the apparent horizon finder algorithm the surface area was strongly converging, the expected error is here below one percent, too. But since the horizons are smaller here and their size is still diminishing for increasing momentum the error might be bigger.

Nonetheless, a final statement if the positive interaction energy points to a binary black hole system with non-merging holes, can only be deduced from long time evolutions of such initial data sets. If a common apparent horizon emerges during the evolution of the black holes they are definitely merging. Also it is possible that an event horizon enclosing both punctures exists already in the initial data. Then the initial data would in fact represent a single black hole.

Physically it is at least possible that a data set with higher linear momenta on the black holes represents a system of two black holes which are not merging in the course of the evolution. Since with increasing intrinsic linear momentum the proper distance of the apparent horizons grows and the momentum of the holes increases, there will be a limiting point above which the two holes will pass each other and do not merge to a single black hole in the course of the evolution.
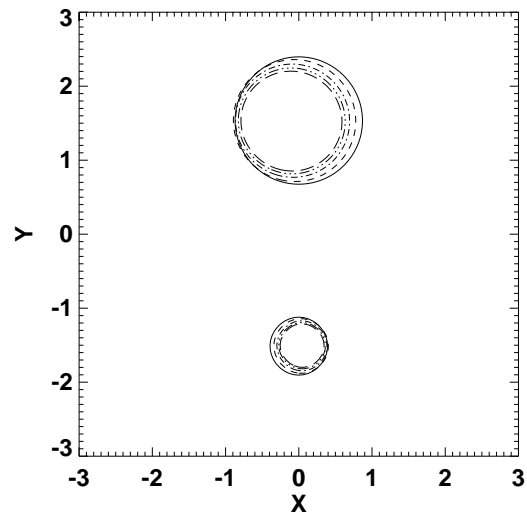
Figure 6.25: Location of the apparent horizons in the xy-plane for initial data representing a binary black hole system with intrinsic linear momentum $P_x = 0, 1, 3, 5, 7$, and 9 and vanishing spin on the black holes. For increasing linear momentum the surface shrinks in the computational coordinates and shifts in x-direction.
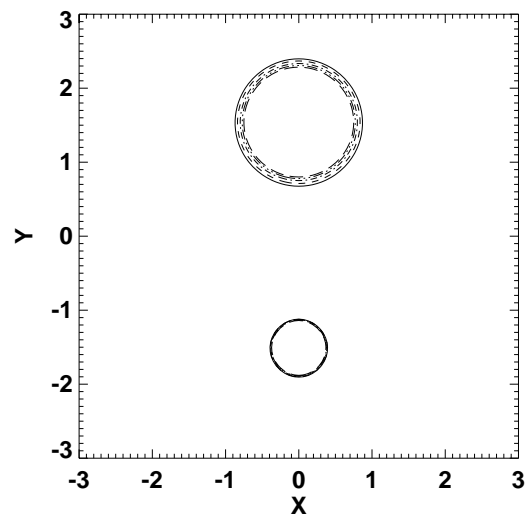

Figure 6.26: Location of the apparent horizons in the xy-plane for the binary black hole system with black hole spins $S_z = 0, 1, 3, 5, 7$, and 9. Since the linear momentum vanishes the center of the surfaces is fixed. For increasing spin the horizon shrinks in the coordinates used for computation.
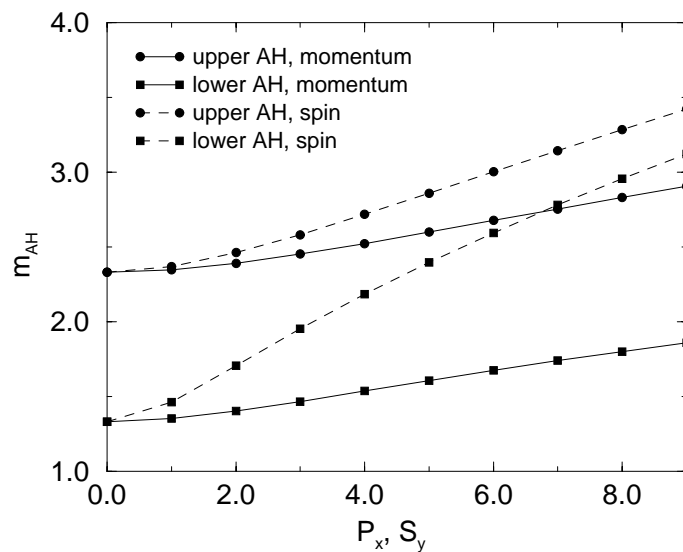
Figure 6.27: Apparent horizon mass m_{AH} of the separated horizons in dependence on the intrinsic black hole momentum and the black hole spin.
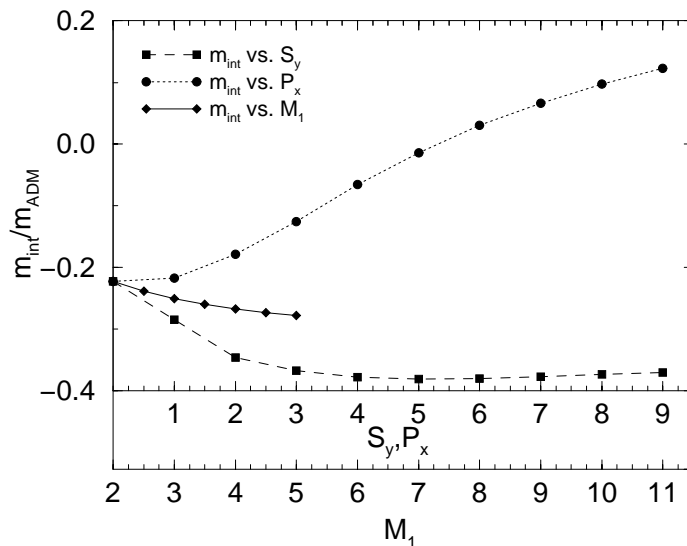

Figure 6.28: Interaction energy for binary black hole systems. Shown is the dependence on the interaction energy on the mass ratio of the holes, the momentum and the spin of the holes.

Chapter 7

Evolution of Puncture Initial Data

According to the initial data study performed in the last chapter puncture initial data provides data sets representing slices with multiple black holes of arbitrary mass, linear momentum, and spin. As was shown in chapter 6 physical quantities like the ADM mass, the linear momentum and the angular momentum can be extracted with high accuracy. Also apparent horizons, enclosing either single punctures or multiple punctures, can be computed and studied with geometrically quantities like the horizon mass.

In this chapter I will examine the evolution of such initial data sets. I will focus on one particular data set representing a binary black hole system with unequal masses, spin, and linear momentum on the holes. During the evolution these black holes will undergo a grazing collision and merge to a single hole. In the course of this process they will emit gravitational waves which can be calculated using the methods described in section 5.3. In addition, the motion of apparent horizons can be studied, showing that the black holes, as defined by their horizons, are in fact moving with respect to the computational grid.

The data set examined in the next sections is defined by the following parameters: masses $M_1 = 1.5, M_2 = 1.0$; location $\mathbf{c}_{(1,2)} = (0, \pm 2, 0)$; momenta $\mathbf{P} = (\pm 1.5, 0, 0)$; spins $\mathbf{S}_1 = (0.5, 0, 0.5), \mathbf{S}_2 = (0, -1.0, 1.0)$. The orientation of the spin and momentum vector is sketched in the neighboring figure.

This system is the analog to the data set examined by Brügmann [26] with just the system rotated to be oriented along the y-axis of the computational grid. Due to the choice of different masses and spins the system does not show symmetries any more, it is a full 3D data set. Hence, it must be evolved on a full three-dimensional grid with its large computational requirements.
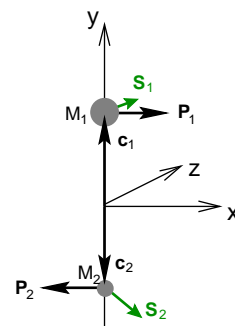
The ADM mass for this system can be extracted to be $m_{ADM} = 2.97$ and the angular momentum is $\mathbf{J} = (0.5, -1.0, -4.5), |J| = 4.637$. If only a negligible fraction of the angular momentum will be radiated away by gravitational waves, the final black hole will correspond to a Kerr black hole [42] with rotation parameter $a/m = J/m_{ADM}^2 = 0.526$. A review on Kerr black holes can be found in the textbook by Wald [52].

7.1   Numerical Aspects of the Evolutions

The evolutions here are performed applying the conformal ADM evolution system (*BSSN* system). Furthermore the 1+log-slicing is used during the evolution while for the calculation of the initial lapse function maximal slicing condition is used to obtain a good form of the lapse. The shift vector β^i is chosen to vanish.

Since the metric diverges at the punctures the implementation of the evolution algorithms in *Cactus* does not rely on the metric γ_{ij} but rather on the rescaled metric γ_{ij}/ϕ^4 with ϕ defined by equation 3.30

$$\phi = 1 + \sum_{i=1}^{N} \frac{M_i}{2r_i}$$

with summation over $N = 2$ black holes i with mass M_i. Here '1' is used instead of u so that derivatives of ϕ, which have to be computed for the calculation of derivatives of the unscaled metric γ_{ij}, can be computed analytically. Since *Cactus* uses the rescaled metric, all metric functions shown in diagrams in this work are displayed in the rescaled form. In addition to this the rescaled metric is also used in the equations of the *BSSN* formalism which involve the metric.

For the initial solution of the maximal slicing condition, equation 4.15,

$$\Delta \alpha = \alpha K_{ab} K^{ab},$$

the question arises, whether it is well defined near the punctures. Considering the analytical form of the extrinsic curvature as given by equation 3.21 and the conformal flat character of the metric $(\gamma^{ij} = \psi^{-4}\delta^{ij})$ it is obvious that the principle part of $\Delta \alpha$ is $O(r^4)$. Further, terms involving first order derivatives of α are $O(r^3)$ and the right hand side of the maximal slicing condition is $O(r^6)$ when spin is present, otherwise $O(r^8)$. According to this the first derivatives of α have to vanish at the punctures. This is fulfilled if equation 4.15 is multiplied by ϕ^4 [26].

Brügmann [26] also showed that with the rescaling of metric and extrinsic curvature a stable evolution with the classical ADM formalism is obtained in the sense that the character of the singularities at the punctures does not change and no additional singularities arise. The time derivatives of the metric and extrinsic curvature rescaled by the conformal factor ψ vanish at the punctures.

The evolutions here are performed with the *BSSN* evolution formalism which evolves different variables than the classical ADM formalism. However in *Cactus* this formalism utilizes the rescaled metric γ_{ij}/ϕ^4 which vanishes at the punctures. In addition to this $tr K = 0$ is chosen initially. Thus, the time derivatives of the *BSSN* variables (λ, K, $\tilde{\gamma}_{ij}$, $\tilde{A}_{ij}$, and $\tilde{\Gamma}^i$) vanish at the punctures. Thus the initial data can be evolved using the *BSSN* formalism even with grid points located at the punctures.

When a configuration with grid points at the punctures is used together with 1+log slicing, the lapse function α does not collapse at the punctures. Thus, the slicing will not be completely singularity avoiding. Evolutions with this slicing showed that for late evolution time the lapse in the whole domain around the punctures has collapsed to zero except at the two grid points where the punctures are located. This results in sharp peaks in the metric

functions around the punctures and finally in the crash of the simulation. To avoid this effect I changed the implementation for the lapse function. When grid points are located at the punctures the lapse at these points is now computed as the average of the lapse at the six neighboring grid points. Since the lapse function is a pure gauge quantity this approach is valid.

7.2 Results of the Evolutions

The binary black hole system described above has been evolved on different grids. With very large grids of 387^3 grid points the evolution was possible up to $t \approx 120$ using grid spacings of $h = 0.25$ and $h = 0.1875$. The memory requirements for such simulations amounted to about 110 gigabytes and the computation time was between 24 and 40 hours on a 256 processor SGI Origin 200 parallel computer.

At the evolution time of $t = 120$ larger errors, mostly visible in the wave modes, developed. The simulations have been stopped at this time without crashing. Smaller grids with either smaller grid spacing or with lesser grid points lead to an earlier development of errors or even to the crash of the simulations at earlier evolution time.

However, the evolution times possible with the current implementations of evolution algorithms in *Cactus* are much longer as that of the simulations done in [26]. These crashed at about $t = 20$. Now, when applying very large grids and the *BSSN* evolution formalism, the evolution of apparent horizons can be studied for longer time and even the extraction of gravitational waves is possible.

7.2.1 Time Development of Metric and Lapse

In figures 7.1 and 7.3 the time development of the rescaled metric component γ_{yy}/ϕ^4 and the lapse function α are shown, respectively. The time is rescaled by the mass $M \equiv m_{ADM}$. These diagrams show the basic features of the evolution of a binary black hole system with merging holes.

The metric grows in time and the lapse function collapses to zero. For earlier time the growth of the metric is located between and next to the punctures since at this time two separated black holes exist. The value of the lapse function collapses near the holes. With elapsing time the black holes merge forming a single black hole. Since the lapse is collapsed to zero between the holes the metric freezes in this region. After the single hole has formed, the metric increases exterior to the grow region of the separated holes. This leads to the shoulders on the inner sides of the metric function γ_{zz}/ϕ^4. The region in which the lapse function collapses is expanding in the course of time since despite of the singularity avoiding slicing grid points are falling into the black hole. Due to the radiative boundary conditions used in the simulation, the lapse function also decreases and the metric grows slowly at the boundary.

7.2.2 Evolution of Apparent Horizons

Since black holes are defined by the existence of an horizon one can study the motion of a black hole by the time evolution of the apparent horizon. As was pointed out by Brandt and Brügmann [20], the punctures describing the the internal, asymptotically flat region of
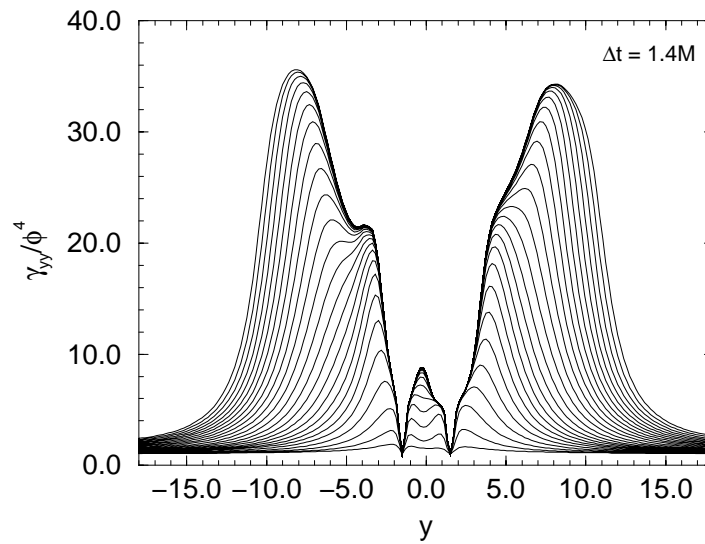
Figure 7.1: Time development of the rescaled metric component γ_{yy}/ϕ^4 for the binary black hole system. The metric is growing during the evolution but freezing in the center region of the grid at later time.
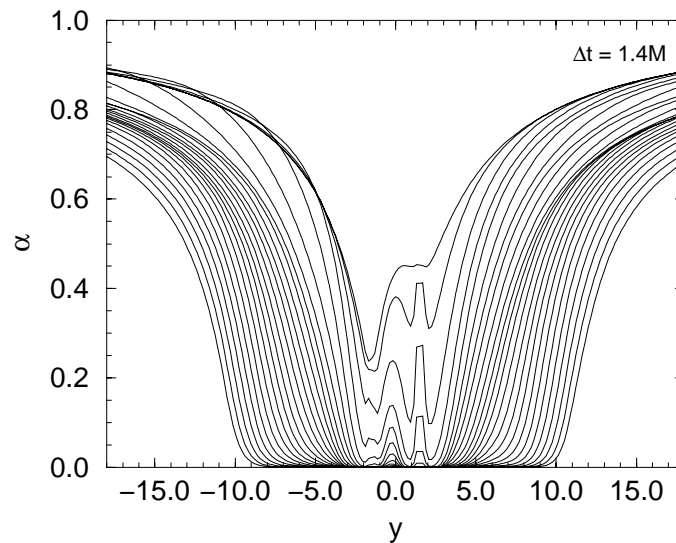

Figure 7.2: Time development of the lapse function α in the evolution of the binary black hole system. At first the lapse is collapsing in the neighborhood of the punctures. Then the collapsing region grows and the lapse value at the boundary is diminishing, too.
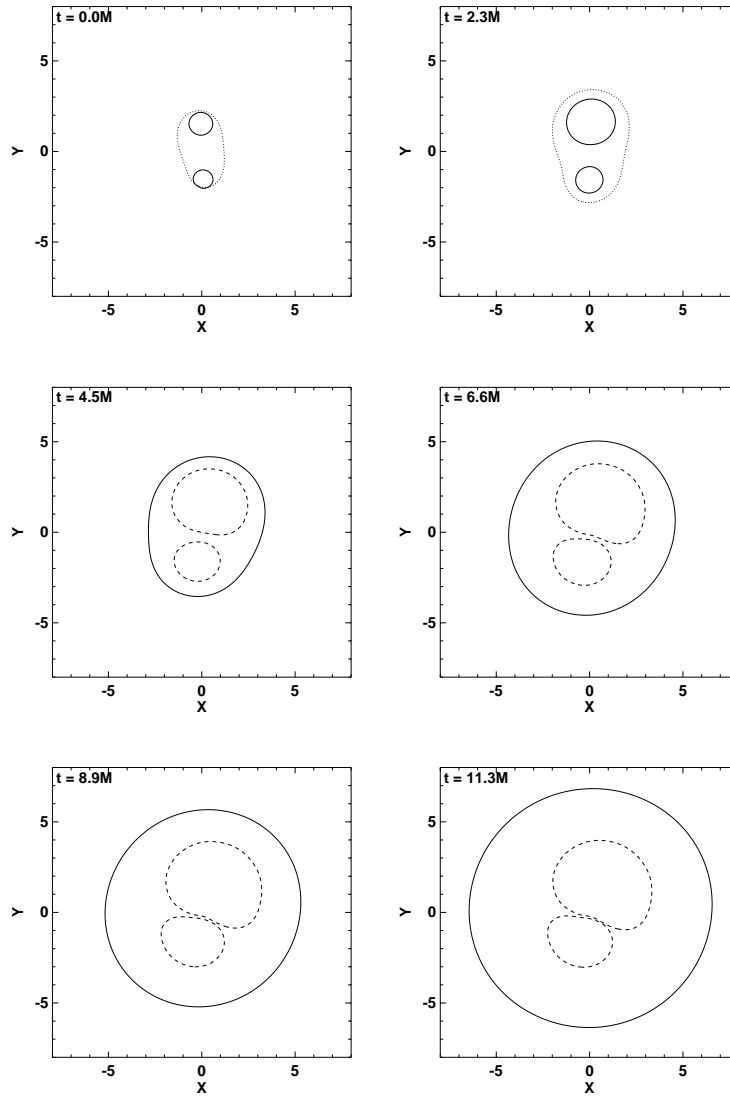
Figure 7.3: Evolution of the apparent horizon. Dotted lines depict surfaces where the horizon finder algorithm stopped without finding a horizon, while solid lines represent found horizons and dashed lines represent marginally trapped surfaces which are no apparent horizons.

the black holes are, by construction, fixed on the grid. Hence, it is not possible to simulate multiple orbits of the black holes in binary systems with puncture initial data. The data gives the possibility to simulate the late state of an inspiraling system, just before the two black holes merge. But this data is still a generalization to the time symmetric Misner or Brill-Lindquist data sets since it permits non time-symmetric data sets with momentum and spin on the black holes.

For the punctures being fixed on the grid, the dynamics of the system is contained in the metric. This can be shown, for example, by the apparent horizons as is done in figure 7.3. In the initial time slice two separated horizons exist oriented along the y-axis. The dotted line shows the surface at which the horizon finder algorithm stopped without finding a common apparent horizon.

Until $t = 2.3M$ the separated horizons grew. Also a very small rotation of the horizons around the z-axis is visible. At $t = 4.5M$ the common horizon has emerged. Tests with finer resolution in time show that the common horizon develops at $t \approx 3.4$.

The separated horizons do not transform continuously to the common horizon. Rather there occurs a discontinuous process in which at some time the conditions for an apparent horizon enclosing the marginally trapped surfaces around the single black holes are fulfilled.

After the common horizon appeared the inner surfaces found by the horizon finder algorithm are enclosed by the apparent horizon The horizon finder algorithm does still find these surfaces as marginally trapped surfaces but for a time of $t > 5$ the mean expansion on this surfaces does not vanish. This is due to the limited number of terms in the expansion which is given by $l_{max} = 8$ here. Hence the dashed lines at $t = 6.6M, 8.9M$, and $11.3M$ show the location of the surface found by the algorithm but not necessarily the right marginally trapped surfaces. At least when the two single surfaces touch each other there will be another minimal surface enclosing these two surfaces. However, also the single surfaces found by the horizon finder algorithm show the rotation of the binary black hole system. In visualizations of gravitational waves [41], a larger rotation of the system is visible. Up to $t = 80$ a rotation of about 180 degrees is visible for a similar initial data set.

Just after emerging the common apparent horizon is strongly deformed from a spherical shape. However, with increasing time the shape of the horizon becomes more and more spherical. Due to the infalling grid points grid horizon grows in the computational coordinates.

7.2.3 Gravitational Waves

As the evolution time allow for the extraction of gravitational wave modes I finally present results of the extraction of gravitational waves from the evolutions.

In figure 7.4 the even-parity wave mode ψ_{20}^e is shown extracted from evolutions on grids with three different resolutions and a fixed location of the boundary. The simulation on the coarsest grid (99^3 grid points with boundary at $r_{bound} = 18$ and grid spacing $h = 0.375$) was only possible up to $t = 90 \approx 30M$. It is obvious that for $t > 17M$ the wave form deviates clearly from the waveforms extracted from finer grids.

Also this is obvious from the calculation of the convergence exponent as shown in the lower part of figure 7.4. For $t < 10M$ second order convergence is visible. The convergence is undefined for $t < 1M$ since the initial data has been computed with Robin boundary conditions showing no defined convergence in the outer region of the grid, as was discussed in section 6.1.2. The sharp peaks at $t \approx 8M$ are due to a crossing of the wave amplitudes.
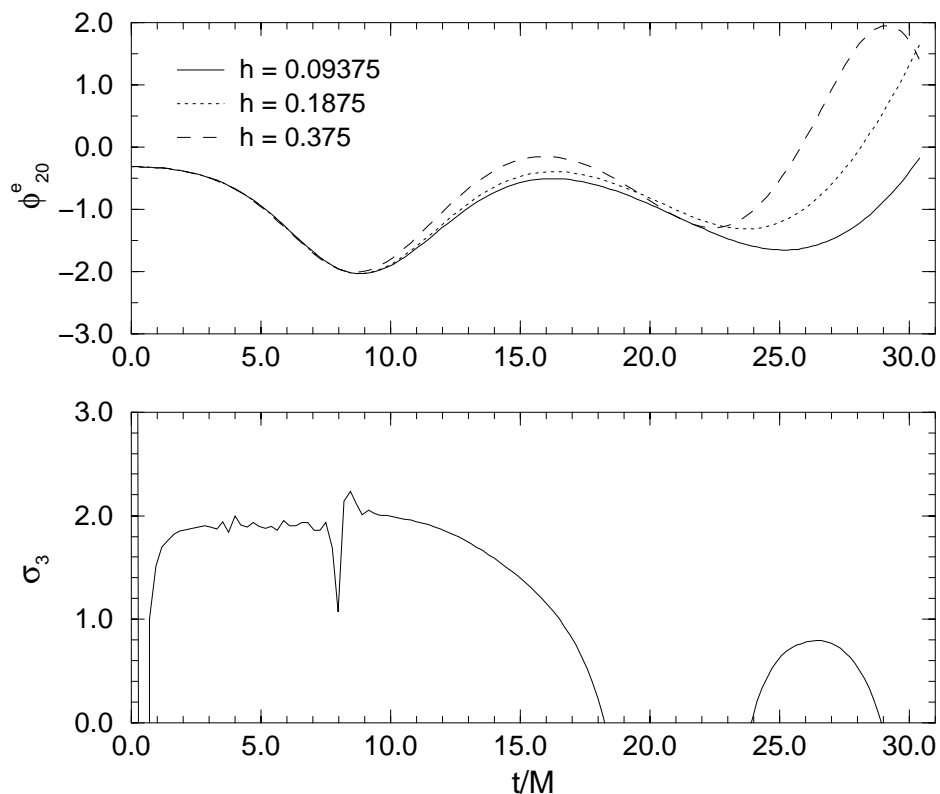
Figure 7.4: Convergence of the even parity wave mode ϕ_{20}^{e}. (a) Wave forms for different resolutions extracted at $r_{ext} = 4M$. (b) Convergence exponent σ_3.

For $t > 10M$ the convergence exponent decreases slowly, reaching $\sigma_3 = 1$ at $t = 16.5M$. At this time the exponent drops down rather fast until zero convergence is reached at $t = 18.3M$. After this time the convergence is undefined except between $24M$ and $29M$ where a small convergence rate below first order is achieved.

Considering higher resolutions, like a grid with $h = 0.125$ instead $h = 0.375$, the waves do not show such obvious deviations for the coarsest grid, even for $t > 18M$. However, also in this case the convergence rate diminishes and amounts below first order, but still remains defined, for $t > 18M$.

This examination shows that the wave extraction gives accurate results on the examined grids up to $t \approx 16.5M$. An extraction at larger radii on bigger grids might result in wave forms which are convergent for longer evolution time but further convergence tests would be necessary to verify this.

So far, the convergence tests done here show the possibility to extract the beginning of the wave modes but no long time development with the desired convergence behavior. Further work is necessary here to enlarge the interval of accurate wave extraction.

Chapter 8

Conclusion and Future Directions

In this thesis I presented results of a study of binary black hole systems in three dimensions constructed using the puncture type initial data introduced by Brandt and Brügmann. The calculations where done in the 3+1 (space+time) decomposition of spacetime, which was also reviewed here together with the conformal decomposition method for the construction of initial data and several types of initial data sets. With puncture initial data the lower asymptotically flat regions of the manifold representing the black hole system are compactified. This simplifies the solution of the constraint equations for the initial data.

The study of the initial data pointed out that, with two punctures, the initial data can represent either two separated black holes or a single black hole with two punctures in its interior. This was shown by the existence of apparent horizons.

The initial data solver shows very good second order convergence in the whole computational domain, except in the vicinity of the punctures where the convergence is expected to be of first order.

For vanishing momentum and spin the initial data is of the analytic, time symmetric, Brill-Lindquist type with vanishing extrinsic curvature and a regular part of the conformal factor which is unity. For finite momentum or spin the regular part of the conformal factor shows values above unity and the extrinsic curvature is non-zero. Due to the numerical solution in the construction of the initial data, the constraint equations are increasingly violated near the punctures for finite momentum or spin.

For further characterization of the generated initial data sets the ADM mass, the total linear momentum, and the total angular momentum were extracted dependent on the mass ratio, the separation, the momentum, and the spin of the black holes. This was done by integrating over coordinate spheres and subsequent extrapolation to infinity.

Examining the extracted values, more differences to Brill-Lindquist data showed up for initial data for finite spin or momentum. The ADM mass changes when the separation of the punctures is modified. This points to a non-linear correlation of the two black holes.

The total angular momentum is analytically related to the linear momenta of the black holes by the classical relation $\mathbf{J} = 2\mathbf{c} \times \mathbf{P}$. This was reproduced by the extraction procedure and served for the verification of extraction results.

The ADM mass of the black hole system depends non-linearly on the linear momenta of the black holes.

If spin is applied on the holes and counteracts with the angular momentum due to the linear momenta, the ADM mass can be reduced compared to a system without spin.

For high total angular momentum caused by high linear momenta on the black holes the extraction shows large errors. In these cases the extraction from initial data computed with Robin boundary conditions is much more accurate. However, the dynamical (multipole) region of the initial data slice grows with the linear momenta. With Robin boundary conditions the black hole system can be simulated with an error of 10 percent, according to the extraction of total angular momentum, when the linear momenta are of about the same size as the radius of the boundary and the masses of the black holes are of order unity.

Overall, it became clear that the extraction procedure yields the correct results, with an error of less than one percent, if the computational domain is sufficiently large. However, if the extraction should be applied in an evolution, the grid has to be very large. With a grid spacing of 0.25 as the maximum for a long time evolution of the data sets examined, and a boundary at a minimum radius of 48 for accurate extraction from the initial data, a grid with 384^3 grid points is necessary. In this evolutions such grids required about 110 GBytes of computer memory and fitted just into the largest available machine. But, since during the evolution grid points are falling into the black hole, the boundary is in fact still too close to the black hole to allow an accurate extraction during the evolution.

In connection with the examination of apparent horizons the interaction energy of the black holes was calculated. Here the interaction energy normalized by the ADM mass approached a constant negative value when either the mass ratio or the spin of the black holes was increased. In contrast to this, the interaction energy grew to positive values if a collinear momentum on the black holes was imposed. However, just from the initial data study it is not obvious if this means that the black holes will not merge in the coarse of their time evolution. This has to be tested in future simulations.

The evolution of binary black hole systems with the *BSSN*-formalism and 1+log-slicing showed the typical grid stretching effect due to the singularity avoiding properties of the slicing. The lapse collapses in the neighborhood of the punctures and the metric components grow next to the punctures.

According to the examination of apparent horizons during the evolution the separated black holes merge at a time of about 10M. Also visible is a small rotation of the system. Considering extracted gravitational waves a rotation of about 180 degrees until $t = 80M$ is visible near the boundary in visualizations.

The extraction of gravitational wave modes showed a very good second order convergence until about $t = 10M$. Until a time of $t = 16.5M$ the convergence order was larger than unity.

These studies show that, with the current implementations of initial data solvers and evolution routines, it is possible to evolve full 3D binary black hole systems sufficiently far into the future to extract gravitational wave modes. The longest evolution time achieved was about 40M at which the evolution errors have significantly grown but not yet terminated the evolution. Grids with smaller grid spacing and a boundary located further out can enable longer evolution times. However, this requires grids with a much larger number of grid points and hence more computer memory. Since the largest machines available for this work possess 128 GBytes of memory such simulations are currently not possible.

But waiting for larger machines does not solve this situation, since the required memory increases by about one order when the grid is refined by a factor of two. An adaptive mesh refinement (AMR), where resolution is added when needed or reduced when possible, can aid here.

However, also with finer grids, boundaries located further out, and even AMR the simulations will finally crash due to the grid stretching caused by the singularity avoiding slicing. Thus gauge freedom and singularities will prevent simulations from lasting for infinite time. Here the technique of black hole excision with the application of inner boundary conditions promises a solution. This, together with appropriate shift conditions, will reduce grid stretching effects by a very large amount and eliminates the singularities from the simulation.

Finally, when very long evolution time has been achieved, the importance of boundary conditions increases in order to obtain highly accurate long time evolutions. With current radiative boundary conditions there is still an error running inwards from the boundary as can be seen e.g. in the value of the Hamiltonian constraint. Thus, more advanced boundary conditions have to be considered or developed.

Bibliography

[1] A. Abrahams, D. Bernstein, D. Hobill, E. Seidel, and L. Smarr. Numerically generated black hole spacetimes: Interaction with gravitational waves. *Phys. Rev. D*, 45:3544–3558, 1992.

[2] Andrew Abrahams and C. Evans. Gauge invariant treatment of gravitational radiation near the source: Analysis and numerical simulations. *Phys. Rev. D*, 42:2585–2594, 1990.

[3] *http://www.aei-potsdam.mpg.de*.

[4] M. Alcubierre, G. Allen, B. Brügmann, E. Seidel, and W.-M. Suen. Towards an understanding of the stability properties of the 3+1 evolution equations in general relativity. 1999. gr-qc/9908079.

[5] M. Alcubierre, S. Brandt, B. Brügmann, C. Gundlach, J. Massó, and P. Walker. Testbeds and applications for apparent horizon finders in numerical relativity. 1998. gr-qc/9809004.

[6] G. Allen, K. Camarda, and E. Seidel. 3d black hole spectroscopy: Determining waveforms from 3d excited black holes. 1998. gr-qc/9806036, submitted to Phys. Rev. D.

[7] P. Anninos, D. Bernstein, S. Brandt, D. Hobill, E. Seidel, and L. Smarr. Dynamics of black hole apparent horizons. *Phys. Rev. D*, 50:3801–3815, 1994.

[8] P. Anninos, D. Bernstein, S. Brandt, J. Libson, J. Massó, E. Seidel, L. Smarr, W.-M. Suen, and P. Walker. Dynamics of apparent and event horizons. *Phys. Rev. Lett.*, 74:630–633, 1995.

[9] P. Anninos, K. Camarda, J. Massó, E. Seidel, W.-M. Suen, and J. Towns. Three-dimensional numerical relativity: The evolution of black holes. *Phys. Rev. D*, 52(4):2059–2082, 1995.

[10] P. Anninos, D. Hobill, E. Seidel, L. Smarr, and W.-M. Suen. Collision of two black holes. *Phys. Rev. Lett.*, 71(18):2851–2854, 1993.

[11] P. Anninos, D. Hobill, E. Seidel, L. Smarr, and W.-M. Suen. The head-on collision of two equal mass black holes. *Phys. Rev. D*, 52(4):2044–2058, 1995.

[12] Peter Anninos and Steven Brandt. Headon collision of two unequal mass black holes. *Phys. Rev. Lett.*, 81:508–511, 1998.

[13] R. Arnowitt, S. Deser, and C. W. Misner. The dynamics of general relativity. In L. Witten, editor, *Gravitation: An Introduction to Current Research*, pages 227–265. John Wiley, New York, 1962.

[14] T. W. Baumgarte and S. L. Shapiro. On the numerical integration of einstein's field equations. *Physical Review D*, 59:024007, 1999.

[15] D. Bernstein. *A Numerical Study of the Black Hole Plus Brill Wave Spacetime*. PhD thesis, University of Illinois Urbana-Champaign, 1993.

[16] L. Blanchet, T. Damour, B. Iyer, C. Will, and A. Wiseman. Gravitational-radiation damping of compact binary systems to second post-newtonian order. *Phys. Rev. Lett.*, 74:3515, 1995.

[17] C. Bona, J. Massó, E. Seidel, and J. Stela. New formalism for numerical relativity. *Phys. Rev. Lett.*, 75:600–603, 1995.

[18] C. Bona, J. Massó, E. Seidel, and J. Stela. First order hyperbolic formalism for numerical relativity. *Phys. Rev. D*, 56:3405–3415, 1997.

[19] J. Bowen and J. W. York. Time-asymmetric initial data for black holes and black-hole collisions. *Phys. Rev. D*, 21:2047–2056, 1980.

[20] S. Brandt and B. Brügmann. A simple construction of initial data for multiple black holes. *Phys. Rev. Lett.*, 78(19):3606–3609, 1997.

[21] S. Brandt and E. Seidel. Evolution of distorted rotating black holes i: Methods and tests. *Phys. Rev. D*, 52(2):856–869, 1995.

[22] S. Brandt and E. Seidel. Evolution of distorted rotating black holes ii: Dynamics and analysis. *Phys. Rev. D*, 52(2):870–886, 1995.

[23] D. Brill and R. Lindquist. Interaction energy in geometrostatics. *Phys. Rev.*, 131:471–476, 1963.

[24] B. Brügmann. Adaptive mesh and geodesically sliced schwarzschild spacetime in 3+1 dimensions. *Phys. Rev. D*, 54(12):7361–7372, 1996.

[25] B. Brügmann. Bifunctional adaptive mesh (bam) for 3d numerical relativity. In J. Frieman A. Olinto and D. Schramm, editors, *Proceedings of The 18th Texas Symposium on Relativistic Astrophysics*, Singapore, 1998. World Scientific.

[26] B. Brügmann. Binary black hole mergers in 3d numerical relativity. *Int. J. Mod. Phys. D*, 8:85, 1999.

[27] *http://www.cactuscode.org*.

[28] K. Camarda. *A Numerical Study of 3D Black Hole Spacetimes*. PhD thesis, University of Illinois at Urbana-Champaign, Urbana, Illinois, 1998.

[29] K. Camarda and E. Seidel. Numerical evolution of dynamic 3d black holes: Extracting waves. *Phys. Rev. D*, 57:R3204, 1998. gr-qc/9709075.

[30] G. Cook. *Initial Data for the Two-Body Problem of General Relativity*. PhD thesis, University of North Carolina at Chapel Hill, Chapel Hill, North Carolina, 1990.

[31] G. B. Cook. Initial data for axisymmetric black-hole collisions. *Phys. Rev. D*, 44:2983–3000, 1991.

[32] G. B. Cook, M. W. Choptuik, M. R. Dubal, S. Klasky, R. A. Matzner, and S. R. Olivera. Three-dimensional initial data for the collision of two black holes. *Phys. Rev. D*, 47:1471, 1993.

[33] Larry L. Smarr David W. Hobill. Supercomputing and numerical relativity: A look at the past, present and future. In C. Evans, L. Finn, and D. Hobill, editors, *Frontiers in Numerical Relativity*. Cambridge University Press, Cambridge, England, 1989.

[34] Éanna É. Flanagan and Scott A. Hughes. Measuring gravitational waves from binary black hole coalescence: I. signal to noise for inspiral, merger, and ringdown. *Phys. Rev. D*, 57:4535, 1998. gr-qc/9701039.

[35] Éanna É. Flanagan and Scott A. Hughes. Measuring gravitational waves from binary black hole coalescences: Ii. the waves' information and its extraction, with and without templates. *Phys. Rev. D*, 57:4566, 1998. gr-qc/9710129.

[36] R. J. Gleiser, C. O. Nicasio, R. H. Price, and J. Pullin. Colliding black holes: How far can the close approximation go? *Physical Review Letters*, 77(22):4483–4486, 1996.

[37] C. Gundlach. Pseudo-spectral apparent horizon finders: an efficient new algorithm. *Phys. Rev. D*, 57:863, 1998. gr-qc/9707050.

[38] S. G. Hahn and R. W. Lindquist. The two body problem in geometrodynamics. *Ann. Phys.*, 29:304–331, 1964.

[39] S. W. Hawking and G. F. R. Ellis. *The Large Scale Structure of Spacetime*. Cambridge University Press, Cambridge, England, 1973.

[40] J. D. Jackson. *Classical Electrodynamics*. Wiley, New York, 1975.

[41] *http://jean-luc.aei-potsdam.mpg.de*.

[42] R. P. Kerr. Gravitational field of a spinning mass as an example of algebraically special metrics. *Phys. Rev. Lett.*, 11:237–238, 1963.

[43] A. Lichnerowicz. L'intégration des équations de la gravitation relativiste et la problème des n corps. *J. Math Pures et Appl.*, 23:37, 1944.

[44] C. Misner. Wormhole initial conditions. *Phys. Rev.*, 118(4):1110–1111, 1960.

[45] C. W. Misner, K. S. Thorne, and J. A. Wheeler. *Gravitation*. W. H. Freeman, San Francisco, 1973.

[46] V. Moncrief. Gravitational perturbations of spherically symmetric systems. i. the exterior problem. *Annals of Physics*, 88:323–342, 1974.

[47] N. O'Murchadha and J. York. Gravitational energy. *Phys. Rev. D*, 10(8):2345–2357, 1974.

[48] J. Pullin. private communication, 1994.

[49] M. Shibata and T. Nakamura. Evolution of three-dimensional gravitational waves: harmonic slicing case. *Phys. Rev. D*, 52:5428, 1995.

[50] J. Thornburg. *Classical and Quantum Gravity*, 14:1119, 1987. Unruh is cited here by Thornburg as originating AHBC.

[51] K. Thorne. Ligo, virgo, and the international network of laser-interferometer gravitational-wave detectors. In M. Sasaki, editor, *Proceedings of the Eight Nishinomiya-Yukawa Symposium on Relativistic Cosmology*, Japan, 1994. Universal Academy Press.

[52] R. M. Wald. *General Relativity*. The University of Chicago Press, Chicago, 1984.

[53] P. Walker. *Horizons, Hyperbolic Systems, and Inner Boundary Conditions in Numerical Relativity*. PhD thesis, University of Illinois at Urbana-Champaign, Urbana, Illinois, 1998.

[54] J. York. Kinematics and dynamics of general relativity. In L. Smarr, editor, *Sources of Gravitational Radiation*. Cambridge University Press, Cambridge, England, 1979.

[55] J. York. Energy and momentum of the gravitational field. In F. J. Tipler, editor, *Essays in General Relativity*, pages 39–58. Academic Press, New York, 1980.

[56] J. York. Initial data for collisions of black holes and other gravitational miscellany. In C. Evans, L. Finn, and D. Hobill, editors, *Frontiers in Numerical Relativity*, pages 89–109. Cambridge University Press, Cambridge, England, 1989.